von KARMAN INSTITUTE

FOR FLUID DYNAMICS

COURSE NOTE 58

V.K.I. SHORT COURSE

on

INTERNAL AERODYNAMICS OF ROCKET ENGINES

by

C.E. PETERS

RHODE-SAINT-GENESE, BELGIUM

APRIL 1966

von KARMAN INSTITUTE FOR FLUID DYNAMICS

COURSE NOTE 58

V.K.I. SHORT COURSE

on

INTERNAL AERODYNAMICS OF ROCKET ENGINES

by

C.E. PETERS

APRIL 1966

PREFACE

This course note contains approximately half of the lectures to be given in a short course: "Internal aerodynamics of rocket engines", to be given at the von Karman Institute, April 18-29, 1966. The objective of the course is to present current information on the analysis of flow in rocket exhaust nozzles. Much of the information to be presented in the course is not available in any standard reference book, but has been assembled from the technical literature of the past few years.

The von Karman Institute has been fortunate in obtaining the able participation of the following lecturers:

Dr K.N.C. Bray
University of Southampton

Dr P. Carrière
ONERA

Dr E. Le Grivès
ONERA

Mr C.E. Peters
ARO, Inc (Arnold Engineering Development Center)
(VKI Visiting professor, 1965-66)

Mr H. Ramm
ARO, Inc.

The lectures of Drs Bray, Carrière and Le Grivès are not included in this course note; neither are the lectures on ground testing of rocket engines. It is hoped that the notes for these lectures can be assembled and published later as a supplement.

R.O. Dietz
Director

SHORT COURSE LECTURE TOPICS

1. Introduction (Mr Dietz)

2. Conventional convergent-divergent nozzles (Mr Peters)

3. Viscous effects in nozzles (Dr Carrière)

4. Altitude-compensating nozzles (Dr Le Grivès)

5. Two-phase flow in rocket nozzles (Mr Peters)

6. Thrust vector control (Mr Peters)

7. Nozzle flow with chemical reaction (Dr Bray)

8. Advanced rocket nozzle concepts (Mr Peters)

9. Ground testing of rockets (Mr Ramm and Mr Peters)

TABLE OF CONTENTS

NOMENCLATURE

The following nomenclature has been used in these notes. Exceptions and additional nomenclature are defined in the text.

A	cross sectional area
A^*	throat area
b	width of turbulent mixing region (chapter 5)
c	speed of sound
c^*	characteristic velocity (chapter 1)
$\bar{c}_e$	characteristic exhaust velocity (chapter 1)
c_p	specific heat at constant pressure
c_v	specific heat at constant volume
C_D	drag coefficient
C_p	pressure coefficient
d	diameter
D	diameter
F	axial thrust
g_o	standard gravitational acceleration
h	static enthalpy, convective heat transfer coefficient, height
H	stagnation enthalpy
I_{sp}	specific impulse
k	thermal conductivity, empirical constant

K	ratio of particle velocity to gas velocity (chapter 3)
L	length, particle temperature ratio (chapter 3)
Le	Lewis number
m	mass
M	Mach number
M*	ratio of velocity to speed of sound at sonic condition
$\mathcal{M}$	molecular weight
Nu	Nusselt number
$\frac{O}{F}$	oxidizer-fuel mass ratio
p	pressure
Pr	Prandtl number
r	radial coordinate, radius
R	universal gas constant, shock radius, radius of curvature
Re	Reynolds number
s	entropy
t	time
T	temperature
u	axial velocity component
v	transverse velocity component
V	total velocity vector
V_{max}	maximum velocity, $\sqrt{2c_pT_o}$
w	mass flow rate
x	axial coordinate
y	transverse coordinate

Greek

α	Mach angle, injection angle (chapter 4)
γ	ratio of specific heats, $\frac{c_p}{c_v}$
δ	separation angle (chapter 4)
ε	turbulent eddy viscosity
θ	streamline angle
μ	viscosity
ξ	evaporation factor (chapter 4)
ρ	density
ϕ	velocity potential
ψ	stream function

Subscripts

a	air stream (chapter 5)
ax	axial
aug	augmented (chapter 5)
c	chamber conditions
e	conditions at nozzle exit
g	gaseous phase
i	injectant (chapter 4), inner boundary of mixing region (chapter 5)
id	ideal
j	central stream (chapter 5)
m	conditions at beginning of particle solidification (chapter 3)

max	maximum
o	stagnation conditions, initial conditions
p	particle phase
s	separation, throat (chapter 2), side (chapter 4)
v	vacuum
w	wall
∞	free stream or ambient conditions

Superscripts

*	conditions at throat or at Mach number unity (except M* and c*)

Inleiding.

CHAPTER I

INTRODUCTION TO THE FLOW IN NOZZLES

1.1 INTRODUCTION

The modern rocket engine is a complex device, but here we need only consider two basic elements, the combustion chamber and the exhaust nozzle. A high temperature working fluid is generated in the combustion chamber where a propellant or combination of propellants, undergoes exothermic chemical reaction. In the liquid propellant rocket, the propellants are stored in tanks and are injected into the combustion chamber at a prescribed rate. In the solid propellant rocket, the combustion chamber also serves as the propellant storage vessel, with the rate of propellant consumption determined by the amount of exposed burning surface and by the combustion chamber pressure. It is normally assumed that the flow at the exit of the combustion chamber is uniform, at negligible velocity, and that the fluid is in thermodynamic and chemical equilibrium.

The second basic element of the rocket engine, the exhaust nozzle, is the primary subject of these lectures. The function of the exhaust nozzle is to convert the internal energy of the working fluid to kinetic energy, and thus to produce thrust.

The analysis of the rocket exhaust nozzle is presented from an engineering point of view, in that the current state of theoretical knowledge is emphasized. Because of the complex

nature of the flow processes within a rocket nozzle, much of the theoretical work is approximate in nature. For this reason, the theoretical results have been compared with experimental results whenever possible. Certainly, many aspects of rocket nozzle flow are incompletely understood. It is hoped that this series of lectures will point out the need for additional research in many of these trouble areas.

Structural aspects of exhaust nozzle design are not considered in this course. Also, the important subject of thermal protection of the nozzle walls is not covered. The fundamental aspects of rocket engine cooling are discussed in basic texts on rocketry (for example, refs. 1-1 and 1-2). Excellent reviews of advanced rocket cooling concepts are presented in refs. 1-3 and 1-4.

Organization of course.

The first lecture in the series is on the subject of idealized nozzle performance, based on the assumptions of (1) frictionless perfect gases of constant composition, and (2) one-dimensional flow. This idealized nozzle performance forms the basis on which the performance of actual exhaust nozzles is evaluated. The departure of actual nozzle performance from this ideal is the subject of subsequent lectures.

In the next lecture (Chapter 2) the subject of nozzle shape is discussed, again with the assumption of a frictionless gas of constant composition. This lecture is basically on departures from one-dimensional flow in the nozzle. Methods of analyzing the transonic nozzle flow are described. The shape of the divergent portion of the nozzle is discussed, starting with the commonly used conical nozzle. The techniques of Rao, as well as various simplified methods, are described for optimization of the divergent nozzle contour.

The next lecture, by Dr Carrière, is concerned with the effects of fluid viscosity on the performance of exhaust nozzles. First, the thrust loss caused by viscous drag on the nozzle walls is considered. Then the complex subject of over-expanded nozzle operation with boundary layer separation is discussed.

The conventional internal expansion nozzle is operating at optimum conditions at only one ambient pressure. Various altitude-compensating nozzles, in which the amount of

nozzle expansion is controlled by the ambient pressure, are the subject of the lecture by Dr Le Grivès.

The lectures by Dr Bray are on the complex subject of nozzle flow with chemical reactions, both for flows in chemical equilibrium and for flows with finite rate chemistry.

The final departure from ideal nozzle performance is discussed in the section on nozzle flows with solid particles (Chapter 3). Most solid and some liquid propellants produce a working fluid which is a mixture of gas and dispersed solid (or liquid) phases. Because the particles have finite mass, and because they must be accelerated by fluid friction, the particles always lag the gas to a certain degree. This lag, both in velocity and temperature, leads to losses in nozzle performance which are sometimes substantial.

The section on thrust vector control (Chapter 4) is primarily concerned with the analysis of the side force produced by asymmetrical injection of fluid into the divergent portion of the rocket exhaust nozzle. Prediction of the side force generated on the nozzle walls requires analysis of the effect of the injected flow on the main flow through the nozzle.

In Chapter 5, advanced rocket engine concepts are discussed from the standpoint of the effect on exhaust nozzle design. Particular emphasis is given to the air-augmented rocket, a device which offers some of the performance advantages of the air breathing engine during the atmospheric portion of the vehicle flight. First, the overall potential of the air-

augmented rocket is analyzed by simplified theory, then the detailed analysis of the complex flow in the mixing section is discussed.

The detailed analysis of rocket engine performance is a complex and, in some cases, a somewhat uncertain task. For this reason, as well as to evaluate mechanical integrity, an important step in any engine development program is to ground test the rocket engine. The final lectures are on the subject of the design of ground testing facilities to provide a simulated high altitude environment for the rocket engine. Special attention is given to the ejector-diffuser, a device in which the rocket itself provides the source of power for pumping the environment surrounding the rocket to a low pressure.

A large amount of material is covered in this course. Some of the areas cannot be covered in great depth, but the references provided should allow the course participants to dig more deeply into these areas.

1.2 IDEALIZED NOZZLE ANALYSIS

The idealized perfect rocket, in which the flow is assumed to be one-dimensional, will be analyzed in this section. Such an analysis leads to a basic understanding of the important variables in rocket nozzle design. Relatively simple formulae are obtained for the basic nozzle performance parameters, therefore, the idealized results are often used for preliminary engineering calculations. The idealized analysis also defines the upper limit for the performance of any real nozzle system using gases of fixed composition, and thus serves as a basis for evaluating the efficiency of real nozzles.

Similar analyses of the ideal rocket are presented in basic references on rocketry (for example, refs. 1-1, 1-2 and 1-5).

1.2.1 Assumptions and basic equations

Assumptions: The following assumptions are used in the idealized nozzle analysis:

1. One-dimensional flow
2. Steady flow
3. Frictionless gases
4. Adiabatic flow
5. Perfect gases
6. Constant specific heats
7. Negligible flow velocity in combustion chamber
8. Heat addition is completed within the combustion chamber.

Basic equations: Consider a control surface extending from a stagnation section to any section of the flow channel:

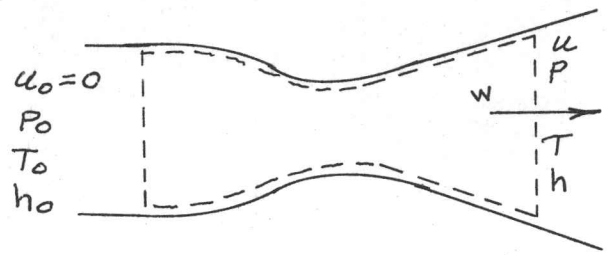

Assumptions 4 and 8 allow the energy equation to be written (First Law of Thermodynamics) :

$$h_o = h + \frac{u^2}{2} = \text{constant} \qquad (1\text{-}1)$$

The assumptions that the flow is frictionless and adiabatic imply that the flow is isentropic (Second Law of Thermodynamics):

$$s = s_o = \text{constant} \qquad (1\text{-}2)$$

Equation of continuity:

$$w = \rho u A = \text{constant} \qquad (1\text{-}3)$$

Equation of state (general form):

$$h = h(s,p)$$
$$\rho = \rho(s,p) \qquad (1\text{-}4)$$

The isentropic expansion process in the nozzle may be represented as

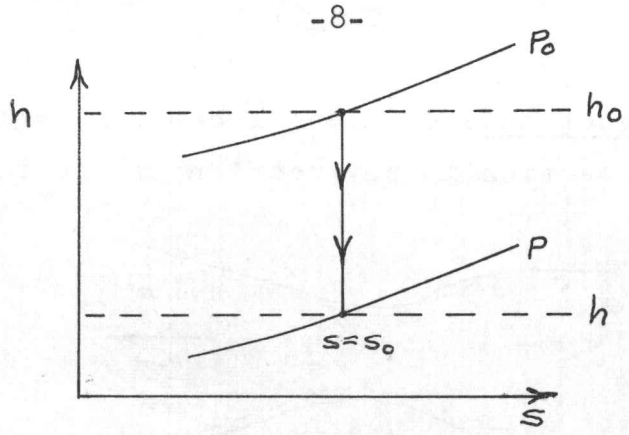

The definition of the Mach number and the speed of sound are:

$$M = \frac{u}{c} = \frac{u}{\sqrt{\left(\frac{\partial p}{\partial \rho}\right)_s}} \qquad (1\text{-}5)$$

Note that we have not yet made the restriction that the gases are perfect.

Subsonic and supersonic flow: The steady flow energy equation in differential form is:

$$dh = -udu \qquad (1\text{-}6)$$

For isentropic flow the relation $Tds = dh - \frac{dp}{\rho}$ becomes

$$dh = \frac{dp}{\rho} \qquad (1\text{-}7)$$

Combining (1-6) and (1-7) gives

$$dp = -\rho udu \qquad (1\text{-}8)$$

which is Euler's equation.

Now introduce the continuity equation in the logarithmic

differential form:

$$\frac{d\rho}{\rho} + \frac{dA}{A} + \frac{du}{u} = 0 \qquad (1\text{-}9)$$

Substituting (1-8) into (1-9) gives

$$\frac{d\rho}{\rho} + \frac{dA}{A} + \frac{dp}{\rho u^2} = 0$$

or

$$\frac{dA}{A} = \frac{dp}{\rho}\left[\frac{1}{u^2} - \frac{d\rho}{dp}\right]$$

The process is isentropic, therefore $\frac{dp}{d\rho} = \left(\frac{dp}{d\rho}\right)_s = c^2$, and

$$\frac{dA}{A} = \frac{dp}{\rho}\left[\frac{1}{u^2} - \frac{1}{c^2}\right] = \frac{dp}{\rho u^2}\left[1 - M^2\right] \qquad (1\text{-}10)$$

From eq. (1-8) we see that the pressure always decreases in an accelerating flow, i.e. $\frac{du}{dp} < 0$. From eq. (1-10) we can deduce the following:

(1) subsonic flow: $\frac{dA}{dp} > 0$ (and $\frac{dA}{du} < 0$)

(2) supersonic flow: $\frac{dA}{dp} < 0$ (and $\frac{dA}{du} > 0$)

(3) sonic flow: $\frac{dA}{dp} = 0$ (and $\frac{dA}{du} = 0$)

The relations show the well known fact that the effect of area change is opposite for subsonic and supersonic flow. We also see that the cross sectional area of continuously accelerated flow passes through a minimum at the sonic condition. The mass flux, ρu, therefore goes through a maximum at the sonic condition.

The continuity equation is

$$\frac{d(\rho u)}{\rho u} + \frac{dA}{A} = 0$$

thus $d(\rho u) = 0$ at the sonic condition, and ρu is a maximum.

Isentropic flow of a perfect gas: We now introduce the assumption that the gas is perfect with constant specific heats.

$$\frac{p}{\rho} = \frac{R}{\mathcal{M}} T \tag{1-11}$$

$$\Delta h = c_p \Delta T \tag{1-12}$$

$$(c_p - c_v) = \frac{R}{\mathcal{M}} \tag{1-13}$$

$$\frac{c_p}{c_v} = \gamma \tag{1-14}$$

$$c_p = \frac{\gamma}{\gamma - 1} \frac{R}{\mathcal{M}} \tag{1-15}$$

Equations (1-11) - (1-15) are valid in general for a perfect gas, and their use is not restricted to the case of isentropic flow.

We may now introduce the concept of the stagnation temperature. The energy equation (eq. 1-1) becomes:

$$T_o = T + \frac{u^2}{2c_p}$$

or

$$\frac{T_o}{T} = 1 + \frac{u^2}{2c_p T} = 1 + \frac{(\gamma-1)u^2}{2\gamma \frac{R}{\mathcal{M}} T} = 1 + \frac{\gamma-1}{2} M^2 \qquad (1\text{-}16)$$

Now introduce the isentropic condition, in the form of eq.(1-7)

$$dh = \frac{dp}{\rho}$$

and using eqs. (1-12) - (1-15) :

$$c_p dT = \frac{RT}{\mathcal{M}p} dp$$

$$\frac{\gamma}{\gamma-1} \frac{R}{\mathcal{M}} \frac{dT}{T} = \frac{R}{\mathcal{M}} \frac{dp}{p}$$

$$\frac{\gamma}{\gamma-1} \frac{dT}{T} = \frac{dp}{p}$$

Integrating between the limits of T_o and T gives

$$\frac{p_o}{p} = \left(\frac{T_o}{T}\right)^{\frac{\gamma}{\gamma-1}} \qquad (1\text{-}17)$$

where p_o is the isentropic stagnation pressure.

Also

$$\frac{\rho_o}{\rho} = \left(\frac{T_o}{T}\right)^{\frac{1}{\gamma-1}}$$

In terms of the Mach number, the ratios $\frac{T_o}{T}$, $\frac{p_o}{p}$ and $\frac{\rho_o}{\rho}$ are :

$$\frac{T_o}{T} = \left[1 + \frac{\gamma-1}{2} M^2\right] \tag{1-16}$$

$$\frac{p_o}{p} = \left[1 + \frac{\gamma-1}{2} M^2\right]^{\frac{\gamma}{\gamma-1}} \tag{1-18}$$

$$\frac{\rho_o}{\rho} = \left[1 + \frac{\gamma-1}{2} M^2\right]^{\frac{1}{\gamma-1}} \tag{1-19}$$

Rocket engines normally operate with sufficiently high chamber pressure so that the nozzle is always choked at the throat. The critical conditions at the throat (section of minimum area) are obtained by setting M = 1 in eqs. (1-16), (1-18) and (1-19):

$$\frac{T_o}{T^*} = 1 + \frac{\gamma-1}{2} = \frac{\gamma+1}{2} \tag{1-20}$$

$$\frac{p_o}{p^*} = \left[1 + \frac{\gamma-1}{2}\right]^{\frac{\gamma}{\gamma-1}} = \left[\frac{\gamma+1}{2}\right]^{\frac{\gamma}{\gamma-1}} \tag{1-21}$$

$$\frac{\rho_o}{\rho^*} = \left[1 + \frac{\gamma-1}{2}\right]^{\frac{1}{\gamma-1}} = \left[\frac{\gamma+1}{2}\right]^{\frac{1}{\gamma-1}} \tag{1-22}$$

<u>Mass flow in a choked nozzle</u>: The continuity equation at the throat is :

$$w^* = A^* \rho^* u^*$$

$$w = \frac{A^*p^*u^*}{\frac{R}{\mathcal{M}}T^*} = \frac{A^*p^*\gamma u^*}{\sqrt{\frac{\gamma R}{\mathcal{M}}}T^*c^*} = \frac{A^*p^*\sqrt{\frac{\gamma\mathcal{M}}{R}}}{\sqrt{T_o}\sqrt{\frac{T^*}{T_o}}} = \frac{A^*p_o\frac{p^*}{p_o}\sqrt{\frac{\gamma\mathcal{M}}{R}}}{\sqrt{T_o}\sqrt{\frac{T^*}{T_o}}}$$

Substituting the equations for $\frac{p^*}{p_o}$ and $\frac{T^*}{T_o}$:

$$w^* = \frac{A^*p_o}{\sqrt{T_o}}\sqrt{\frac{\gamma\mathcal{M}}{R}}\left[\frac{2}{\gamma+1}\right]^{\frac{\gamma+1}{2(\gamma-1)}}$$

or

$$w^* = \frac{A^*p_o}{\sqrt{T_o}}\sqrt{\frac{\gamma\mathcal{M}}{R}\left(\frac{2}{\gamma+1}\right)^{\frac{\gamma+1}{\gamma-1}}} \qquad (1\text{-}23)$$

Similarly, the mass flow at any other section of the nozzle is given by

$$w = \frac{Ap_o}{\sqrt{T_o}}M\sqrt{\frac{\gamma\mathcal{M}}{R}}\left[1 + \frac{\gamma-1}{2}M^2\right]^{-\frac{(\gamma+1)}{2(\gamma-1)}} \qquad (1\text{-}24)$$

Because the flow is steady, $w = w^*$. Equating eqs. (1-23) and (1-24) and solving for the area ratio $\frac{A}{A^*}$:

$$\frac{A}{A^*} = \frac{1}{M}\left[\frac{2}{(\gamma+1)}\left(1 + \frac{\gamma-1}{2}M^2\right)\right]^{\frac{(\gamma+1)}{2(\gamma-1)}} \qquad (1\text{-}25)$$

The variation of nozzle area ratio with pressure ratio is shown in fig. 1-1, for $\gamma = 1.2$, 1.3 and 1.4.

1.2.2 Nozzle thrust

Consider the rocket engine shown schematically:

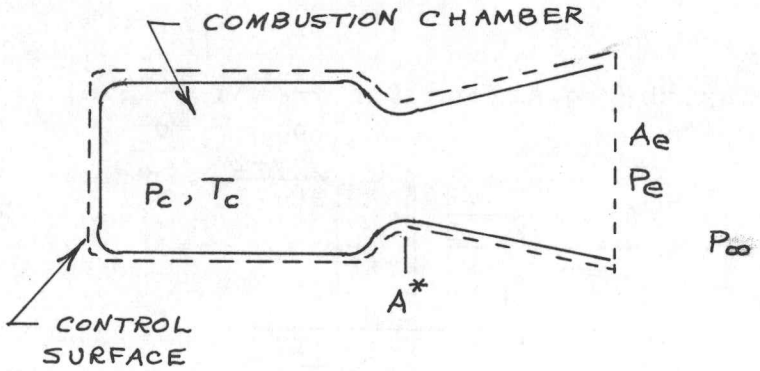

The net axial thrust on the rocket is obtained by applying the momentum theorem to the control surface. The entire control surface, except for A_e, is subjected to the ambient pressure, p_∞, and the thrust is

$$F = \int_{A_e} (p-p_\infty)dA + \int_{A_e} \rho u^2 dA \qquad (1\text{-}26)$$

Eq. (1-26) is valid for any rocket motor, if u is taken as the axial component of the velocity in the nozzle exit plane. For a liquid propellant engine in which the propellants are not stored in the chamber, the control surface is assumed to include the propellant tankage, so that the momentum of the injected propellants does not appear in the thrust equation.

For one dimensional flow in the nozzle, eq. (1-26) becomes:

$$F = (p_e-p_\infty)A_e + \rho_e u_e^2 A_e \qquad (1\text{-}27)$$

or

$$F = (p_e - p_\infty)A_e + wu_e \qquad (1\text{-}27a)$$

Equation (1-27) may also be written in terms of the exit plane Mach number as

$$\begin{aligned} F &= (p_e - p_\infty)A_e + \gamma p_e A_e M_e^2 \\ &= A_e \left[(p_e - p_\infty) + \gamma p_e M_e^2\right] \\ &= A_e p_e \left[1 + \gamma M_e^2 - \frac{p_\infty}{p_e}\right] \end{aligned} \qquad (1\text{-}27b)$$

The thrust in a vacuum ($p_\infty = 0$) is

$$F_v = p_e A_e \left[1 + \gamma M_e^2\right] \qquad (1\text{-}28)$$

F_v is sometimes referred to as the "thrust function" or "impulse function" (Shapiro, ref. 1-6). The useful ratio of F_v to the value of F_v at the nozzle throat is tabulated as $\frac{F}{F^*}$ in various tables of flow functions (for example, Keenan and Kaye, ref. 1-7).

Maximum thrust - Assuming that the nozzle stagnation conditions, A^* and p_∞ are fixed, the problem is to determine the exit area, A_e, which provides maximum thrust. The nozzle mass flow is, therefore, also fixed. Differentiating eq.(1-27a):

$$dF = (p_e - p_\infty)dA_e + A_e dp_e + wdu_e$$

Momentum considerationsgive $wdu = -Adp$, therefore

$$dF = (p_e - p_\infty)dA_e$$

The maximum thrust is obtained when $\frac{dF}{dA_e} = 0$, or when $p_e = p_\infty$. A nozzle which is operating with $p_e = p_\infty$ is said to be "adapted" or "correctly expanded". When $p_e > p_\infty$, the nozzle is said to be "underexpanded", and "overexpanded" when $p_e < p_\infty$.

The well known result that maximum thrust is obtained when $p_e = p_\infty$ can also be shown from simple physical reasoning. Consider a section of the nozzle wall near the exit plane:

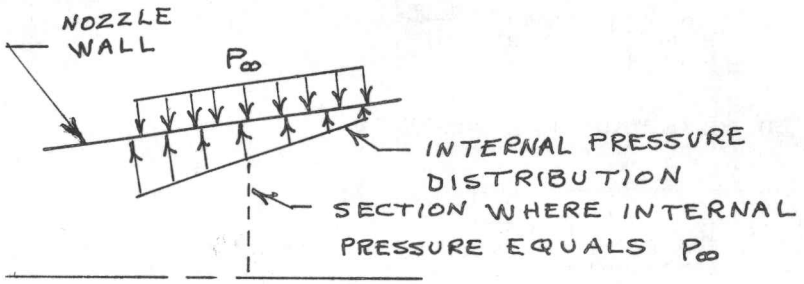

The thrust produced by the nozzle is determined by the excess of the pressure forces acting on the internal surface over the pressure forces acting on the external surface. Additional expansion of the flow produces additional thrust as long as the internal pressure is greater than p_∞ . When the internal pressure is less than p_∞, additional nozzle expansion causes negative thrust, or drag, on the nozzle. Clearly, the maximum thrust is obtained for a nozzle exit area, A_e, which gives $p_e = p_\infty$.

1.2.3 Rocket performance parameters

Several performance parameters are used in the evaluation of a rocket engine. Included are the nozzle thrust coeffi-

cient (C_F), characteristic velocity (c*), specific impulse (I_{sp}) and characteristic exhaust velocity ($\bar{c}_e$). These performance parameters are calculated from the parameters p_c, A*, F and w, all of which are relatively easy to measure during the experimental operation of a rocket engine. For the case of the ideal rocket, we shall see that these parameters are given by relatively simple relationships which show the significance of each of the performance parameters.

Nozzle thrust coefficient - The most commonly used parameter for evaluation of the efficiency of an exhaust nozzle is the thrust coefficient , C_F. By definition

$$C_F \equiv \frac{F}{p_c A^*} \tag{1-30}$$

Similarly, the vacuum thrust coefficient is

$$C_{Fv} = \frac{F_v}{p_c A^*} \tag{1-31}$$

C_{Fv} is related to C_F by

$$C_F = C_{Fv} - \frac{A_e}{A^*} \frac{p_\infty}{p_c} \tag{1-32}$$

Combining eq. (1-30) with eq.(1-27b) yields, for one dimensional nozzle flow:

$$C_F = \frac{A_e}{A^*} \frac{p_e}{p_c} \left[1 + \gamma M_e^2 - \frac{p_\infty}{p_e} \right] \tag{1-33}$$

Also

$$C_{Fv} = \frac{A_e}{A^*} \frac{p_e}{p_c} \left[1 + \gamma M_e^2 \right] \qquad (1\text{-}34)$$

The maximum value of C_F is obtained when $p_e = p_\infty$:

$$C_{F_{max}} = \frac{A_e}{A^*} \frac{p_e}{p_c} \gamma M_e^2 \qquad (1\text{-}35)$$

For isentropic nozzle flow, $p_o = p_c$; $\frac{A_e}{A^*}$ and M_e are functions of γ and $\frac{p_e}{p_c}$, and the following equation is obtained for C_F:

$$C_F = \left\{ \frac{2\gamma^2}{(\gamma-1)} \left(\frac{2}{\gamma+1}\right)^{\frac{\gamma+1}{\gamma-1}} \left[1 - \left(\frac{p_e}{p_c}\right)^{\frac{\gamma-1}{\gamma}} \right] \right\}^{\frac{1}{2}} + \left(\frac{p_e}{p_c} - \frac{p_\infty}{p_c}\right) \frac{A_e}{A^*} \qquad (1\text{-}36)$$

Equation (1-36) indicates that C_F is independent of T_c and $\mathcal{M}$, and is therefore insensitive to the efficiency of combustion. The combustion efficiency does have a small effect on γ, but for a given area ratio C_F is relatively insensitive to small variations of γ, especially for low area ratio nozzles. The nozzle thrust coefficient is normally interpreted to be a figure of merit for only the divergent portion of the exhaust nozzle. In practice, the test engineer compares the experimental value of C_F with the theoretical value, and the deviation from ideal is attributed to the exhaust nozzle, not to the combustion chamber.

The variation of C_F with $\frac{A_e}{A^*}$ is shown in fig. 1-2 for $\gamma = 1.2$. We see from fig. 1-2 that, for a given $\frac{A_e}{A^*}$, the value of C_F increases monotonically as $\frac{p_c}{p_\infty}$ is increased. This

increase in C_F is caused entirely by the decrease of the pressure acting on the outer surface of the nozzle.

The line of maximum thrust coefficients shown in fig. 1-2 corresponds to the locus of the optimum area ratios for the various values of $\frac{p_c}{p_\infty}$. We see that the curve of thrust coefficient for a given value of $\frac{p_c}{p_\infty}$ is fairly flat near the optimum area ratio. Therefore, the thrust coefficient is insensitive to small variations of the area ratio from the ideal value.

The "separation limit" shown in fig. 1-2 is determined by the inability of the nozzle boundary layer to remain attached to the nozzle wall for $\frac{p_\infty}{p_e} > 2.5$ (see section 1.2.3). For operating conditions to the right of the separation limit, C_F is no longer given by eqs (1-32) or (1-33).

Characteristic velocity - The performance parameter which is commonly used to evaluate the combustion chamber performance is the characteristic velocity c*. By definition:

$$c^* = \frac{p_c A^*}{w} \qquad (1\text{-}37)$$

Introducing eq.(1-23) for w, we get

$$c^* = \sqrt{\frac{1}{\gamma}\left(\frac{\gamma+1}{2}\right)^{\frac{\gamma+1}{\gamma-1}} \frac{RT_c}{\mathcal{M}}} \qquad (1\text{-}38)$$

The parameter c* is not a function of the supersonic nozzle

geometry, but only of $\gamma, \mathcal{M}$ and T_c. The characteristic velocity is primarily a measure of the efficiency of the combustion chamber. For a real rocket engine, c* is also influenced by the efficiency of the subsonic portion of the exhaust nozzle, because departures from one dimensional flow also influence the mass flow through the nozzle throat. Comparison of eqs.(1-30) and (1-37) indicates that

$$\frac{F}{\dot{m}} = C_F c^* \tag{1-39}$$

Specific impulse - A parameter used to evaluate the overall performance of a rocket is the specific impulse, I_{sp}. The specific impulse is defined as the ratio of the thrust to the mass flow. Rather than the mass flow, the specific impulse is normally defined in terms of the propellant weight flow in a standard gravitational field, thus

$$I_{sp} = \frac{F}{\dot{m} g_o} = \frac{\bar{c}_e}{g} \tag{1-40}$$

where g_o is the standard acceleration of gravity.

Effective exhaust velocity - Another parameter used to evaluate the overall performance of a rocket is the effective exhaust velocity, $\bar{c}_e$, defined as

$$\bar{c}_e = \frac{F}{\dot{m}} \tag{1-41}$$

Using eq. (1-27a), we see that

$$\bar{c}_e = u_e + \frac{(p_e - p_\infty) A_e}{\dot{m}} \tag{1-42}$$

The effective exhaust velocity is equal to the actual exhaust velocity when the nozzle is correctly expanded. Comparing eqs. (1-40) and (1-41), we see that I_{sp} and $\bar{c}_e$ differ only by the constant g_o, and

$$\bar{c}_e = g_o I_{sp} \qquad (1\text{-}43)$$

The objective of the rocket designer is to obtain the maximum vehicle acceleration for a given amount of propellant and he therefore is concerned with maximizing $\bar{c}_e$ (or I_{sp}). The other performance parameters, c* and C_F, are primarily diagnostic parameters used to point out the reasons for deficiencies in rocket performance.

Two areas of performance improvement are open to the rocket designer. The first is to increase c* by improving combustion efficiency, or by selecting propellants with a higher ratio of $\frac{T_c}{\mathcal{M}}$. The second area is to increase C_F by careful nozzle design.

Performance of typical propellants - Although the evaluation of propellants does not fall within the scope of this course, results for a few chemical propellants will be given to acquaint the reader with the range of values for the rocket performance. The following table includes a few propellant combinations in use or being considered for use. A more complete table is given in ref. 1-2. The data in the table were calculated by assuming adiabatic combustion, and ideal frozen expansion from p_c = 34 atm. to p_∞ = 1 atm. in a correctly expanded nozzle.

OXIDIZER	FUEL	O/F (mass ratio)	THEORETICAL T_c (°K)	γ	$\mathcal{M}$	I_{sp}
Fluorine	Hydrogen	4.50 (max. I_{sp})	3033	1.33	8.9	374
RFNA (22% NO_2)	UDMH	2.60	3144	1.23	22	250
Nitrogen Tetroxide	Hydrazine	1.10	3005	1.26	19	263
Oxygen	RP-1	2.00	3350	1.25	21	266
Oxygen	Hydrogen	3.50 (max. I_{sp})	2755	1.26	9.0	364

It should be noted that, for many applications such as the very long range single stage rocket, the important performance parameter is I_{sp}. For other applications where the mass of propellant consumed is small compared to the total vehicle mass, the important parameter is (I_{sp} x propellant bulk density). For such a mission propellant combinations containing hydrogen are considerably less desirable than is indicated by the I_{sp} of these propellant combinations. See ref. 1-2 for a more complete discussion of this subject.

1.2.3 Non adapted nozzle operation

We have seen in the previous section that the maximum thrust is obtained when $p_e = p_\infty$. In many practical rocket applications, however, the nozzle must operate through a range of ambient pressures. The first stage of a launch vehicle, for example, must operate satisfactorily from sea level to an altitude where the ambient pressure is perhaps only one-hundredth of sea level pressure.

Inviscid nozzle flow - The classical concept of inviscid supersonic nozzle flow is illustrated in fig. 1-3. The nozzle exit pressure, p_e, is independent of p_∞ until p_∞ is increased to the level where a normal shock is forced to move inside the nozzle. Condition (1) of fig. 1-3 corresponds to underexpanded nozzle operation, and the flow adjusts to p_∞ by passing through a series of expansion waves with a corresponding deflection of the free streamline. Condition (2) corresponds to "correct expansion" or "adapted" operation, with $p_e = p_\infty$. For condition (3), p_∞ is greater than p_e, but not sufficiently high to cause a normal shock at the nozzle exit plane. In this case of overexpanded nozzle operation the flow adjusts from p_e to p_∞ by passing through an oblique shock wave. Further increase of p_∞ causes a normal shock to be formed at the nozzle exit plane, with subsonic flow downstream of the shock (condition (4)). Higher ambient pressure causes a normal shock to be formed inside the nozzle (condition (5)). The ambient pressure could be increased to the level where the normal shock would be moved upstream to the nozzle throat; further increase of p_∞ would cause the flow in the nozzle to become entirely subsonic. Such

pressure ratios normally do not occur during steady-state rocket operation. This condition does occur, however, during the engine starting and shutdown transients.

We see that for overexpanded nozzle operation the pressures on the divergent portion of the nozzle are less than ambient, with a corresponding loss in thrust as compared to adapted nozzle operation. For conditions (1)-(4), p_e is equal to the design value, and the thrust coefficient may be calculated from eq. (1-32).

Viscous nozzle flow - The flow in a real nozzle is viscous, and a boundary layer exists along the nozzle wall. The boundary layer is limited in the amount of pressure rise that it will withstand without separation from the wall. For this reason, overexpanded nozzle operation is quite different in character from that presented in the preceding section, where the effects of boundary layer were ignored.

For underexpanded flow ($p_e > p_\infty$), the flow is the same as shown in fig. 1-3, with the flow adjusting to the ambient pressure through a series of expansion waves. Increasing the ambient pressure to slightly above p_e causes the flow to adjust to p_∞ through an oblique shock, shown as condition (3) in fig. 1-3. The upper limit on p_∞/p_e to form an oblique shock at the exit plane, however, is not given by the normal shock condition, but rather is controlled by the separation characteristics of the nozzle boundary layer. The type of flow shown in fig. 1-3 as conditions (4) and (5) never exists in reality. Approximately, when $\frac{p_\infty}{p_e} > 2.5\text{-}3.0$, the point of boundary layer

separation will move upstream into the divergent portion of the nozzle, as shown in fig. 1-4. It is assumed that the nozzle boundary layer is turbulent, which is usually the case in rocket nozzles.

The subject of boundary layer separation is very complex and will be covered in a later lecture by Dr Carrière. For purposes of discussion, we may adopt here the simplified "Summerfield criterion" for the separation characteristics (ref. 1-2). By inspection of experimental separation data for nozzles with wall angles of approximately 15 degrees, Summerfield concluded that boundary layer separation will occur if $\frac{p_\infty}{p_e} > 2.5$. When the separation occurs inside the nozzle, it will be assumed that the wall pressure is constant downstream of separation, and that the separation occurs where $\frac{p_\infty}{p_s} = 2.5$ (see fig. 1-4 for nomenclature). This view of the separation phenomenon is highly simplified. In reality, the pressure ratio at separation may vary from 2.5 to 3.5 or higher, depending on the specific flow conditions. Also, as indicated in fig. 1-4, the region downstream of separation is not at constant pressure, but a certain amount of recompression occurs, depending on the nozzle geometry. The simplified model, however, does serve to illustrate the major influence of boundary layer separation on nozzle performance.

Nozzle thrust - Because of boundary layer separation, the pressures inside the nozzle are never lower than about $0.4\ p_\infty$. Boundary layer separation, therefore, is desirable from the standpoint of thrust when the nozzle is operated in the overexpanded condition. This effect is illustrated in fig. 1-5,

where the effect of variable ambient pressure is shown for two nozzle area ratios, $\frac{A_e}{A^*} = 5$ and $\frac{A_e}{A^*} = 20$. The range of pressure ratios shown is insufficient to cause a normal shock in the flow for the case of inviscid flow. Fig. 1-5(a) shows that C_F varies linearly with $\frac{p_\infty}{p_e}$ for $\frac{p_\infty}{p_e} < 2.5$. Without boundary layer separation C_F would continue to decrease linearly for increasing p_∞, as indicated by the dashed lines for $\frac{p_\infty}{p_e} > 2.5$. The occurrence of boundary layer separation, however, causes C_F to decrease much less rapidly for $\frac{p_\infty}{p_e} > 2.5$.

In fig. 1-5(b), the variation of $C_F/C_{F_{id}}$ with p_∞/p_e is shown for the same nozzle area ratios. The ideal thrust coefficient was calculated by assuming that the nozzle area ratio was varied so that the nozzle was correctly expanded for all cases. First, we see that the performance penalty caused by using a non-adapted nozzle is small, as long as $0.5 < \frac{p_\infty}{p_e} < 2$. Also, we see that the high area ratio nozzle is somewhat less sensitive to non-adapted operation than is the low area ratio nozzle. For overexpanded operation with boundary layer separation, $C_F/C_{F_{id}}$ remains nearly constant with increasing p_∞/p_e. This conclusion is based on a highly simplified separation model.

Figure 1-5 has illustrated that boundary layer separation prevents very large overexpansion thrust losses. This fact leads one to consider using a large area ratio nozzle for a launch rocket which starts at sea level and operates through a large range of ambient pressures. The performance of two nozzles operating from sea level to an altitude greater than

25 km is shown in fig. 1-6. For p_c = 40 atm. the area ratio 10 nozzle has design p_e = 0,5 atm., and separation does not occur in this nozzle at sea level. The area ratio 40 nozzle has design p_e = .083 atm., and boundary layer separation occurs at altitudes less than 11.4 km. We see in fig. 1-6(a) that the thrust coefficient of the area ratio 40 nozzle is 1-2% below that of the area ratio 10 nozzle for altitudes less than 10 km, but is substantially higher (3 - 7 %) at altitudes greater than 15 km. The difference in performance is shown more graphically in fig. 1-6(b), where the ratio $C_F/C_{F_{id}}$ is presented.

The area ratio 40 nozzle appears to be somewhat superior in this comparison, depending on the maximum altitude for the launch vehicle. In practice, however, the area ratio 10 nozzle would be chosen for this application. This choice would be governed by two considerations. First, the actual thrust of a nozzle with boundary layer separation is less than indicated by figs. 1-5 and 1-6, because of the recompression downstream of separation. This loss is greater with contoured nozzles having small wall angles near the exit than for a conical nozzle. The second reason for avoiding boundary layer separation is that the separation may be unstable in position, which could cause severe mechanical problems.

REFERENCES

1-1 SUTTON: Rocket propulsion elements.
John Wiley & Sons, New York, 3rd edition, 1963

1-2 BARRERE, et al.: Rocket propulsion.
Elsevier Publishing Co, Amsterdam, London, New York, and Princeton, 1960.

1-3 ARMOUR, et al.: A review of nozzle concepts for future solid propellant rocket motors.
Philco Research Lab. RPL-TDR-64-8, March 1964.

1-4 SUTTON, et al.: Advanced cooling techniques for rocket engines.
Astronautics & Aeronautics, vol. 4, no 1, January 1966, pp. 60-71.

1-5 LANCASTER (editor): Jet propulsion engines.
vol. XII, High speed aerodynamics and jet propulsion, Princeton University press, Princeton, N.J., 1959.

1-6 SHAPIRO: The dynamics and thermodynamics of compressible fluid flow, vol. 1.
Ronald press, New York, 1953.

1-7 KEENAN & KAYE: Gas tables.
John Wiley & Sons, New York, 1961.

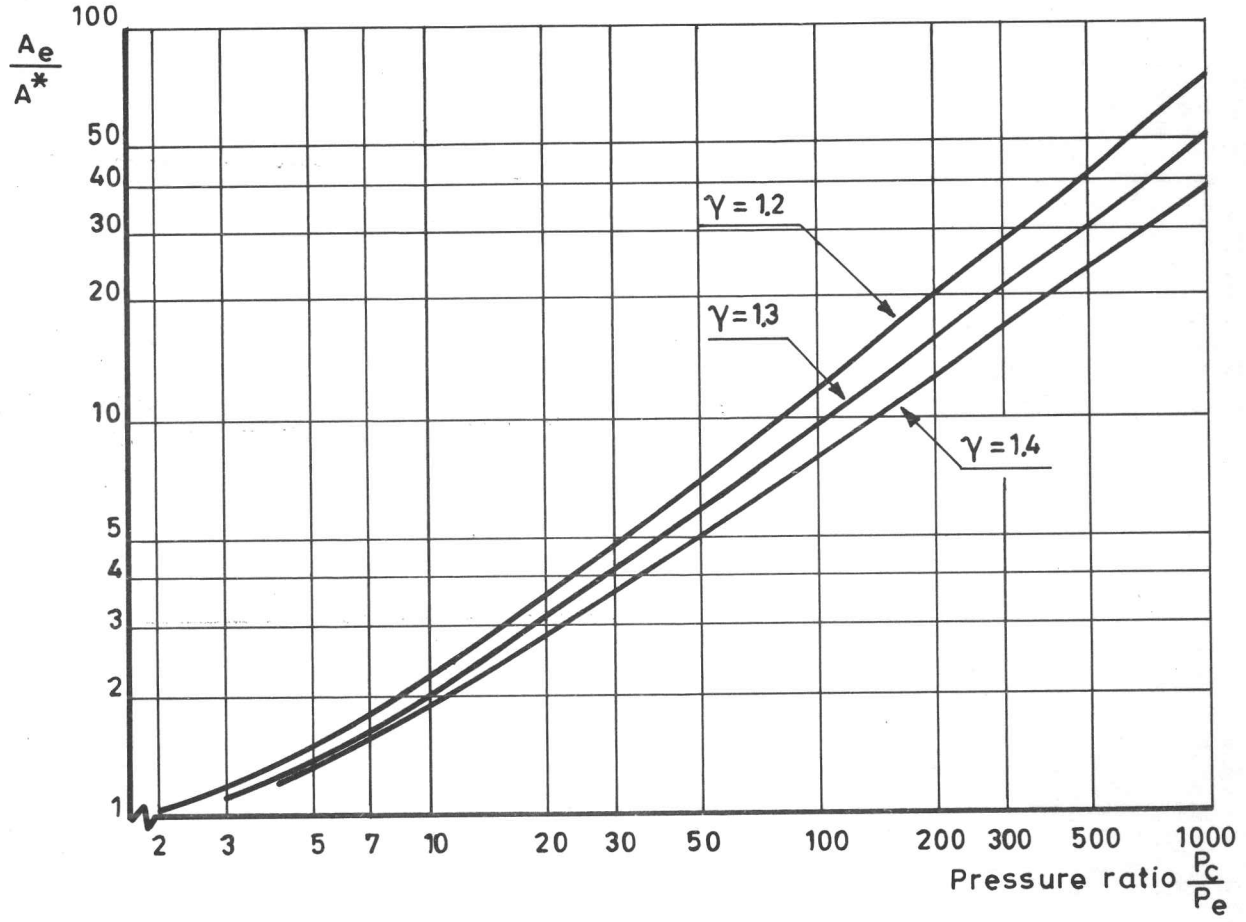

• Fig.1-1 VARIATION OF NOZZLE AREA RATIO WITH PRESSURE RATIO

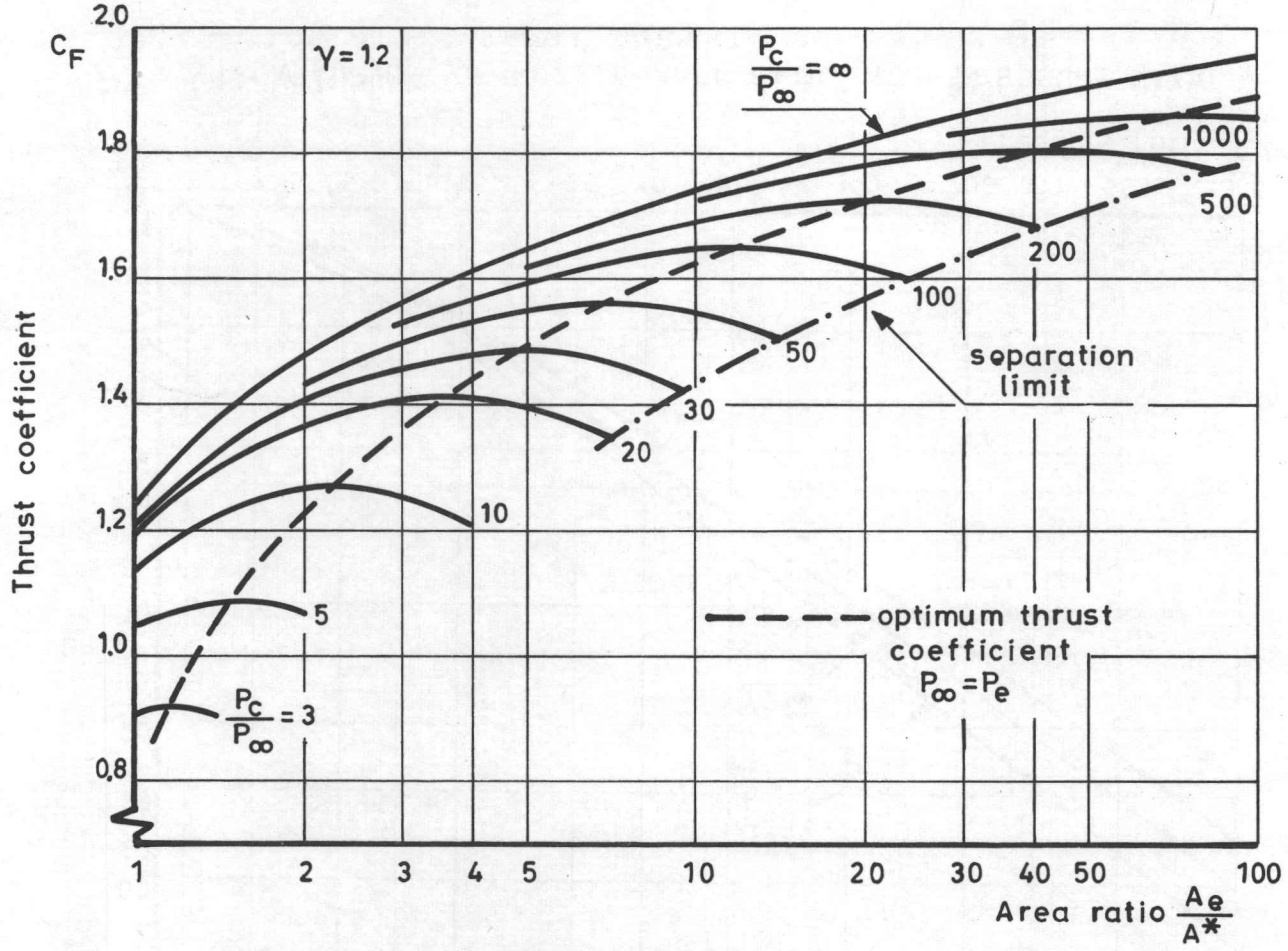

Fig. 1-2 VARIATION OF THRUST COEFFICIENT WITH AREA RATIO

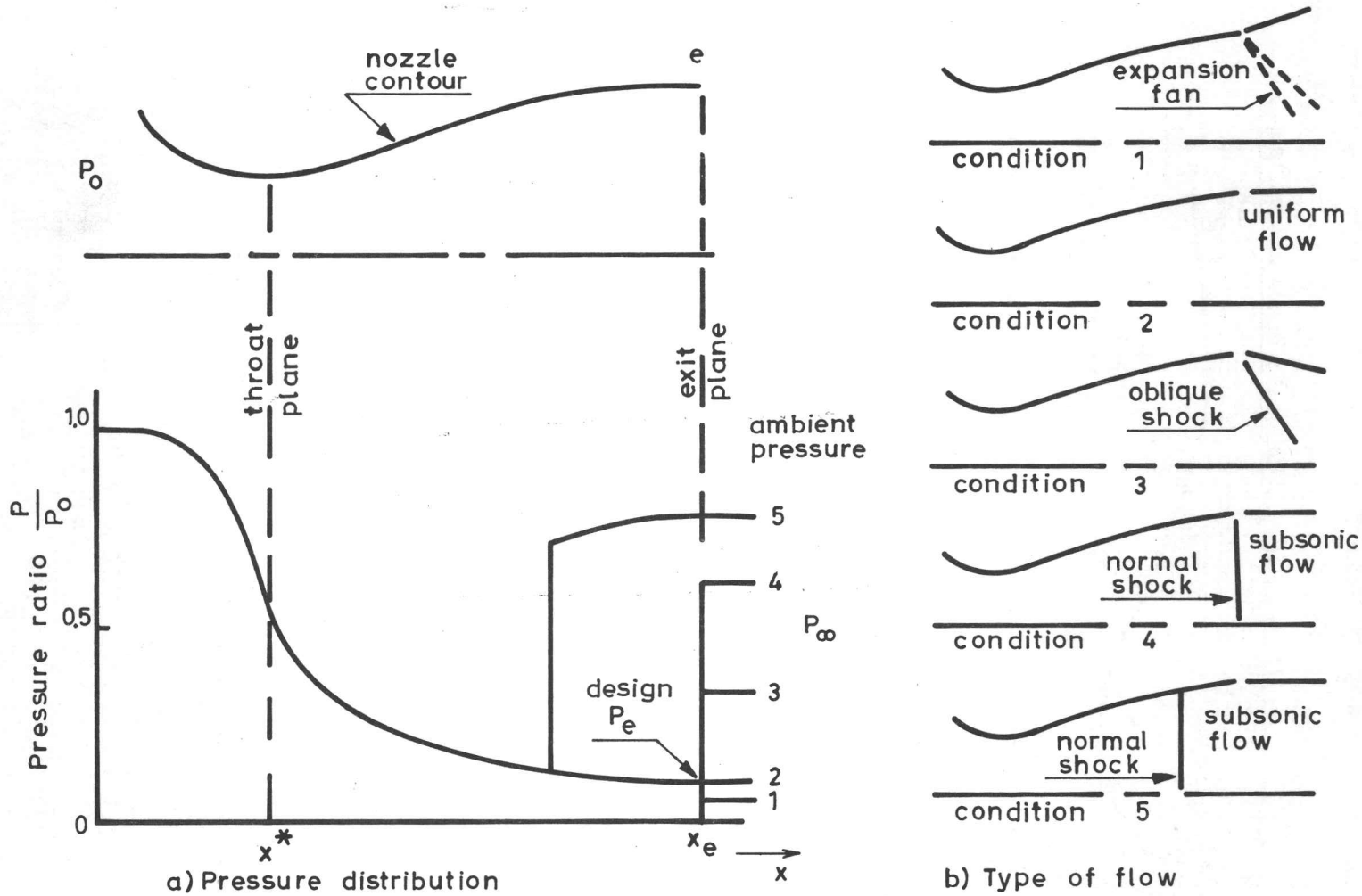

Fig. 1-3 NOZZLE FLOW WITH VARIABLE AMBIENT PRESSURE (INVISCID FLOW)

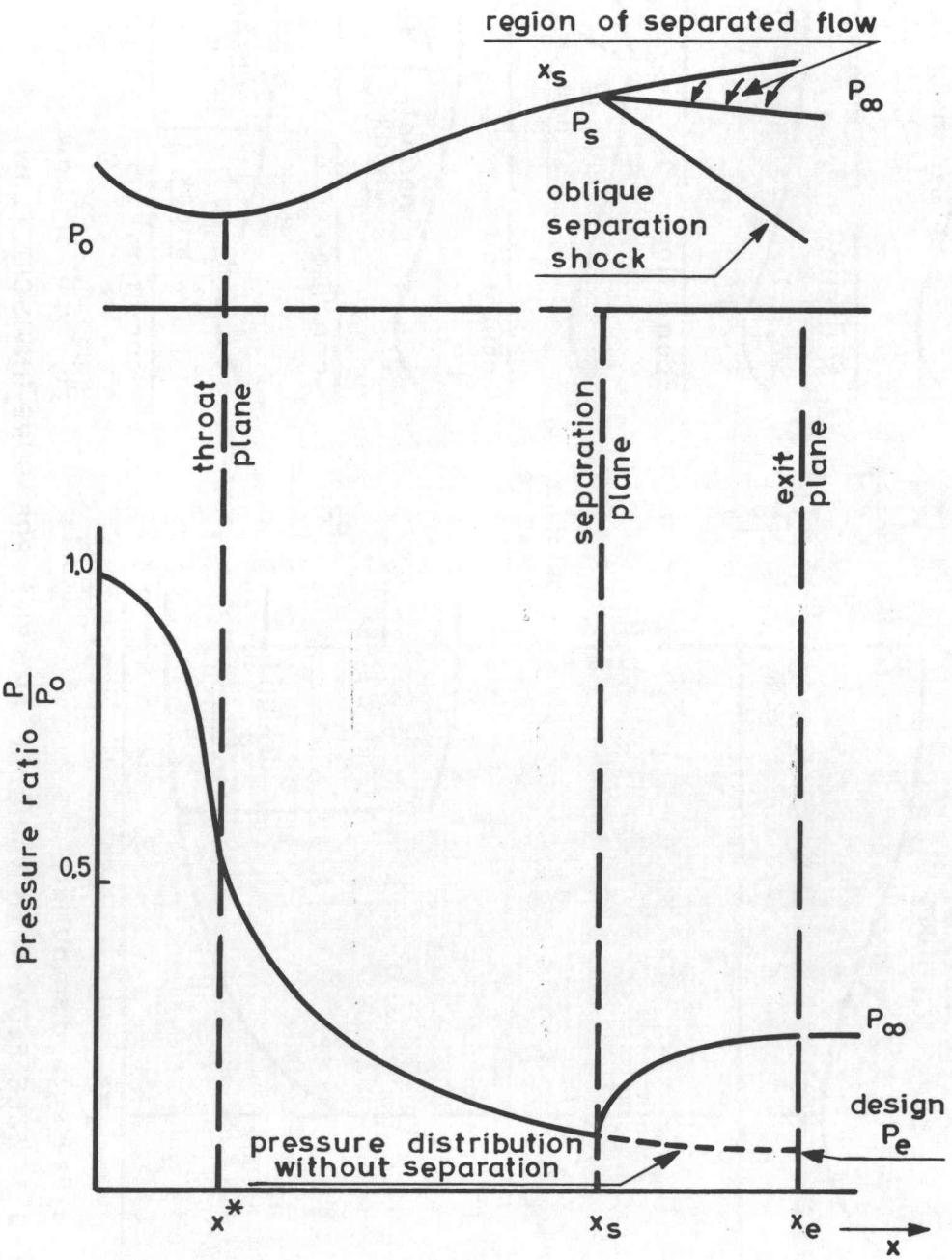

Fig. 1-4 NOZZLE FLOW WITH BOUNDARY LAYER SEPARATION

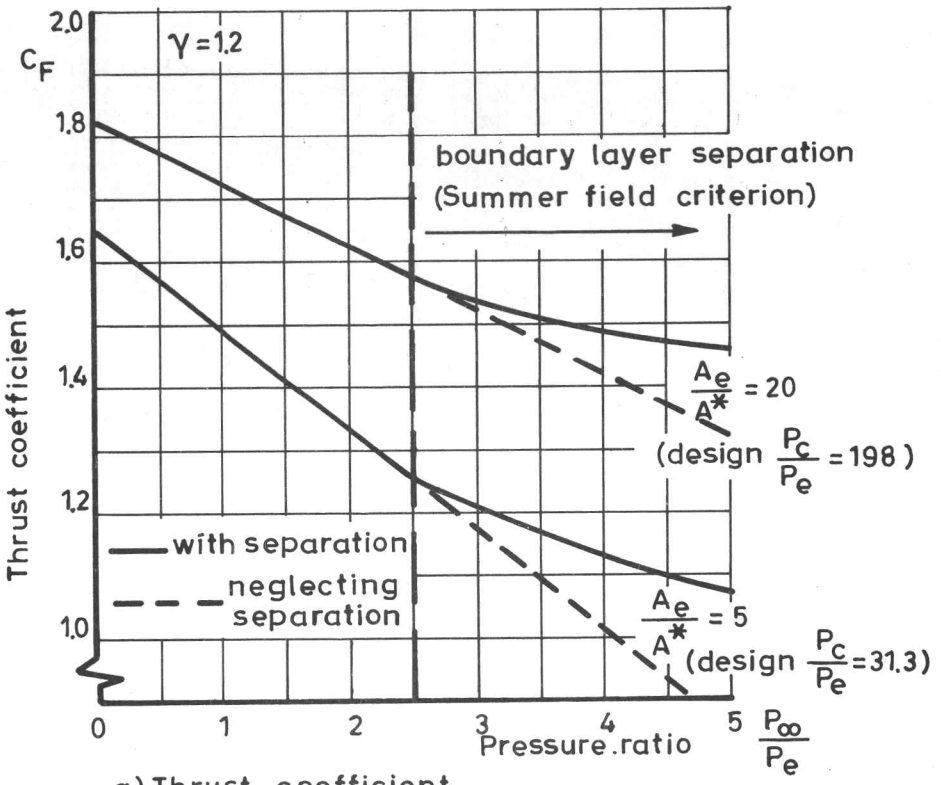

a) Thrust coefficient

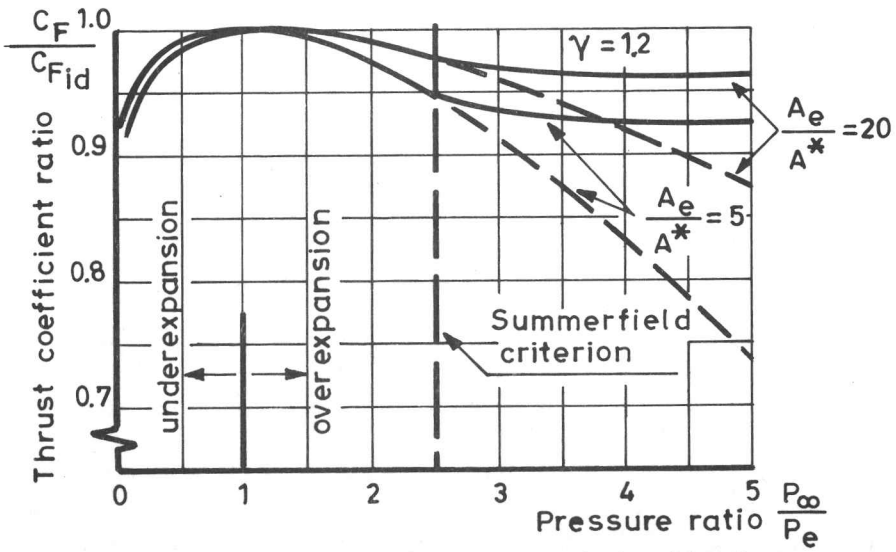

b) Thrust coefficient compared to ideal

Fig. 1-5 EFFECT OF BOUNDARY LAYER SEPARATION ON THRUST COEFFICIENT

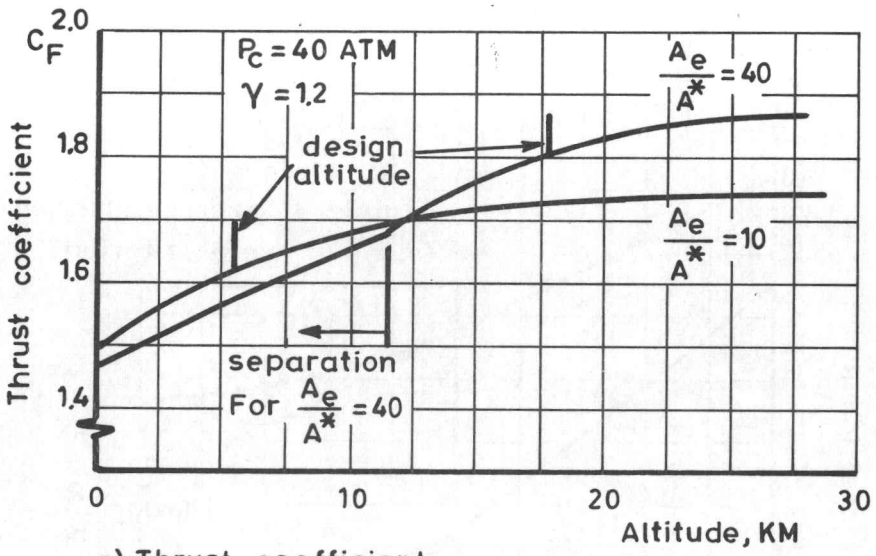

a) Thrust coefficient

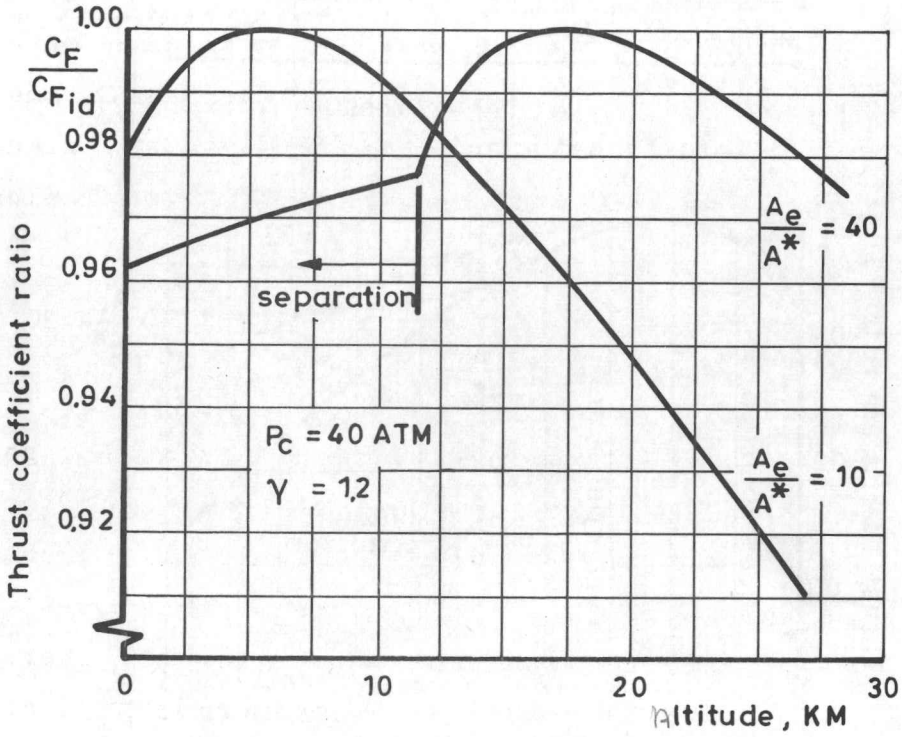

b) Thrust coefficient compared to ideal

Fig. 1-6 VARIATION OF THRUST COEFFICIENT WITH ALTITUDE

CHAPTER 2

CONVENTIONAL CONVERGENT-DIVERGENT NOZZLES

2.1 INTRODUCTION

In Chapter 1 the rocket exhaust nozzle was analyzed with the assumption of one dimensional flow. Now we shall analyze the effect of departure from one dimensional flow. The other assumptions of the one dimensional analysis are retained: adiabatic frictionless flow, perfect gas with constant specific heats, etc.

Rocket exhaust nozzles are nearly always axisymmetric and most of this chapter is on the analysis of axisymmetric flows in nozzles. Some analysis of two dimensional plane flow will be presented to illustrate the techniques for calculating the transonic flow in nozzles.

2.2 CONVERGENT NOZZLE GEOMETRY

The design of the convergent, or subsonic, portion of the rocket nozzle is usually based on considerations of weight and heat transfer. The contour is normally chosen first, and then the flow field is analyzed. The maximum heat transfer in the nozzle occurs just upstream of the throat, therefore it is desirable to make the convergent section as short as possible. Weight considerations also dictate a short convergent section. The desirability of a short convergent section must be balanced against the losses which result from a too rapid convergence of the nozzle (departure from one dimensional flow at the throat).

Barrère, et al. (Ref. 2-1) recommend a toroidal section at the throat, with the convergent geometry either conical or sinusoidal (fig.2-1). Rao (Ref. 2-2) also used a toroidal throat section in his analysis of optimum nozzles, but with a smaller radius of curvature downstream of the throat. (Fig. 2-1). It is generally agreed that the radius of curvature of the toroidal throat section should be 1 to 2 throat radii for the region upstream of the throat. The usual approximate analyses for the shape of the sonic line yield results in terms of only the radius of wall curvature at the throat, and the detailed upstream geometry is ignored.

2.3 TRANSONIC FLOW IN NOZZLES

The design of the supersonic contour by the method of characteristics requires that the shape of the sonic line be known. Actually, the required initial condition for the method of characteristics is a specification of the flow conditions along a line where the flow is everywhere slightly supersonic.

The most common technique for analyzing the transonic flow in nozzles is the use of series expansions. The velocity (or velocity potential) components are expressed as power series of the geometric variables. The series coefficients are evaluated to satisfy the equation of motion for the flow. Of course, the accuracy of the technique depends on the number of terms in the power series.

2.3.1 Basic equations

The basic equations used in the analysis of transonic and supersonic flow in nozzles are (1) equation of irrotationality (2) continuity equation, (3) Euler equation, and (4) definition of the speed of sound.

Equation of irrotationality

$$\frac{\partial u}{\partial y} = \frac{\partial v}{\partial x} \qquad (2\text{-}1)$$

Continuity equation

$$\frac{\partial (\rho u)}{\partial x} + \frac{\partial (\rho v)}{\partial y} = 0 \qquad \text{(two dimensional)} \qquad (2\text{-}2)$$

$$\frac{\partial (\rho u)}{\partial x} + \frac{1}{y} \frac{\partial (\rho v y)}{\partial y} = 0 \qquad \text{(axisymmetric)} \qquad (2\text{-}3)$$

Euler equation

$$dp = -\rho d\left(\frac{V^2}{2}\right) \qquad (2\text{-}4)$$

Speed of sound

$$c^2 = \frac{dp}{d\rho} \qquad (2\text{-}5)$$

Equation of motion - The preceding equations may be combined to derive the equation of motion for the potential flow. For two dimensional flow:

$$\left(1-\frac{u^2}{c^2}\right)\frac{\partial u}{\partial x}+\left(1-\frac{v^2}{c^2}\right)\frac{\partial v}{\partial y}-\frac{2uv}{c^2}\frac{\partial u}{\partial y}=0 \qquad (2\text{-}6)$$

For axisymmetric flow:

$$\left(1-\frac{u^2}{c^2}\right)\frac{\partial u}{\partial x}+\left(1-\frac{v^2}{c^2}\right)\frac{\partial v}{\partial y}-\frac{2uv}{c^2}\frac{\partial u}{\partial y}+\frac{v}{y}=0 \qquad (2\text{-}7)$$

Note: In this section, for consistency, y will be used for the radial coordinate in axisymmetric flow. In general, r will be used for the radial coordinate.

2.3.2 Analysis of Oswatitsch

One of the earlier uses of the power series technique was by Oswatitsch and Rothstein (Ref. 2-3). Consider the flow through a symmetrical two dimensional nozzle with arbitrary wall contour, $y_w = F(x)$. (For convenience, we may take F = 1 at the throat).

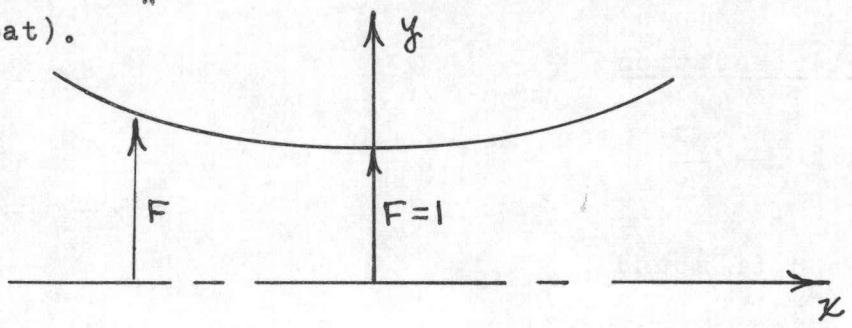

It is assumed that the velocity components, u and v, may be represented by a power series in y, with the coefficients in the series taken as functions of x. Because the flow is symmetrical about the x-axis, the series for u must contain only even powers of y, and the series for v only odd powers.

$$\left.\begin{aligned} u &= a_o + \frac{1}{2!} a_2 y^2 + \frac{1}{4!} a_4 y^4 + \cdots \\ v &= b_1 y + \frac{1}{3!} b_3 y^3 + \cdots \end{aligned}\right\} \qquad (2\text{-}8)$$

Note that a and b are functions of x.
Differentiating eqs.(2-8) and substituting into eq. (2-1) results in

$$a_2 y + \frac{1}{3!} a_4 y^3 = b_1' y + \frac{1}{3!} b_3' y^3 \qquad (2\text{-}9)$$

where the ppimes denote differentiation with respect to x. Eq.(2-9) must be true for all values of y, therefore, the coefficients of like powers of y must be equal.

$$\left.\begin{aligned} a_2 &= b_1' \\ a_4 &= b_3' \end{aligned}\right\} \qquad (2\text{-}10)$$

Now write eq.(2-6) in a different form:

$$(c^2 - u^2)\frac{\partial u}{\partial x} + (c^2 - v^2)\frac{\partial v}{\partial y} - 2uv\,\frac{\partial u}{\partial y} = 0 \qquad (2\text{-}6a)$$

By using the relation $c^2 = \frac{\gamma-1}{2}(V_{max}^2 - V^2)$, we may write (with $V^2 = u^2 + v^2$)

$$(c^2 - u^2) = \frac{\gamma-1}{2}(V_{max}^2 - v^2) - \frac{\gamma+1}{2} u^2$$

and

$$(c^2 - v^2) = \frac{\gamma-1}{2}(V_{max}^2 - u^2) - \frac{\gamma+1}{2} v^2$$

Equation (2-6a) then becomes

$$\left[\frac{\gamma-1}{2}(V_{max}^2 - v^2) - \frac{\gamma+1}{2} u^2\right]\frac{\partial u}{\partial x} + \left[\frac{\gamma-1}{2}(V_{max}^2 - u^2) - \frac{\gamma+1}{2} v^2\right]\frac{\partial v}{\partial y}$$

$$- 2uv \frac{\partial u}{\partial y} = 0 \qquad (2\text{-}6b)$$

Now obtain the derivatives from eq.(2-8), substitute them into eq.(2-6b) and retain only the terms independent of y. The result is

$$b_1 = - \frac{(V_{max}^2 - \frac{\gamma+1}{\gamma-1} a_o^2)}{(V_{max}^2 - a_o^2)} a_o' \qquad (2\text{-}11)$$

Boundary conditions - At the wall of the nozzle

$$\frac{v_w}{u_w} = \frac{dy_w}{dx} = \frac{dF}{dx} = F' \qquad (2\text{-}12)$$

At the wall, eq.(2-8) becomes

$$u_w = a_o + \frac{1}{2} a_2 F^2 + \frac{1}{24} a_4 F^4$$

and

$$v_w = b_1 F + \frac{1}{6} b_3 F^3$$

From eq.(2-12), $v_w = F' u_w$, thus

$$b_1 F + \frac{1}{6} b_3 F^3 = F'(a_o + \frac{1}{2} a_2 F^2 + \frac{1}{24} a_4 F^4)$$

From eq.(2-10), $a_4 = b_3'$, and

$$b_1 F + \frac{1}{6} b_3 F^3 = F'(a_o + \frac{1}{2} a_2 F^2 + \frac{1}{24} b_3' F^4) \qquad (2\text{-}13)$$

Calculation procedure - The coefficient a_o corresponds to the velocity distribution on the x-axis. If the nozzle contour is given, and if a_o is known, then it is possible to

1. Compute $b_1(x)$ from eq.(2-11)
2. Compute $a_2(x)$ from eq.(2-10)
3. Integrate eq.(2-13) numerically for $b_3(x)$
4. Compute $a_4(x)$ from eq.(2-10)

All of the coefficients would be known, and the flow field would be established to the fourth power of y.

Conservation of mass flow - The mass flow through the nozzle is used as a control in an iterative procedure to determine $a_o(x)$.

$$\int_o^F \rho u dy = w = \text{constant}$$

The relation for ρ is

$$\frac{\rho}{\rho_o} = \left(1 - \frac{V^2}{V^2_{max}}\right)^{\frac{1}{\gamma-1}}$$

Oswatitsch and Rothstein present the detailed calculation procedure, as well as several approximations to facilitate convergence of the solution. Note that exactly the same procedure is used for the axisymmetric case, except for the different forms for the continuity equation and equation of motion.

Typical results - Lines of constant M* are shown in Fig. 2-2 for two dimensional and axisymmetric flow, both cases having the same hyperbolic wall contour. We see the usual result

that the flow reaches the sonic condition at the wall upstream of the physical throat. The sonic condition on the centerline is not reached until downstream of the physical throat.

2.3.3 Analysis of Sauer

Sauer (Ref. 2-4) obtained approximate, but closed form, rules for the flow in the throat region of a nozzle. He used the concept of a series solution along with an approximate equation of motion.

Basic equations - Define $\hat{u}$ and $\hat{v}$ by

$$\frac{u}{c^*} = 1 + \hat{u}, \quad \frac{v}{c^*} = \hat{v} \tag{2-14}$$

where c^* is the speed of sound at the sonic condition, Equation (2-6), for two dimensional flow, may be linearized in the transonic region (Ref. 2-5, Chapter 21). The assumptions used in the linearization are

$$\left|\frac{u}{c^*} - 1\right| \ll 1$$

and

$$\frac{v}{c^*} \ll 1$$

The following simplified equation is obtained

$$(\gamma+1)\hat{u}\,\frac{\partial \hat{u}}{\partial x} - \frac{\partial \hat{v}}{\partial y} = 0 \tag{2-15}$$

Series formulation - The perturbation velocity potential corresponding to $\hat{u}$ and $\hat{v}$, is written

$$\frac{1}{a^*}\phi = f_o(x) + y^2 f_2(x) + y^4 f_4(x) + \ldots \qquad (2\text{-}16)$$

By differentiating eq.(2-16) we obtain

$$\hat{u} = f_o' + y^2 f_2' + y^4 f_4' + \ldots \qquad (2\text{-}16a)$$

$$\hat{v} = 2y f_2 + 4y^3 f_4 + \ldots \qquad (2\text{-}16b)$$

Taking the derivatives $\frac{\partial \hat{u}}{\partial x}$ and $\frac{\partial \hat{v}}{\partial y}$ and substituting into eq.(2-15) yields

$$(\gamma+1)(f_o' + y^2 f_2' + y_4 f_4')(f_o'' + y^2 f_2'' + y^4 f_4'') = 2f_2 + 12y^2 f_4$$

Equating the coefficients of terms independent of y:

$$(\gamma+1) f_o' f_o'' = 2f_2 \qquad (2\text{-}17)$$

Equating coefficients of terms in y^2:

$$(\gamma+1)(f_o' f_2'' + f_o'' f_2') = 12 f_4 \qquad (2\text{-}18)$$

Note that f_o' represents the velocity distribution on the x-axis, $\left[\hat{u}(x)\right]_{y=0}$.

We now set x = 0 where the sonic line crosses the x-axis. Now assume that for a short distance near the origin f_o' may be represented by a straight line.

$$f_o' \simeq \left(\frac{\partial \hat{u}}{\partial x}\right)_o x \qquad (2\text{-}19)$$

From eqs.(2-17) and (2-18), we evaluate the remaining coefficients (noting that $f''_o = \left(\frac{d\hat{u}}{dx}\right)_o$).

$$f_2 = \frac{\gamma+1}{2}\left(\frac{d\hat{u}}{dx}\right)_o^2 x$$

$$f_2' = \frac{(\gamma+1)}{2}\left(\frac{d\hat{u}}{dx}\right)_o^2$$

$$f_4 = \frac{(\gamma+1)^2}{24}\left(\frac{d\hat{u}}{dx}\right)_o^3$$

$$f_4' = 0$$

The velocity distributions are then

$$\hat{u} = \left(\frac{d\hat{u}}{dx}\right)_o x + \frac{\gamma+1}{2}\left(\frac{d\hat{u}}{dx}\right)_o^2 y^2 \qquad (2\text{-}20a)$$

$$\hat{v} = (\gamma+1)\left(\frac{d\hat{u}}{dx}\right)_o^2 xy + \frac{(\gamma+1)^2}{6}\left(\frac{d\hat{u}}{dx}\right)_o^3 y^3 \qquad (2\text{-}20b)$$

and the approximate velocity field near the origin is defined.

<u>Sonic line</u> - The sonic line is defined as

$$u^2 + v^2 = c^{*2}, \text{ or } (1+\hat{u})^2 + \hat{v}^2 = 1$$

Considering the other assumptions in the theory, we may set $\hat{u} = 0$ at the sonic line. Then, from eq.(2-20a)

$$x^* = -\frac{(\gamma+1)}{2}\left(\frac{d\hat{u}}{dx}\right)_o y^{*2} \qquad (2\text{-}21)$$

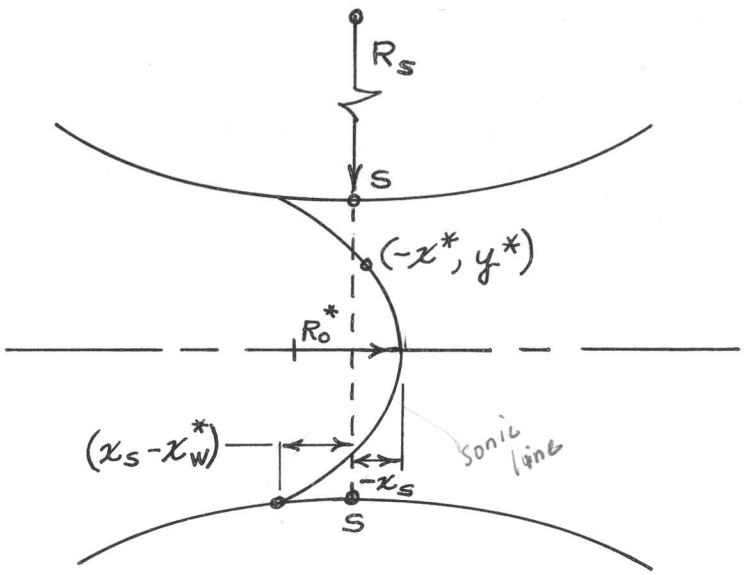

The nomenclature is shown in the sketch, where the asterisk denotes a general point on the sonic line. Eq.(2-21) shows that the sonic line is a parabola, with the curvature on the x-axis given by

$$\frac{1}{R_o^*} = \frac{\frac{d^2x^*}{dy^{*2}}}{\sqrt{1+(\frac{dx^*}{dy^*})^2}} = (\gamma + 1)\,(\frac{d\hat{u}}{dx})_o \qquad (2\text{-}22)$$

We must now locate the sonic line relative to the physical throat plane. In the throat plane, $\hat{v}_s = 0$, therefore from eq.(2-20b)

$$-x_s = \frac{\gamma+1}{6}\,(\frac{d\hat{u}}{dx})_o\, y_s^2 \qquad (2\text{-}23)$$

We now must find where the sonic line intersects the wall. Assuming that $y_w^* = y_s$, and combining eqs(2-21) and (2-23), we get

$$(x_s - x_w^*) = \frac{\gamma+1}{3} \left(\frac{d\hat{u}}{dx}\right)_o y_s^2 = -2x_s \qquad (2\text{-}24)$$

The radius of curvature of the wall at the throat plane will now be evaluated.

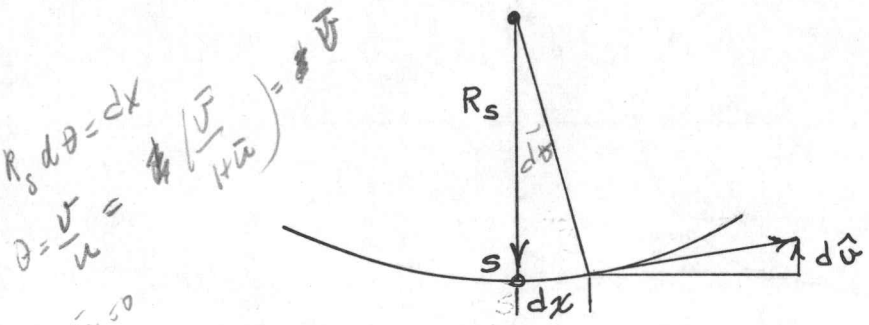

$$\frac{1}{R_s} \approx \frac{\partial \hat{v}}{\partial x}$$

Differentiating eq.(2-20b) yields:

$$\frac{1}{R_s} = (\gamma+1)\left(\frac{d\hat{u}}{dx}\right)_o^2 y_s = \frac{1}{R_o^*} \left(\frac{d\hat{u}}{dx}\right)_o y_s \qquad (2\text{-}25)$$

Sonic line parameters for a given nozzle - The preceding development was based on the known velocity distribution at the axis, $\left(\frac{d\hat{u}}{dx}\right)_o$. Usually, however, it is the shape of the nozzle which is known. The nozzle geometry in the throat region is defined by y_s and R_s, and eqs(2-22)-(2-25) can be written to give the sonic line parameters in terms of the geometric parameters. Using the relation $\left(\frac{d\hat{u}}{dx}\right)_o = \frac{1}{y_s}\left[\frac{d\hat{u}}{d(\frac{x}{y_s})}\right]_o$ in eq.(2-25) yields:

$$\left[\frac{d\hat{u}}{d(\frac{x}{y_s})}\right]_o = \sqrt{\frac{1}{(\gamma+1)} \frac{y_s}{R_s}} \qquad (2\text{-}26)$$

Using eq.(2-26) in eq.(2-22):

$$\frac{R_o^*}{y_s} = \sqrt{\frac{1}{(\gamma+1)} \frac{R_s}{y_s}} \qquad (2\text{-}27)$$

Using eq.(2-26) in eq.(2-24):

$$\frac{x_s - x_w^*}{y_s} = 2 \frac{(-x_s)}{y_s} = \sqrt{\frac{(\gamma+1)}{9} \frac{y_s}{R_s}} \qquad (2\text{-}28)$$

Axisymmetric nozzles - The equations for axisymmetric nozzles may be obtained by a similar development.

$$\frac{x^*}{y_s} = - \frac{(\gamma+1)}{4} \left[\frac{d\hat{u}}{d(\frac{x}{y_s})} \right]_o (\frac{y^*}{y_s})^2 \qquad (2\text{-}29)$$

$$\left[\frac{d\hat{u}}{d(\frac{x}{y_s})} \right]_o = \sqrt{\frac{2}{(\gamma+1)} \frac{y_s}{R_s}} \qquad (2\text{-}30)$$

$$\frac{R_o^*}{y_s} = \sqrt{\frac{2}{(\gamma+1)} \frac{R_s}{y_s}} \qquad (2\text{-}31)$$

$$\frac{(x_s - x_w^*)}{y_s} = - \frac{x_s}{y_s} = \sqrt{\frac{(\gamma+1)}{32} \frac{y_s}{R_s}} \qquad (2\text{-}32)$$

Comparison of plane and axisymmetric nozzles - The sonic line shape for plane and axisymmetric nozzles having the same contour is shown in the following sketch

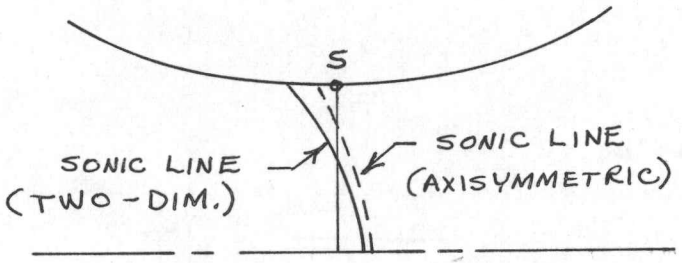

By comparing eqs.(2-26) and (2-30), we see that the rate of increase of centerline velocity at the throat is greater for the axisymmetric case by a factor of $\sqrt{2}$.

Comparison with more exact results - Consider a nozzle having $\frac{R_s}{y_s} = 5$. The following table shows the results of the Sauer approximation as compared to the more exact results of Oswatitsch.

	TWO-DIMENSIONAL		AXISYMMETRIC	
	OSWATITSCH	SAUER	OSWATITSCH	SAUER
$\left[\frac{d\hat{u}}{d(\frac{x}{y_s})}\right]_o$	0.27	0.29	0.37	0.41
$-\frac{x_s}{y_s}$	0.12	0.12	0.14	0.12
$\frac{(x_s - x^*_w)}{y_s}$	0.23	0.23	0.12	0.12

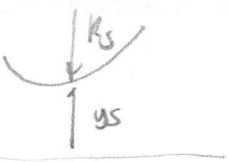

We see that the results of the approximate method are surprisingly accurate for a nozzle having a relatively large radius of curvature, R_s. The Sauer technique is apparently adequate for wind tunnel nozzles in which $\frac{R_s}{y_s} > 5$. The Sauer technique has also been used for the analysis of the transonic flow in rocket nozzles, for example, by Rao.

2.3.4 Analysis of Hall

Hall (Ref. 2-6) has developed higher order series expansion solutions for two dimensional and axisymmetric flow. For axisymmetric nozzles, and two dimensional nozzles symmetrical about the axis, the nozzle wall is represented by

$$y_w = 1 + \frac{x^2}{2R_s} + \sigma \frac{x^4}{8R_s^3} + O(x^6) \qquad (2\text{-}33).$$

where $\sigma = 1$ for a circular arc
$\sigma = 0$ for a parabolic arc
$\sigma = -1$ for a hyperbolic arc

The coordinates are made dimensionless by dividing by the nozzle throat half height, y_s (same nomenclature as used in Sauer's analysis). Hall used the same basic equations as Oswatitsch (section 2.3.1), but represented the perturbation velocities, $\hat{u}$ and $\hat{v}$, by a power series in R_s^{-1}.

$$\hat{u} = \frac{u_1(y,z)}{R_s} + \frac{u_2(y,z)}{R_s^2} + \frac{u_3(y,z)}{R_s^3} + \ldots \qquad (2\text{-}34)$$

$$\hat{v} = \left[\frac{\gamma+1}{(1+\omega)R_s}\right]^{\frac{1}{2}} \left[\frac{v_1(y,z)}{R_s} + \frac{v_2(y,z)}{R_s^2} + \frac{v_3(y,z)}{R_s^3} + \ldots\right] \qquad (2\text{-}35)$$

$\omega = 0$ for two dimensional flow

$\omega = 1$ for axisymmetric flow

The coordinate z is related to x by

$$x = \left[\frac{\gamma+1}{(1+\omega)R_s}\right]^{\frac{1}{2}} z$$

A first approximation is obtained by considering only the first term in eqs.(2-34) and (2-35), and is equivalent to using a linearized form of the equation of motion (eq. 2-6 or eq. 2-7). Hall's first order solution is equivalent to Sauer's solution, or to the first approximation suggested by Oswatitsch. Hall has worked out analytical expressions for the u(y,z) and v(y,z) terms in eqs.(2-34) and (2-35), up to and including the third order terms. The expressions are quite lengthy , and will not be included here.

Hall concluded that, up to the third order terms, the solution is independent of σ in eq.(2-33).

Results for axisymmetric flow - The results for $\frac{u}{c^*}$ and $\frac{v}{c^*}$ at the throat plane are presented in the following tables for various values of the throat radius of curvature, R_s. The values in the tables were calculated for $\gamma = 1.4$

$R_s = 10$

y	$\frac{u}{c^*}$			$\frac{v}{c^*}$		
	One term	Two terms	Three terms	One term	Two terms	Three terms
0	.9750	.9775	.9771	0	0	0
0.5	.9875	.9881	.9881	-.0072	-.0060	-.0068
1.0	1.0250	1.0238	1.0240	0	0	0

$R_s = 5$

y	$\frac{u}{c^*}$			$\frac{v}{c^*}$		
	One term	Two terms	Three terms	One term	Two terms	Three terms
0	.9500	.9599	.9570	0	0	0
0.5	.9550	.9565	.9562	-.0216	-.0146	-.0153
1.0	1.0500	1.0452	1.0464	0	0	0

$R_s = 1.5$

y	$\frac{u}{c^*}$			$\frac{v}{c^*}$		
	One term	Two terms	Three terms	One term	Two terms	Three terms
0	.8333	.9432	.8344	0	0	0
0.5	.9167	.9447	.9333	-.1307	.0113	-.0406
1.0	1.1667	1.1134	1.1500	0	0	0

We see that the first order solution is satisfactory for $R_s = 10$ and $R_s = 5$. Also the first order solution is somewhat better for $\frac{u}{c^*}$ than for $\frac{v}{c^*}$. For $R_s = 1.5$, however, the series obviously has not converged, and more terms would be required to obtain a reliable solution.

Mass flow in the nozzle - One result of the nonuniform flow at the throat is that the mass flow is different from the one dimensional value. For an axisymmetric nozzle, Hall derived the following equation for the ratio of mass flow to the one dimensional mass flow:

$$\frac{w}{w_{ideal}} = 1 + \frac{\gamma+1}{R_s^2}\left[\frac{1}{96} + \frac{8\gamma+21}{4608 R_s} + \frac{745\gamma^2+1971\gamma+2007}{552\,960\,R_s^2} + \cdots\right] \qquad (2\text{-}36)$$

The deviation from the one dimensional mass flow is shown in the following table, for $\gamma = 1.4$.

R_s	$1 - \frac{w}{w_{id}}$		
	One term	Two terms	Three terms
1.5	0.0111	0.0062	0.0116
3.0	0.00277	0.00215	0.00249
5	0.00100	0.00087	0.00091
10	0.00025	0.00023	0.00024

Again, we see that the series solution has not converged for the lower values of R_s. Also, we see that the mass flow through the nozzle is less than the one dimensional flow, but by a relatively small amount.

2.3.5 Other analytical techniques

From the results shown in the preceding section, it is obvious that a large number of terms in the series solution would be required to accurately calculate the transonic flow for the small values of R_s which are used in rocket nozzles. Perhaps as many as 20 or 30 terms would be required for some nozzle geometries. Unfortunately, the algebra becomes so cumbersome for series solutions with more than three terms that the problem can only be satisfactorily solved on a high speed digital computer.

It would also be possible to apply the relaxation technique of Emmons (Ref. 2-7) to the problem of the transonic nozzle flow. Again, the calculations would be so lengthy as to require the use of a high speed digital computer. It is unlikely that the relaxation procedure would offer any computational advantages over the series expansion technique. The primary usefulness of the relaxation technique is for calculating accelerating-decelerating nozzle flow with shock waves in the region of the throat.

Ahlberg et al. (Ref. 2-8) have suggested that the streamline curvature technique of Valentine (Ref. 2-9) could be applied to the transonic flow in nozzles. They stated that initial results using Valentine's method were sufficiently

promising to justify replacement of the series expansion technique. Valentine treated the case of two dimensional subsonic flow in curved channels, and developed a graphical technique for the solution. Unfortunately, the details of the extension of the technique to axisymmetric nozzle flow have not yet been published in the open literature.

2.3.6 Transonic flow in annular nozzles

Although annular rocket nozzles (plug, E-D, etc) will be discussed in another section, brief attention will be given here to the transonic flow in such nozzles. The general flow direction in the throat region is usually inclined to the axis of symmetry; the inclination, β, may be as large as 90°. Rao (Ref. 2-10) treated the case of $\beta = 90°$ and a throat contour which was symmetrical about its own centerline, using the approximate Sauer technique. Lord (Ref. 2-11) treated the case of the transonic flow in a nozzle with a constant diameter centerbody ($\beta = 0$). Lord used a series expansion technique similar to Hall's (Ref. 2-6), and considered the indirect problem where the axial velocity distribution is specified and the nozzle wall contour is calculated.

The general case of an arbitrary value of β and arbitrary throat profile has been recently considered by Moore and Hall (Ref. 2-12). They considered the direct problem (specified geometry) and also used the series expansion technique of Hall. The solution is considerably more complex than for the case of a conventional two dimensional or axisymmetric nozzle, and only the first order solution was obtained. For the special case of $\beta = 0$, the series solution was evaluated up to and including third order terms.

2.4 IDEAL SUPERSONIC NOZZLES

The design of the ideal supersonic nozzle will be considered in this section. An ideal nozzle is one with uniform and parallel flow at the exit plane.

2.4.1 Method of characteristics

The method of characteristics is the fundamental technique used for the analysis of supersonic nozzle flow. Detailed discussions of the method of characteristics are presented in basic references on supersonic aerodynamics, for example, Refs. 2-5 and 2-13.

For steady axisymmetric flow, the equation of motion (eq. 2-7) may be written in terms of the velocity potential, ϕ, as

$$(c^2 - \phi_x^2)\phi_{xx} - 2\phi_x\phi_r\phi_{xr} + (c^2 - \phi_r^2)\phi_{rr} + \frac{c^2}{r}\phi_r = 0 \qquad (2\text{-}37)$$

where the subscripts x and r represent differentiation by the respective independent variable. Equation (2-37) is of the general form

$$A\phi_{xx} + 2B\phi_{xr} + C\phi_{rr} = D$$

For supersonic flow, $B^2 - AC$ is positive, therefore, eq.(2-37) is a second order hyperbolic partial differential equation with two independent variables. For such "quasi-linear"

equations (linear in derivatives of highest order), the solutions are such that two families of "characteristic curves" exist. Along each family of characteristics the variables are related by a pair of second order ordinary differential equations. For steady flow, the characteristics in the physical plane correspond to the Mach lines. The advantage of the method of characteristics is that, instead of the difficult task of solving eq.(2-37), we have the relatively simple task of solving simultaneously the two pairs of ordinary differential equations. The solution is further simplified in that the variables of interest are the differentials ϕ_x and ϕ_r, therefore, we must integrate the equations only once.

The differential equations along the Mach lines are:

$$\left(\frac{dr}{dx}\right)_{I,II} = \frac{-uv \pm c\sqrt{u^2 + v^2 - c^2}}{c^2 - u^2} - \frac{c^2 v}{c^2 - v^2}\frac{1}{r}\left(\frac{dr}{du}\right)_{I,II} \qquad (2\text{-}38)$$

$$\left(\frac{dv}{du}\right)_{I,II} = \frac{uv \pm c\sqrt{u^2 + v^2 - c^2}}{c^2 - v^2} \qquad (2\text{-}39)$$

The upper sign refers to family I characteristic lines, and the lower sign to family II. The family I lines are called "right running" and the family II lines "left running".

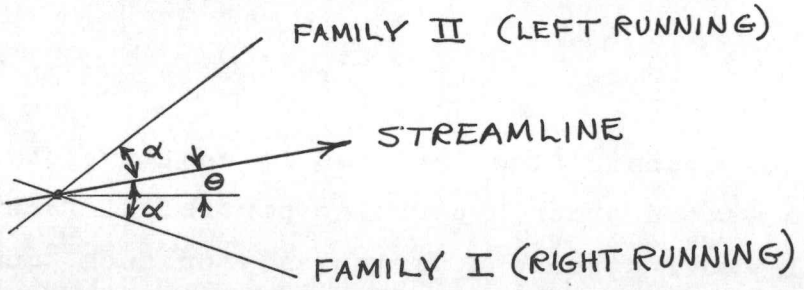

The characteristics in the physical plane are inclined at the Mach angle, α, to the streamlines.

Calculation procedure - Consider a small unit process in the physical plane:

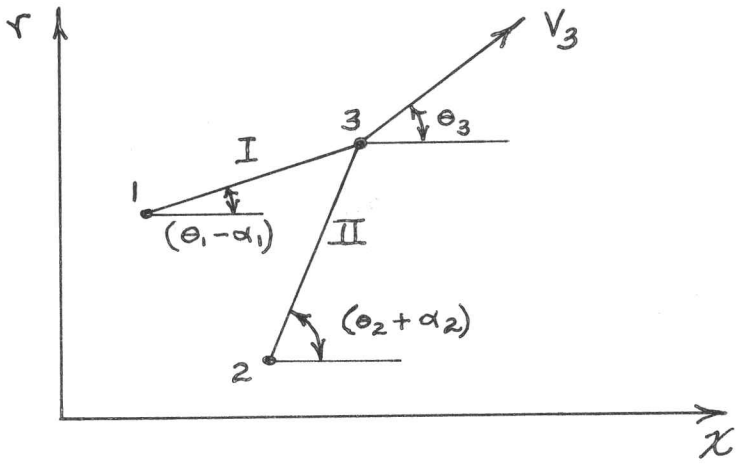

For the small unit process we may consider the Mach lines to be straight, with the slopes taken as the average of the slopes at the end points. The following difference equations result from eqs. (2-38) and (2-39):

$$r_3 - r_1 = (x_3 - x_1)\tan(\theta - \alpha)_{1-3} \qquad (2\text{-}40a)$$

$$r_3 - r_2 = (x_3 - x_2)\tan(\theta + \alpha)_{2-3} \qquad (2\text{-}40b)$$

$$\theta_3 - \theta_1 + Q_{1-3}(V_3 - V_1) - \left(\frac{G}{r}\right)_{1-3}(r_3 - r_1) = 0 \qquad (2\text{-}41a)$$

$$\theta_3 - \theta_2 - Q_{2-3}(V_3 - V_2) + \left(\frac{F}{r}\right)_{2-3}(r_3 - r_2) = 0 \qquad (2\text{-}41b)$$

The following abbreviations have been used:

$$Q = \frac{\cot\alpha}{V}$$

$$F = \frac{\sin\theta\sin\alpha}{\sin(\theta+\alpha)}$$

$$G = \frac{\sin\theta\sin\alpha}{\sin(\theta-\alpha)}$$

As a first approximation,we may evaluate the coefficients which are averaged over the interval by the values at the initial point. Thus $\tan(\theta-\alpha)_{1-3}$ becomes $\tan(\theta_1-\alpha_1)$, etc. We may then solve eqs.(2-40) and (2-41) for the unknowns r_3, x_3, V_3 and θ_3. Using these values we may recalculate using the averaged coefficients, and then repeat the procedure until the solution converges.

Using suitable initial and boundary conditions, we may calculate the entire downstream flow field by this step by step procedure. The overall accuracy of the method depends only on the interval size and the degree of accuracy of each unit calculation. It should be noted that small errors are cumulative because the conditions at each calculated point become the initial conditions for the next succeeding point, etc. With modern high speed digital computers, the number of individual calculations is no problem, and the method of characteristics is a reliable and highly accurate analytical tool.

2.4.2 Nozzle design procedure

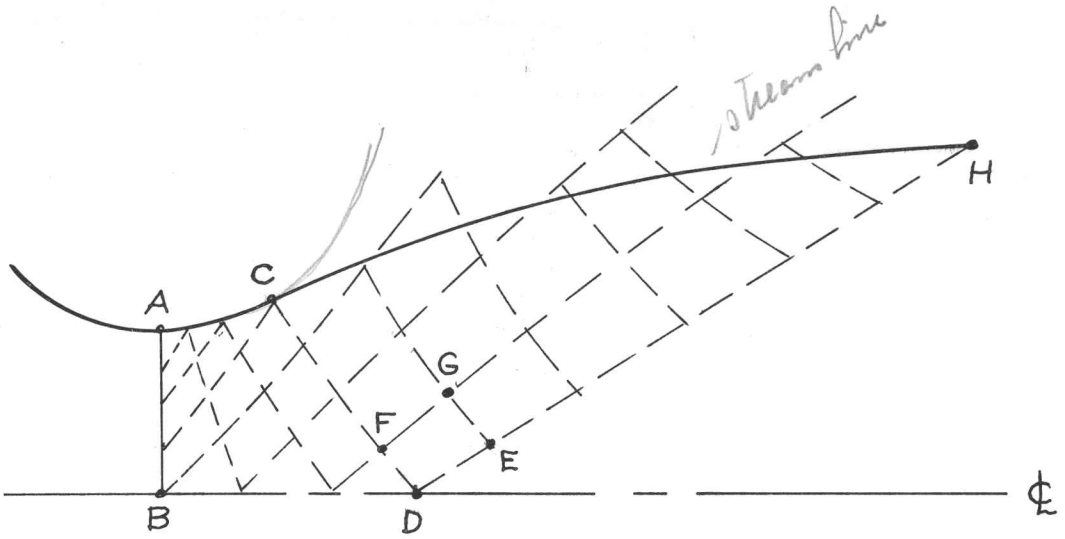

It is assumed that V and θ are known along a line A-B, where the flow is entirely supersonic. The wall downstream of A may be curved outward arbitrarily. The characteristics network is started at several points along AB, and constructed in a region bounded by the wall and by the centerline. The expansion is continued until the design Machnumber is reached on the nozzle axis (point D). Point C, at the wall, lies on the same family I characteristic as D. The arbitrary curvature of the nozzle is stopped at C. Downstream of C, the wall must be shaped to provide uniform and parallel flow at the nozzle exit plane.

The Mach line extending downstream from D must be straight because it bounds uniform and parallel flow. Several points are chosen along this Mach line to be the end points of family I characteristics. Take point E as an example. The flow conditions are also known at point F, therefore, eqs. (2-40) and (2-41) may be used to calculate the conditions at G. In this manner, the flow field is constructed in the region

bounded by CD and the Mach line extending from D. The streamline angle is known at every point in the characteristics network.

The streamline of interest is the one passing through C because this gives the desired nozzle contour, C-H. Most aerodynamic textbooks recommend a step by step extrapolation procedure on θ to determine the streamline C-H. A more accurate procedure is to use a mass integral to determine the shape of the boundary streamline:

$$2\pi \int_{o}^{r_w} \rho V \cos\theta r dr = w = \text{constant}$$

The mass flow, w, is known from the conditions along AB.

The shortest possible ideal nozzle is obtained when AC is collapsed to a point, with a sharp corner at A. Even the sharp cornered nozzle is approximately twice as long as the nozzles which are normally used for rockets. Weight and length considerations prohibit the use of ideal nozzles, even though some loss in performance results from the use of shorter nozzles.

2.5 CONICAL NOZZLES

The simplest geometric shape for a supersonic nozzle is a truncated cone. Typically, the nozzle wall angle is about 15°. Although the thrust is less than ideal, such conical nozzles are short and light, and are easy to manufacture. Consequently, most early rockets were equipped with conical nozzles, and many solid propellant rockets are so equipped today.

2.5.1 Source flow in conical nozzles

The flow in conical nozzles is approximately source-like in nature. The streamlines in the divergent section appear to originate from a point upstream of the throat, and the isobaric surfaces are concentric spherical caps.

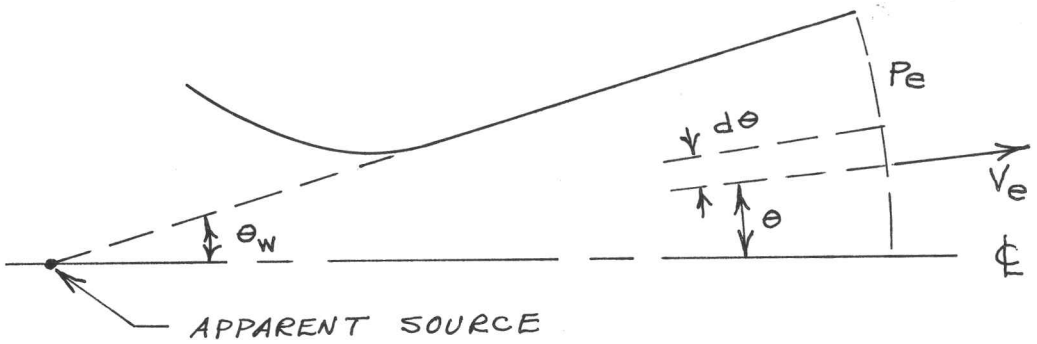

The spherical cap intersecting the nozzle lip has the pressure p_e and the velocity V_e. The axial component of thrust for the annular area between θ and $(\theta+d\theta)$ is

$$dF = \rho_e V_e(2\pi r\sin\theta r d\theta)(V_e\cos\theta)+(p_e-p_\infty)(2\pi r\sin\theta r d\theta)\cos\theta$$

Integrating with respect to θ, from 0 to θ_w, gives

$$F = \left(\frac{1+\cos\theta_w}{2}\right)\left[wV_e+(p_e-p_\infty)A_e'\right] \qquad (2\text{-}42)$$

The variables p_e, A_e' and V_e are those along the spherical cap, not in the exit plane. For small divergence angles A_e' is very nearly equal to A_e, therefore the quantity in brackets may be considered the thrust of an ideal nozzle with parallel flow at the exit. We see then that the deviation in thrust caused

by flow divergence is

$$\lambda = \left(\frac{1+\cos\theta_w}{2}\right) \qquad (2\text{-}43)$$

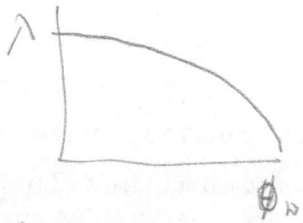

The divergence loss factor, λ, is shown in fig. 2-3 for values of θ_w from 0 to 50°. The loss for a nozzle with $\theta_w = 15°$ is only 1.7% .

Departure from source flow - If the flow at the throat of a conical nozzle were source-like, the method of characteristics would predict source flow throughout the nozzle. Migdal and Landis (Ref. 2-14) have investigated theoretically the effect of transonic nozzle geometry on the thrust of conical nozzles. The flow at the throat section was assumed to be uniform and parallel, with various transition contours downstream of the throat (fig. 2-4). Frictional effects were neglected in the analysis, and the method of characteristics was modified to include the formation of weak shock waves.

The results for the transition geometries of figs. 2-4b and 2-4c are shown in fig. 2-5. Even though the flow may be substantially different from source flow, the effect on thrust efficiency ($C_{F_v}/C_{F_{vid}}$) is small. Fig. 2-5 also indicates that the positive curvature transition yields thrust efficiencies which are closer to the source flow prediction than does the negative curvature transition.

Migdal and Landis also investigated the effect of sonic line curvature on the thrust performance of conical nozzles. They found that the results varied insignificantly

from the results of fig. 2-5, provided that the subsonic nozzle contour was reasonably smooth.

Migdal and Landis found that the departures from source flow were greatest just downstream from the throat. The thrust efficiency of the low area ratio portion of the nozzle was lowest for those nozzles with sharp corners. This is consistent with the rapid reduction of wall pressure which is encountered in such nozzles.

In general, a shock wave is formed in the conical nozzle flow field, although the presence of the shock is not shown by inspection of the wall pressure distributions. The mechanism of the shock formation is discussed by Darwell and Badham (Ref. 2-15) and by Migdal and Kosson (Ref. 2-16).

The theoretical centerline pressure distribution in a 15° conical nozzle with a positive curvature transition section is shown in fig. 2 of Ref. (2-16). The shock becomes weaker and moves downstream as the radius of wall curvature, R_c, is increased. The presence of shocks in the conical nozzle flow field has a relatively small effect on the thrust performance, however, the altered flow field may have a significant effect on the rate of chemical reactions in the nozzle.

2.5.2 Experimental results on conical nozzles

There have been many experimental investigations on the performance of conical nozzles, usually with air as the working fluid. Early U.K.research on conical nozzles is

described in Refs. 2-17 and 2-18. It was found that the source flow equation for the nozzle thrust (eq. 2-43) predicts the trend of C_F vs θ_w up to $\theta_w = 45°$.

More recently, Campbell and Farley (Ref. 2-19) made experiments on conical nozzles, using air as the working fluid. Nozzles with $\theta_w = 15°$, 25° and 29° were operated at area ratios of 10 and 25. Again, the trend of eq. (2-43) was verified.

Bloomer, et al (Ref. 2-20) have presented extensive and very precise experimental results on conical nozzles, using an O_2-JP-4 rocket to provide the working fluid. The nozzle half angle, θ_w, was varied from 15° to 30°, and the area ratio from 8 to 75. Throat geometry consisted of a circular arc section ($R_s = 1.78r^*$) extended to tangency with the conical supersonic section. The thrust performance of the various conical nozzles is shown in fig. 2-6. Bloomer, et al., operated the rocket without a divergent nozzle, and thereby determined the thrust loss in the convergent section. The data points of fig. 2-6 have been corrected so the divergent nozzle is not penalized by the inefficiency of the convergent section.

Bloomer, et al., estimated the distribution of the thrust losses in the entire nozzle system, and the results are shown in fig. 2-7. As would be expected, the divergence losses are a relatively larger fraction for the 25° nozzle as compared to the 15° nozzle.

It was also shown in Ref. 2-20 that the optimum value of θ_w is 20°-25° for a nozzle of a specified length exhausting into a vacuum.

2.6 OPTIMUM ROCKET EXHAUST NOZZLES

The ideal nozzle with parallel and uniform exit flow is excessively long and heavy for rocket applications. On the other hand, very short conical nozzles produce substantially less thrust than the ideal nozzle. Obviously, there must be an optimum nozzle configuration somewhere between the ideal nozzle and the conical nozzle. The problem of determining an optimum nozzle of limited length was attacked by several investigators with a semi-empirical approach (for example, Dillaway, Ref. 2-21). Guderley and Hantsch (Ref. 2-22) attacked the problem in a mathematically rigorous approach using the calculus of variations. Rao (Ref. 2-2) took a similar but somewhat simpler approach, and his development will be presented here. It is noteworthy that the "Rao" nozzle is now widely used for liquid propellant rocket engines.

2.6.1 Analysis of Rao

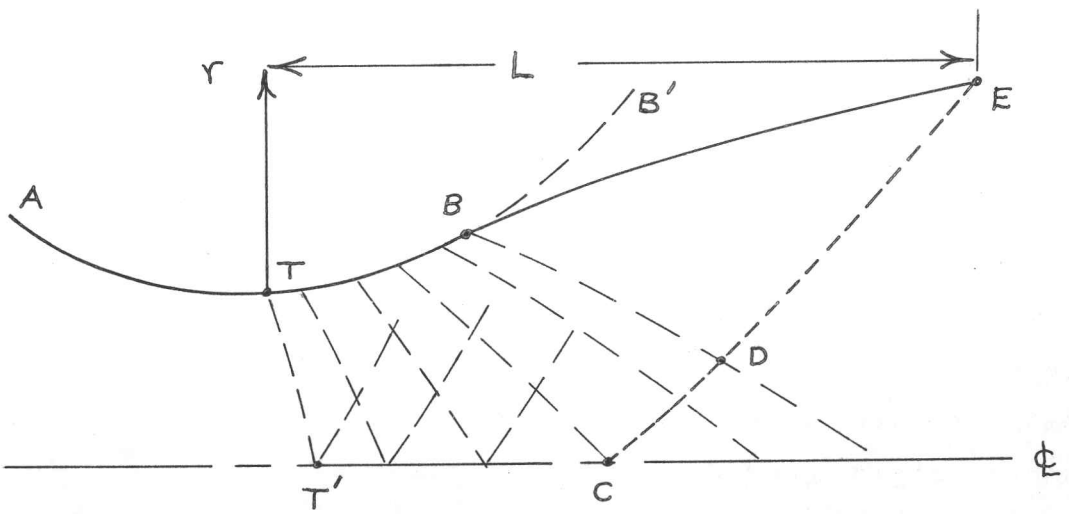

Let ATBE represent the nozzle contour. AT is the convergent portion of the nozzle and TBE is the divergent portion. The slightly supersonic flow along TT' is assumed to be known (Rao used Sauer's method). The initial expansion is generated by the contour TB, and the contour BE turns the flow toward parallel.

Initial expansion - The initial expansion contour, TBB', is selected arbitrarily. A number of points on TB' are used to generate the method of characteristics in the central portion of the nozzle flow field. The basic problem is to determine the amount of expansion along TB' which will yield maximum thrust, with the condition that L is specified.

The flow in the central part of the flow field is unaffected by the nozzle wall contour downstream of B. This central net of characteristics which is unaffected by BE is called by Rao the "kernel" of the flow field. In other words, the basic problem is to determine the extent of the "kernel" such that nozzle thrust is maximized for a given nozzle length.

Formulation of problem - Consider a control surface, CE passing through the nozzle exit. The thrust and mass flow will be evaluated along CE. The location of C on the axis, and the local inclination of the control surface, $\phi(r)$ completely define the surface. Point D is the intersection with CE of the family I characteristic originating at B. Consider an elemental length, ds, along CE.

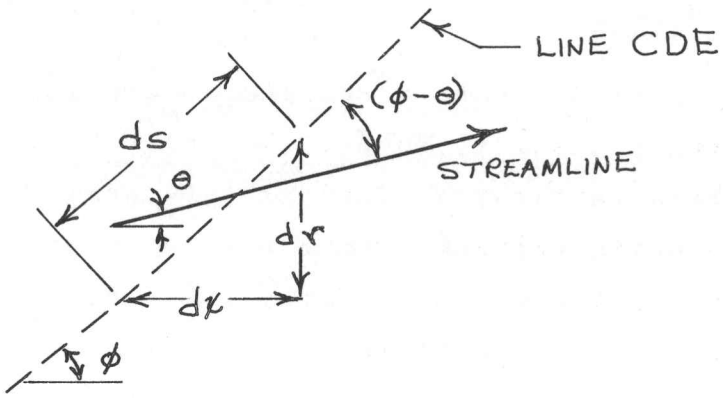

The element of area along CE is $dA = 2\pi r ds$, and $ds = \frac{dr}{\sin\phi}$. The mass flow crossing dA is

$$\rho V \frac{\sin(\phi-\theta)}{\sin\phi} 2\pi r dr$$

Integrating, the total mass flow crossing CE is

$$w = \int_C^E \rho V \frac{\sin(\phi-\theta)}{\sin\phi} 2\pi r dr \qquad (2\text{-}44)$$

Similarly, the thrust is

$$F = \int_C^E \left[(p-p_\infty) + \rho V^2 \frac{\sin(\phi-\theta)}{\sin\phi} \cos\theta \right] 2\pi r dr \qquad (2\text{-}45)$$

The mass flow is fixed by the nozzle throat, therefore, maximizing F is sufficient. The axial distance from C to E is

$$x_E - x_C = \int_C^E \cot\phi dr$$

and the length, L, is

$$L = x_C + \int_C^E \cot\phi dr \qquad (2\text{-}46)$$

If the nozzle contour is changed, the control surface CE correspondingly changes. We can fix point C and vary ϕ to change the control surface. The length L determines the location of C. Because the variations of the nozzle contour are subject to constant length, we may treat C as fixed, and the following condition must be satisfied:

$$\int_C^E \cot\phi\, dr = \text{constant} \tag{2-47}$$

The mass flow is fixed at the throat, which is invariant in this discussion. Therefore, we must maximize the thrust subject to the conditions of eqs. (2-44) and (2-47). Using the Lagrangian multiplier method, the problem is reduced to maximizing the integral

$$I = \int_C^E (f_1 + \lambda_2 f_2 + \lambda_3 f_3)\, dr \tag{2-48}$$

where

$$f_1 = \left[(p-p_\infty) + \rho V^2 \frac{\sin(\phi-\theta)\cos\theta}{\sin\phi} \right] r$$

$$f_2 = \rho V \frac{\sin(\phi-\theta)}{\sin\phi}\, r$$

$$f_3 = \cot\phi$$

and λ_2, λ_3 are Lagrangian multiplier constants.

Solution of problem - The required control surface, and flow conditions along it, are obtained by setting the first variation of I equal zero.

For convenience, the control surface CD is assumed to be a family II characteristic in the "kernel". Therefore, δC, δM and $\delta\theta$ are all zero in this region (δ indicates variation of a function). $\phi = (\alpha+\theta)$ along CD, and $\delta\phi = 0$. The location of D is not known, and $\delta D \neq 0$.

Between D and E, δD, δM, $\delta\theta$ and $\delta\phi$ are all nonzero, as is δ_{r_E}. We require M and θ to be continuous in the flow, and ϕ to be continuous along CDE, therefore, the integrand of eq. (2-48) is continuous. The variation of D does not enter the first variation of I, and we obtain (subscripts denote partial differentiation):

$$\delta I = 0 = \int_{r_D}^{r_E} \Big[(f_{1M}+\lambda_2 f_{2M}+\lambda_3 f_{3M})\delta M + (f_{1\theta}+\lambda_2 f_{2\theta}+\lambda_3 f_{3\theta})\delta\theta + (f_{1\phi}+\lambda_2 f_{2\phi}+\lambda_3 f_{3\phi})\delta\phi \Big]\, dr + \delta r_E (f_1+\lambda_2 f_2+\lambda_3 f_3) \text{ at E} \qquad (2\text{-}49)$$

The variations of M, θ, ϕ and r_E are arbitrary, therefore, along DE

$$f_{1M}+\lambda_2 f_{2M}+\lambda_3 f_{3M} = 0 \qquad (2\text{-}50)$$

$$f_{1\theta}+\lambda_2 f_{2\theta}+\lambda_3 f_{3\theta} = 0 \qquad (2\text{-}51)$$

$$f_{1\phi}+\lambda_2 f_{2\phi}+\lambda_3 f_{3\phi} = 0 \qquad (2\text{-}52)$$

At E

$$f_1+\lambda_2 f_2+\lambda_3 f_3 = 0 \qquad (2\text{-}53)$$

Since f_{3M} and $f_{3\theta}$ are zero, eqs. (2-50) and (2-51) yield

$$f_{1M} f_{2\theta} = f_{1\theta} f_{2M}$$

The variable r drops out of this equation, giving

$$\phi = \theta+\alpha \quad \text{along DE} \qquad (2\text{-}54)$$

therefore, DE coincides with a family II characteristic. Substituting eq. (2-54) into eqs. (2-51) and (2-52), we obtain

$$\frac{V\cos(\theta-\alpha)}{\cos\alpha} = -\lambda_2 \qquad (2\text{-}55)$$

and

$$r\rho V^2 \sin^2\theta\tan\alpha = -\lambda_3 \qquad (2\text{-}56)$$

Eqs. (2-55) and (2-56) are necessary for I to be maximum. Substituting eqs. (2-54) - (2-56) into eq. (2-53) yields

$$\sin 2\theta = \frac{p-p_\infty}{\frac{1}{2}\rho V^2}\cot\alpha \qquad \text{at E} \qquad (2\text{-}57)$$

From eqs. (2-55) and (2-56) we obtain

$$\frac{d\theta}{dr} - \frac{\sqrt{M^2-1}}{M(1+\frac{\gamma-1}{2}M^2)}\frac{dM}{dr} + \frac{\sin\alpha\sin\theta}{r\sin(\theta+\alpha)} = 0 \qquad (2\text{-}58)$$

which is the condition of compatibility between M and θ along a family II characteristic.

Eqs. (2-54), (2-55) and (2-56) give the form of the control surface and the velocity distribution along it.

Construction of optimum contour - The first step in the construction procedure is to choose the contour in the region of the throat. Rao suggested using the contour of Fig. 2-3c. The transonic flow is then calculated (section 2.3) to give the flow conditions along a line AB where the flow is entirely supersonic. The characteristic "kernel" is then developed. Several family I characteristics are computed from various points on the initial expansion contour TB'. With experience, these characteristics can be chosen to bracket the characteristic of interest, BD.

Instead of choosing L, Rao chooses M_E, which defines L a posteriori. By choosing several values of M_E, optimum contours of several lengths are obtained.

Choosing M_E allows eq. (2-57) to be solved for θ_E. Note that for $p_\infty = 0$, eq. (2-57) reduces to

$$\sin 2\theta_E = \frac{2}{\gamma M_E^2} \cot \alpha_E \qquad (2\text{-}59)$$

The relationship for M and θ along the control surface is given by eqs. (2-55) and (2-56). These equations can be written as

$$M^* \frac{\cos(\theta-\alpha)}{\cos\alpha} = M_E^* \frac{\cos(\theta_E-\alpha_E)}{\cos\alpha_E} \qquad (2\text{-}60)$$

and

$$\frac{r}{r_E} M^2\left(1+\frac{\gamma-1}{2}M^2\right)^{\frac{-\gamma}{\gamma-1}} \sin^2\theta\tan\alpha = M_E^2\left(1+\frac{\gamma-1}{2}M_E^2\right)^{\frac{-\gamma}{\gamma-1}} \sin^2\theta_E\tan\alpha_E \qquad (2\text{-}61)$$

Equations (2-60) and (2-61) may be solved to yield M and θ for various values of $\frac{r}{r_E}$. These relations along the control surface can be computed even though we do not yet know the position of the control surface, DE.

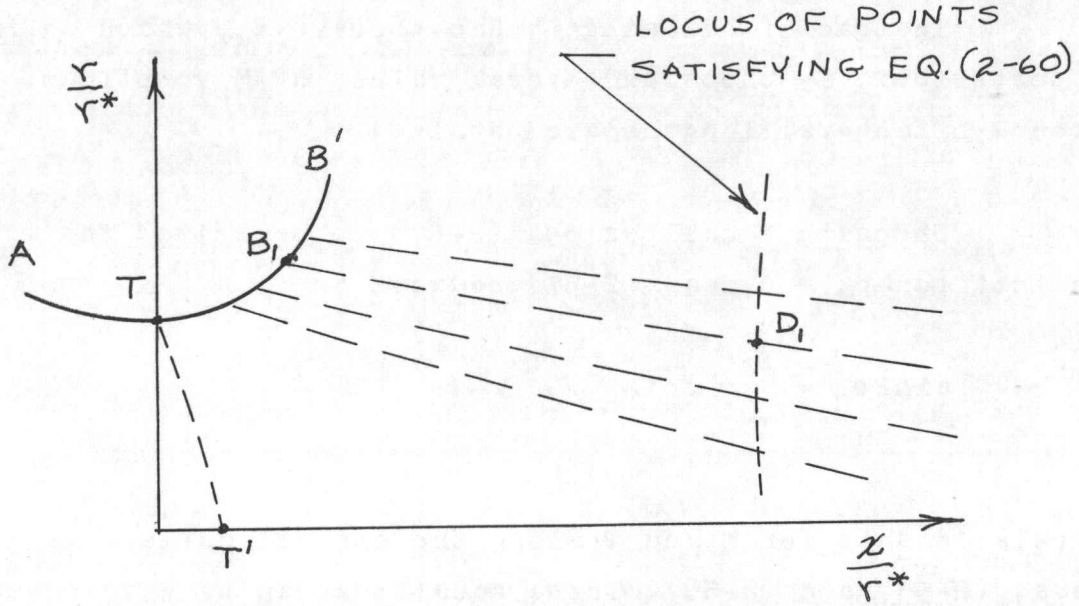

The next step is to locate point D, which lies on the dashed line in the sketch. A trial position of D_1 is chosen, and $\left.\frac{r}{r_E}\right|_1$ is determined from eq. (2-61). The criterion for the correct position of D_1 is that the mass flow crossing B_1D_1 be equal to the mass flow crossing D_1E.

$$2\pi r^*\rho^*V^* \int_{B_1}^{D_1} \frac{\rho V \sin\alpha}{\rho^* V^* \cos(\theta-\alpha)} \frac{r}{r^*} d\left(\frac{x}{r^*}\right) =$$

$$2\pi r^*\rho^*V^* \int_{1}^{D_1} \frac{\rho V \sin\alpha}{\rho^* V^* \sin(\theta+\alpha)} \frac{r}{r_E} d\left(\frac{r}{r_E}\right) \qquad (2\text{-}62)$$

Equation (2-62) is solved by trial and error, thus locating point D. We now have sufficient information to completely define the control surface, DE, which is a family II characteristic. The respective values of M and θ are known at D. From eq.(2-61) the value of r_E is obtained. The fact that DE is a characteristic allows calculation of x_E.

Now that BD and DE are defined, we may construct the nozzle contour in the same manner as for the ideal nozzle (section 2.4).

Typical nozzle configuration - Rao presented in Ref. 2-2 two examples of optimum nozzles for $p_\infty = 0$ and $\gamma = 1.23$. The wall contours of the two nozzles, having $M_E = 3.5$ and 2.6, respectively are shown in fig. 2-8. The performance characteristics of the nozzles are shown in the following table.

	NOZZLE A	NOZZLE B	NOZZLE A SHORTENED TO LENGTH OF B
L/r^*	8.19	2.94	2.94
A_e/A^*	19.36	4.973	6.84
C_{Fv}	1.7676	1.5829	1.5688
% of one dimensional thrust for same area ratio	98.58	96.93	93.5
% of thrust of conical nozzle having same L and A_e/A^*	102.3	100.5	102.1

Approximation of optimum nozzle contour - Rao (Ref. 2-23) proposed a simple graphical approximation for the optimum nozzle contour when r_E/r^* and L/r^* are specified. The throat geometry is that of fig. 2-4(c), except the radius downstream of the throat is slightly smaller. The optimum nozzle contour will have unique values of θ_E and θ_M (maximum wall angle, at B) if length and area ratio are specified. The parametric values of θ_M and θ_E are shown in fig. 2-9. With θ_M and θ_E known, it is possible to approximate the nozzle contour with a parabola. The parabolic contour is constructed by a simple graphical procedure, illustrated in fig. 2-10.

For $\frac{A_e}{A^*} = 25$ and $\frac{L}{r^*} = 12$, the approximate contour agrees with the exact contour within 3% of the radial coordinate. The accuracy is adequate for preliminary engineering analysis of weight, heat transfer, etc.

The wall angles of fig. 2-9 were calculated with $\gamma = 1.23$. When area ratio and length are specified, the contour is insensitive to γ and fig. 2-9 may be used for other values of γ.

2.6.2 Truncated ideal nozzles

The rigorous optimization of Rao (and Guderley and Hantsch) has been applied only to the case of prescribed nozzle length. The variational problem has not yet been solved for the more complex case of prescribed nozzle surface (essentially weight). Also, the effect of wall friction has not been included in the variational analysis.

To approach the general optimization problem, several investigators have suggested that truncated ideal nozzles be examined. Ahlberg, et al, (ref. 2-8) have made extensive investigations of truncated ideal nozzles. They developed a series of ideal, sharp cornered nozzles, with various area ratios, based on a prescribed throat flow. The conditions of optimum length and surface area were investigated numerically. Friction losses were calculated by use of a simple skin friction relation.

A family of ideal nozzle contours are shown in fig. 2-11. The nomenclature is that of ref. 2-8: A_D corresponds to $\left.\frac{A_e}{A^*}\right|_{ideal}$, and $\frac{A_s}{A_T}$ to the ratio of nozzle surface area to throat area. There are four variables shown on fig. 2-11: vacuum thrust coefficient, surface area, length and exit diameter. Any two of these completely specify the contour and the other two variables.

minimum
Maximum length nozzles - For a given value of C_{F_v}, the optimum length nozzle is obtained when the line of C_{F_v} is tangent to a vertical line.

Minimum surface nozzles - Minimum surface nozzles are obtained when the line of C_{F_v} is tangent to a line of constant surface area. The difference between optimum length and optimum surface nozzles is relatively small.

Non-vacuum operation - When $p_\infty \neq 0$, the C_F curves of fig. 2-11 are not valid. New lines of constant C_F may be plotted by using eq. (1-32):

$$C_F = C_{Fv} - \frac{A_e}{A^*} \frac{p_\infty}{p_c} \qquad (1\text{-}32)$$

Because of the shift of the C_F curves with increasing p_∞, segments of lower area ratio nozzles result for the optimum nozzles

Comparisons with other nozzles - For a given value of C_{F_v}, the optimum length truncated ideal nozzle is slightly shorter than the corresponding Rao nozzle. This may be caused partly by different numerical techniques, but more likely because Ahlberg, et al., used a sharp corner downstream of the throat. A minimum surface truncated ideal nozzle is nearly identical to a minimum length Rao nozzle.

For the same value of C_{F_v}, an optimum truncated ideal nozzle may have 30-40% less length and surface area than a 15° conical nozzle. This comparison is based on the same throat flow and friction coefficients for both types of nozzles.

Wall friction effects - The effect of friction in nozzles is to cause the optimum length and surface to be less than for frictionless flow. Using an area ratio 40 ideal nozzle as an example, Ahlberg, et al., show that the nozzle should be about 13% shorter than ideal to obtain maximum thrust with friction.

2.6.3 Experiments on optimum nozzles

Bloomer, et al., (Ref. 2-24) have investigated three different contoured nozzles with the same O_2-JP4 rocket chamber as was used for their investigation of conical nozzles (Ref. 2-20, see also section 2.5.). The nozzles were designed by the method of Rao, with the following characteristics:

Nozzle	A_e/A^*	L/r^*	Length
			Length of 15° conical with same area ratio
1	16	9.03	0.80
2	25	9.35	0.60
3	30	10.22	0.60

The experimental vacuum thrust coefficients of the three contoured nozzles are compared with conical nozzle performance in fig. 2-12. For a given length (fig. 2-12a), nozzles 2 and 3 show a 1-2% improvement over the best conical nozzles. Nozzle 1 shows no improvement over the 25° conical nozzle. On the

basis of the same C_{F_v}, the contoured nozzles are much shorter than the 15° conical nozzle.

For a fixed nozzle surface area, the contoured nozzles show no improvement over the 20° conical nozzle (fig. 2-12b).

2.7 EFFECT OF VARIABLE THERMODYNAMIC PROPERTIES

Throughout this chapter we have used the assumption that the gas composition is invariant. In general, however, chemical reactions occur in the nozzle, resulting in variations of the thermodynamic properties.

For the case of equilibrium chemistry in the nozzle, the variations of the gas properties can be incorporated into the method of characteristics in a relatively simple way. Guentert and Neumann (Ref. 2-25) have developed a procedure for incorporating thermochemical data into the method of characteristics. Ahlberg, et al., (Ref. 2-8) and Migdal and Landis (Ref. 2-14) have treated the case of equilibrium chemistry in the nozzle by defining an effective isentropic coefficient, γ:

$$\gamma = \left.\frac{\partial(\ell n p)}{\partial(\ell n \rho)}\right|_s$$

The variation of γ with the flow variables, p or M, is obtained from one dimensional thermochemical calculations. The variation of γ with pressure is shown in fig. 2-13 for typical rocket propellants.

Comparison with constant γ - For a given nozzle contour, Ahlberg, et al., have shown that the ratio of $C_{F_v}/C_{F_{vid}}$ is insensitive to variations of γ. Some typical results are shown in the following table. The nozzle was a truncated ideal nozzle, designed for minimum surface with $\gamma = 1.2$ and $\frac{A_e}{A^*} = 25$.

GAS	$C_{Fv}/C_{Fv\ id}$	C_F (no friction)
$\gamma = 1.1$	.9875	1.922
solid(fig.2-13)	.9874	1.914
H_2-O_2(fig.2-13)	.9852	1.829
$\gamma = 1.2$	.9849	1.815(design contour)
$\gamma = 1.4$	.9790	1.666

To calculate $\frac{C_{F_v}}{C_{F_{vid}}}$ in a nozzle of specified geometry, $\gamma = 1.1$ may be used for the solid propellant, and $\gamma = 1.2$ for the H_2-O_2 propellant. Migdal and Landis obtained similar results for conical nozzles.

Note that to accurately calculate C_{F_v}, the actual gas properties should be used. Also, the variation of gas properties has some influence on nozzle optimization. If the nozzle length and exit diameter are specified, however, the nozzle shape is only slightly changed by a relatively large variation of γ (Refs. 2-8 and 2-23).

REFERENCES

2-1 BARRERE, et al.; Rocket propulsion.
Elsevier Publishing Co., Amsterdam, London, New York and Princeton, 1960.

2-2 RAO: Exhaust nozzle contour for maximum thrust.
Jet Propulsion, vol. 28, no 6, June 1958, pp.377-382.

2-3 OSWATITSCH & ROTHSTEIN: Flow pattern in a converging-diverging nozzle.
NACA TN 1215, March 1949.

2-4 SAUER: General characteristics of flow through nozzles at near critical speeds.
NACA TM 1147, June 1947.

2-5 SHAPIRO: The dynamics and thermodynamics of compressible fluid flow, 2 volumes.
Ronald Press, New York, 1953.

2-6 HALL: Transonic flow in two dimensional and axially symmetrix nozzles.
ARC 23 347, December 1961.

2-7 EMMONS: The numerical solution of compressible fluid flow problems.
NACA TN 932, 1944.

2-8 AHLBERG, et al.: Truncated perfect nozzles in optimum nozzle design,
ARS Jnl, vol. 31, no 5, May 1961, pp. 614-620.

2-9 VALENTINE: An approximate method for design or analysis of two dimensional subsonic flow passages.
NACA TN 4241, April 1958.

2-10 RAO: Analysis of a new concept rocket nozzle.
Progress in Astronautics and Rocketry, vol. 2,
Academic Press, New York, 1960, p. 669.

2-11 LORD: A theoretical study of annular supersonic nozzles.
ARC R & M 3227, October 1959.

2-12 MOORE & HALL: Transonic flow in the throat region of an annular nozzle with arbitrary smooth profile.
ARC 26 543, January 1965.

2-13 FERRI: Elements of aerodynamics of supersonic flows.
MacMillan Co., New York, 1949.

2-14 MIGDAL & LANDIS: Characteristics of conical supersonic nozzles.
ARS Jnl, vol. 32, no 12, December 1962, pp.1898-1901.

2-15 DARWELL & BADHAM: Shock formation in conical nozzles.
AIAA Jnl, vol. 1, np 8, August 1963, pp. 1932-1934.

2-16 MIGDAL & KOSSON: Shock predictions in conical nozzles.
AIAA Jnl, vol. 3, no 8, August 1965, pp. 1554-1556.

2-17 FRASER, et al.: Efficiency of supersonic nozzles for rockets and some unusual designs.
Proc. Inst. of Mech. Eng., vol. 171, no 16, 1957.

2-18 ROWE: The effect of divergence angle on the thrust of a supersonic nozzle.
Imperial College Report JRL no 36, September 1957.

2-19 CAMPBELL & FARLEY: Performance of several convergent - divergent rocket-type exhaust nozzles.
NASA TN D - 467, September 1960.

2-20 BLOOMER, et al.: Experimental study of effects of geometric variables on performance of conical rocket engine exhaust nozzles.
NASA TN D - 846, June 1961.

2-21 DILLAWAY: A philosophy for improved rocket nozzle design.
Jet Propulsion, vol. 27, no 10, October 1957,
pp. 1088-1093.

2-22 GUDERLEY & HANTSCH: Beste Formen für Achsensymmetrische Überschallschubdüsen.
Zeitsch. für Flugwissensch., vol. 3, September 1955.

2-23 RAO: Approximation of optimum thrust nozzle contour.
ARS Jnl, vol. 30, no 6, June 1960, P.561.

2-24 BLOOMER, et al.: Experimental study of effects of geometric variables on performance of contoured rocket engine exhaust nozzles.
NASA TN D - 1181, January 1962.

2-25 GUENTERT & NEUMANN: Design of axisymmetric exhaust nozzles by the method of characteristics incorporating a variable isentropic exponent.
NASA TR R - 33, 1959.

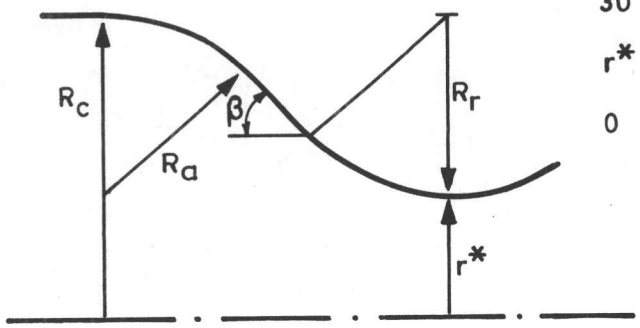

$30^\circ < \beta < 45^\circ$

$r^* < R_r < 2r^*$

$0 < R_a < R_c$

a) Conical section (ref. 2-1)

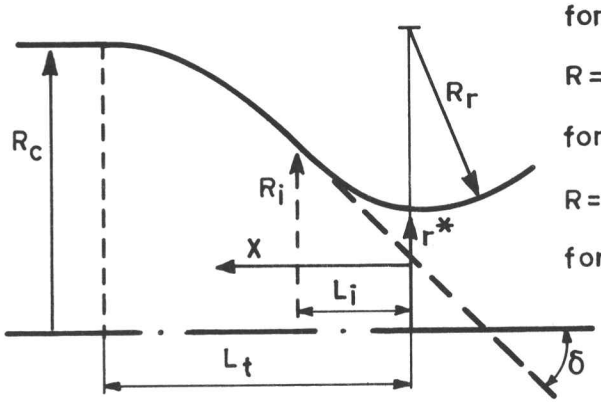

for $0 < X < L_i$:

$$R = R_i - (R_i - r^*)\cos\frac{\pi}{2}\,\frac{X}{L_i}$$

for $L_i < X < L_t$:

$$R = R_i + (R_c - R_i)\sin\frac{\pi}{2}\,\frac{X - L_i}{L_t - L_i}$$

for $\frac{L_i}{L_t} = 0.4$

$$R_i = \frac{r^* + 0.666\,R_c}{1.666}$$

for $L_t = R_c$, $\delta = 45^\circ$

b) Sinusoidal section (ref. 2-1)

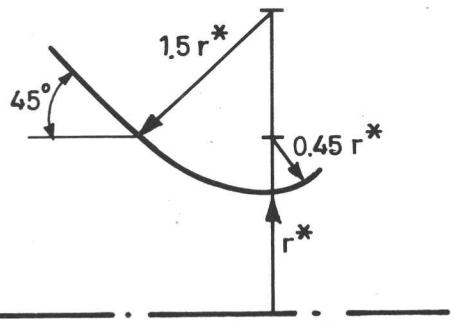

c) Rao's throat geometry (ref. 2-2)

Fig. 2-1 CONVERGENT NOZZLE CONTOURS

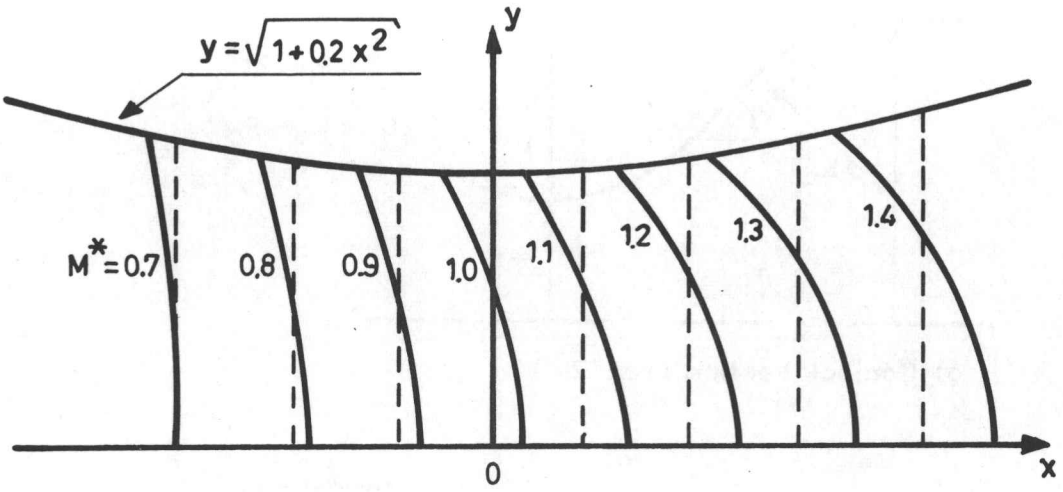

a) Two - dimensional

– – – – – – – one-dimensional

——————— series expansion

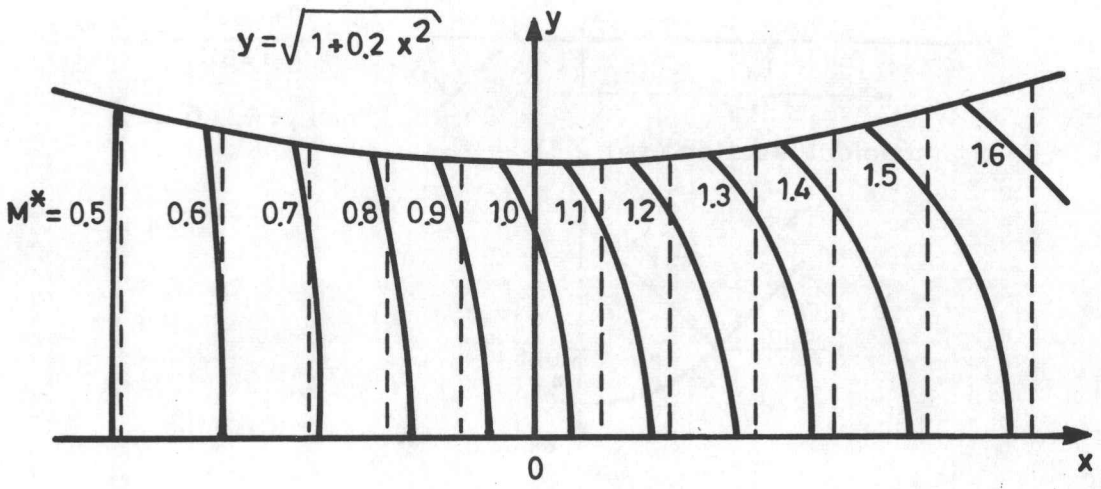

b) Axisymmetric

Fig. 2-2 TRANSONIC FLOW IN NOZZLES (ref. 2-3)

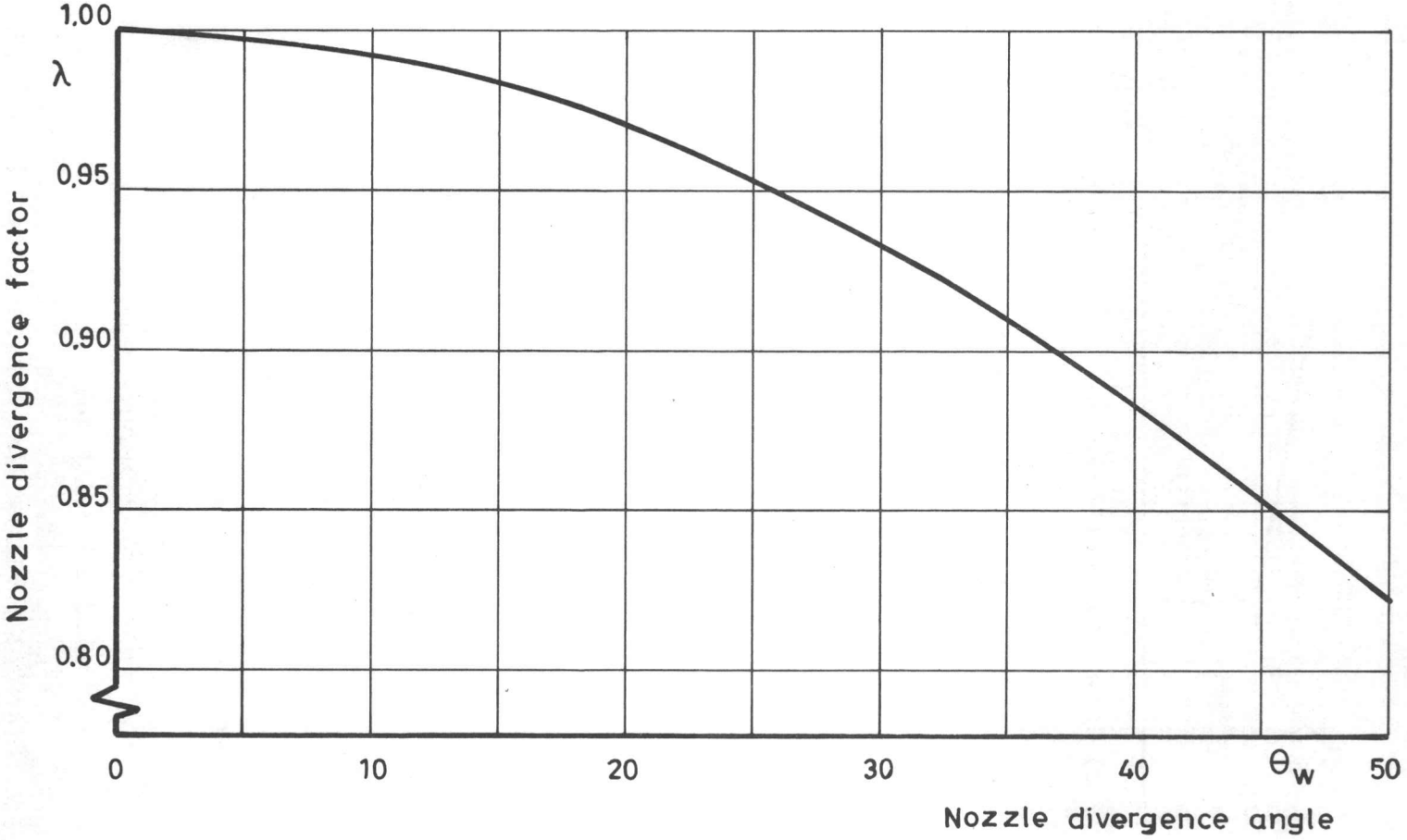

Fig. 2-3 DIVERGENCE FACTOR FOR CONICAL NOZZLES

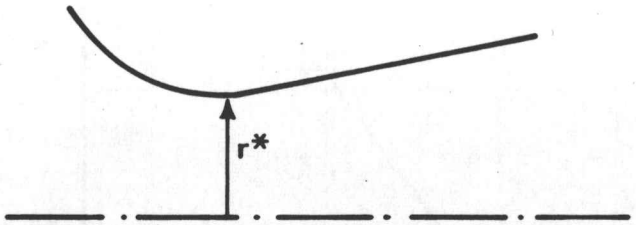

a) Cone attached directly

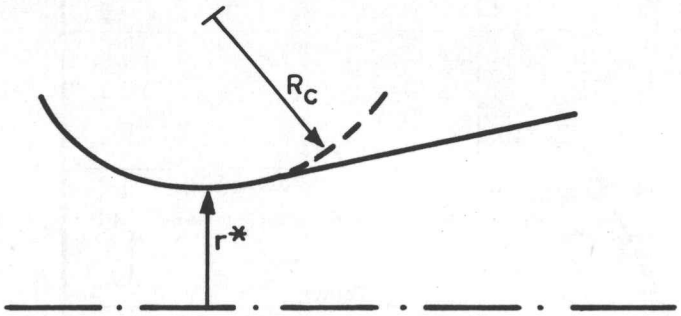

b) Positive curvature transition

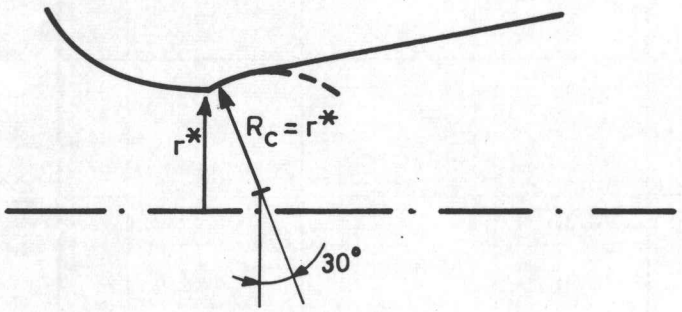

c) Negative curvature transition

Fig. 2-4 TRANSITION CONTOURS FOR CONICAL NOZZLES (ref. 2-14)

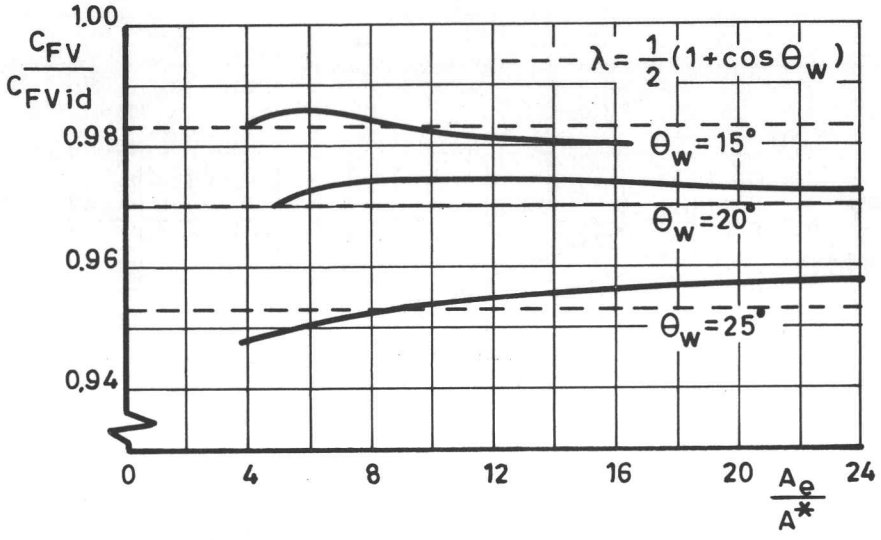

a) Transition geometry of fig. (2 - 4b) with $\frac{R_c}{r^*} = 2$

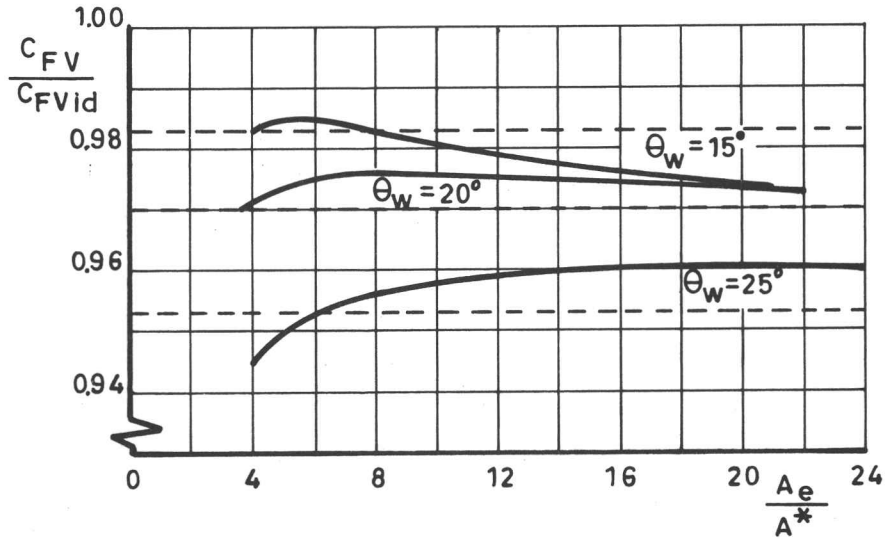

b) Transition geometry of fig. (2 - 4c)

Fig. 2 - 5 THRUST EFFICIENCY OF CONICAL NOZZLES ($\gamma = 1.2$) (ref. 2-14)

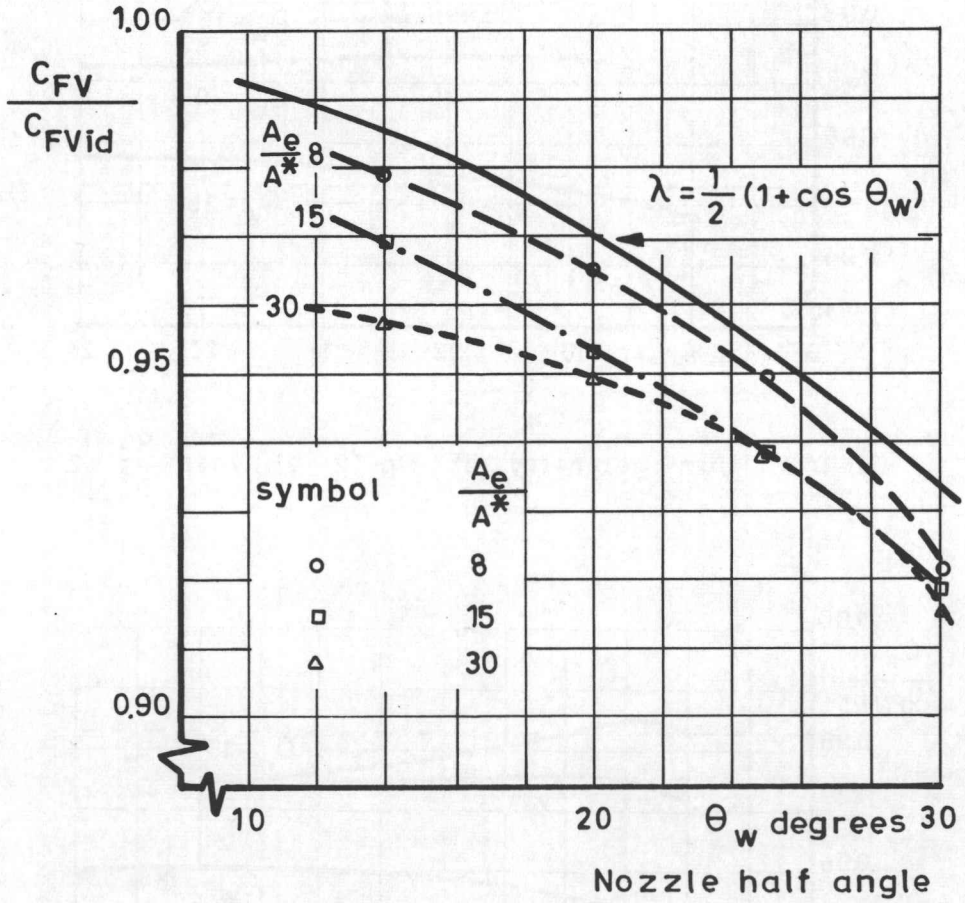

Fig. 2-6 EXPERIMENTAL PERFORMANCE OF CONICAL NOZZLES (ref. 2-20)

Bloomer

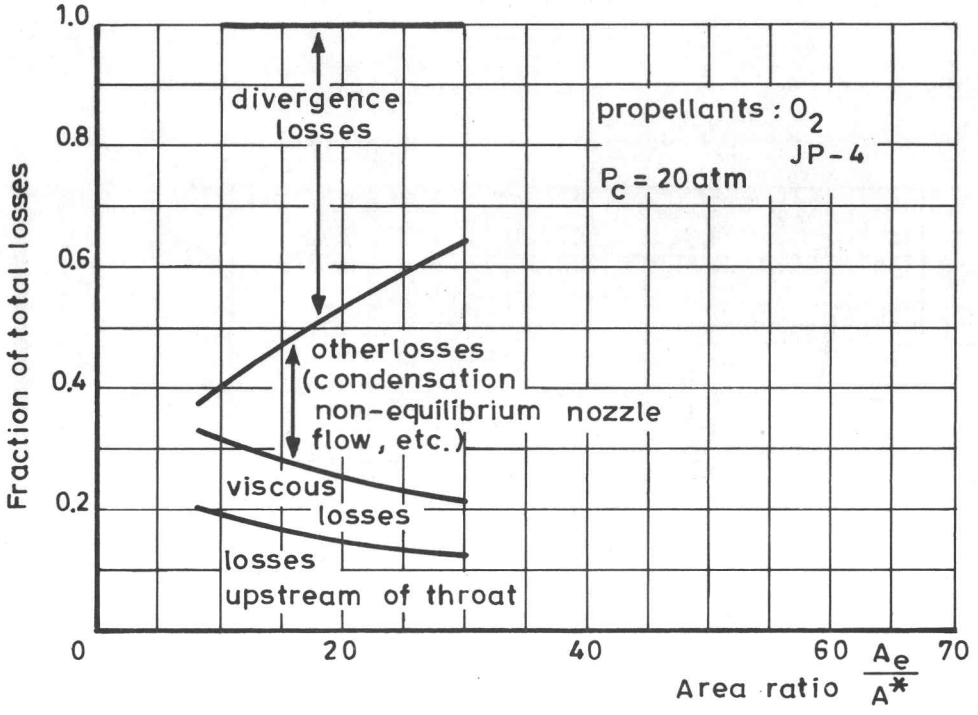

a) 15° Half angle nozzles

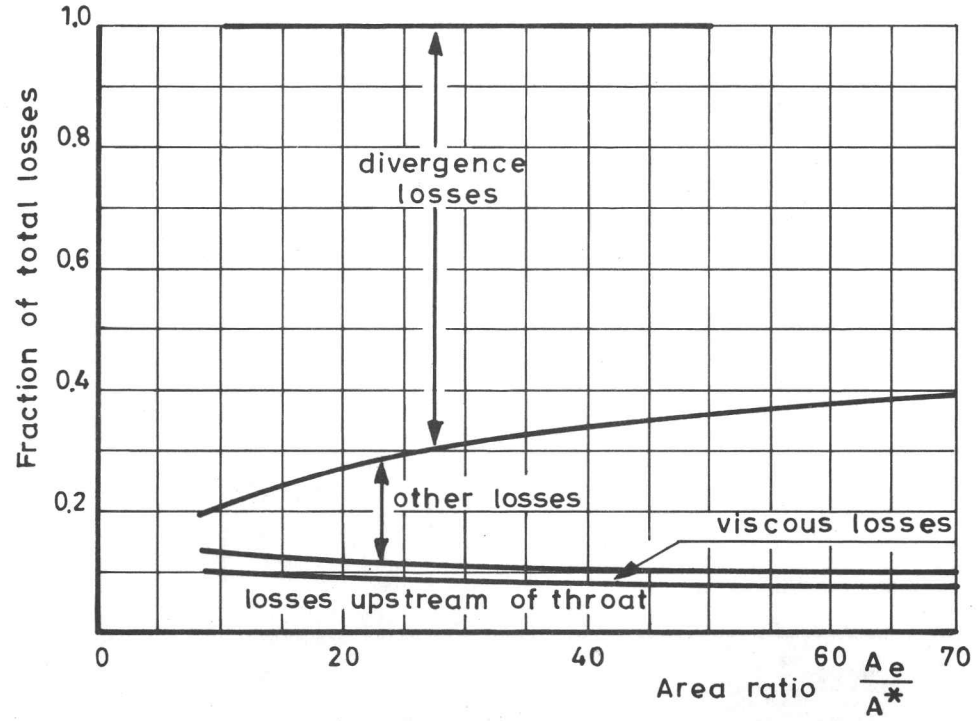

b) 25° Half angle nozzles

Fig. 2-7 DISTRIBUTION OF LOSSES IN CONICAL NOZZLES (ref. 2-20)

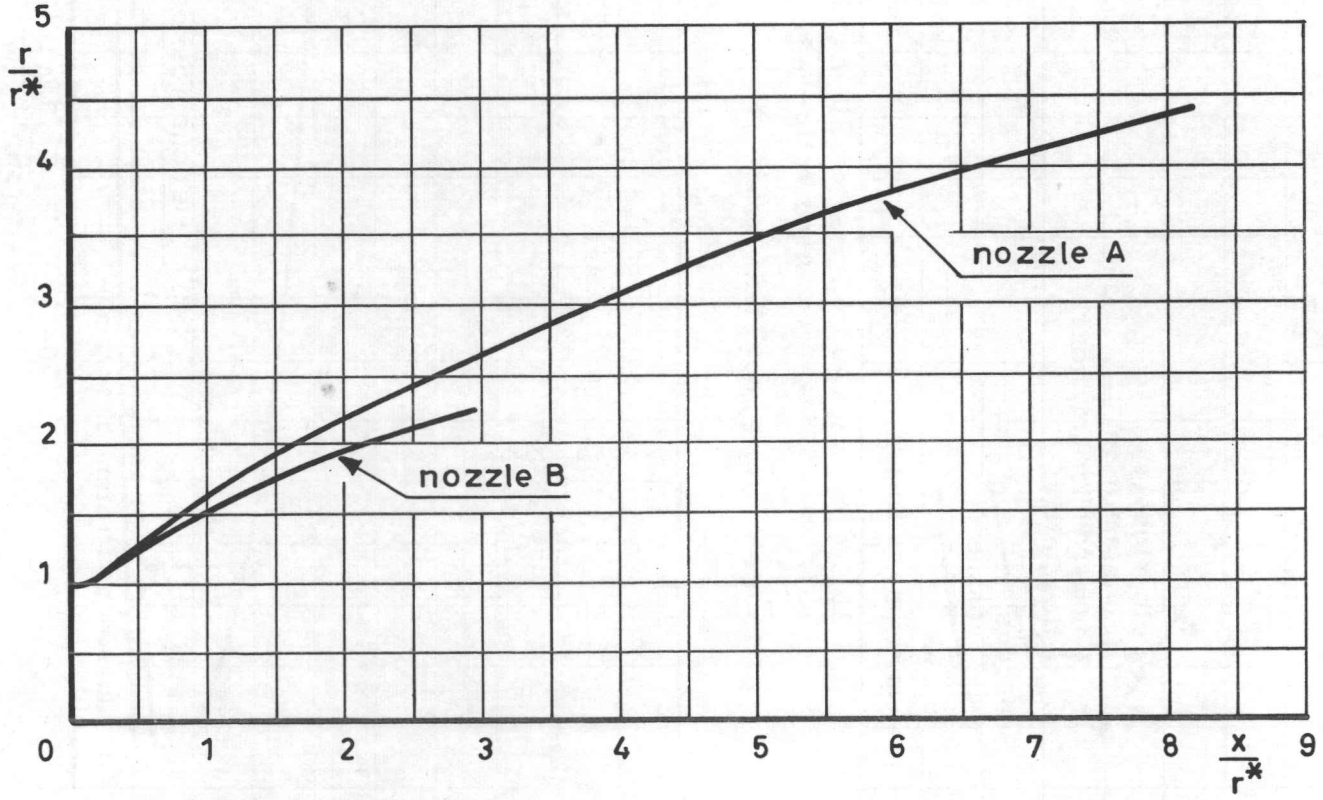

Fig. 2-8 TYPICAL OPTIMUM NOZZLE CONTOURS (ref. 2-2)

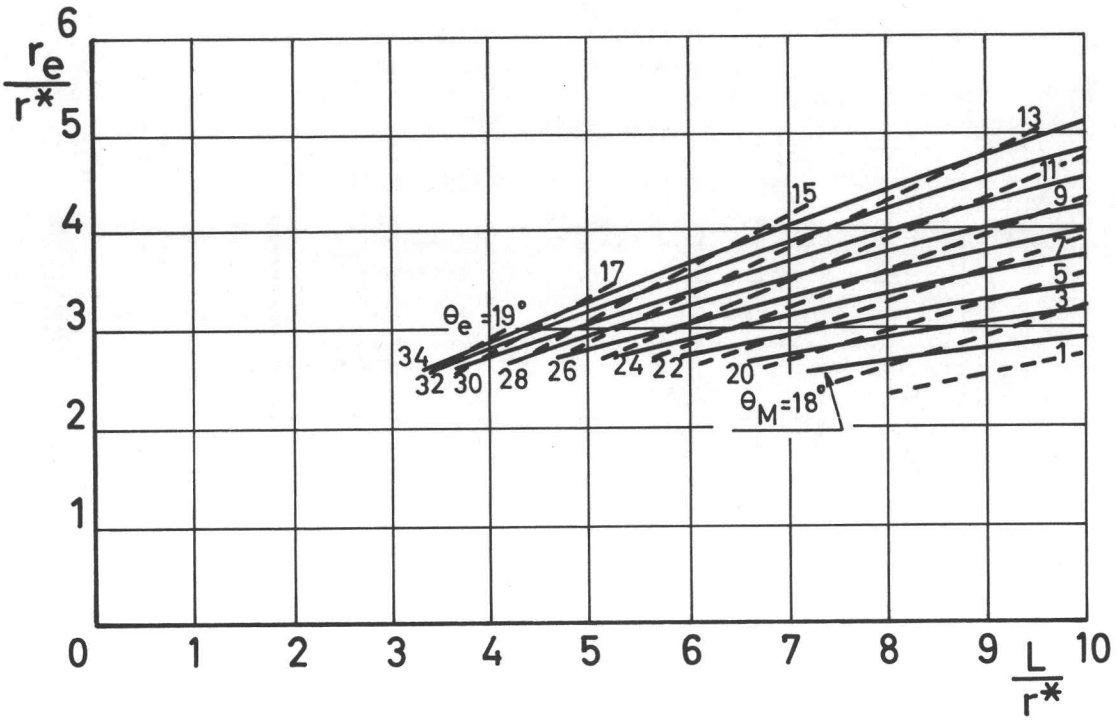

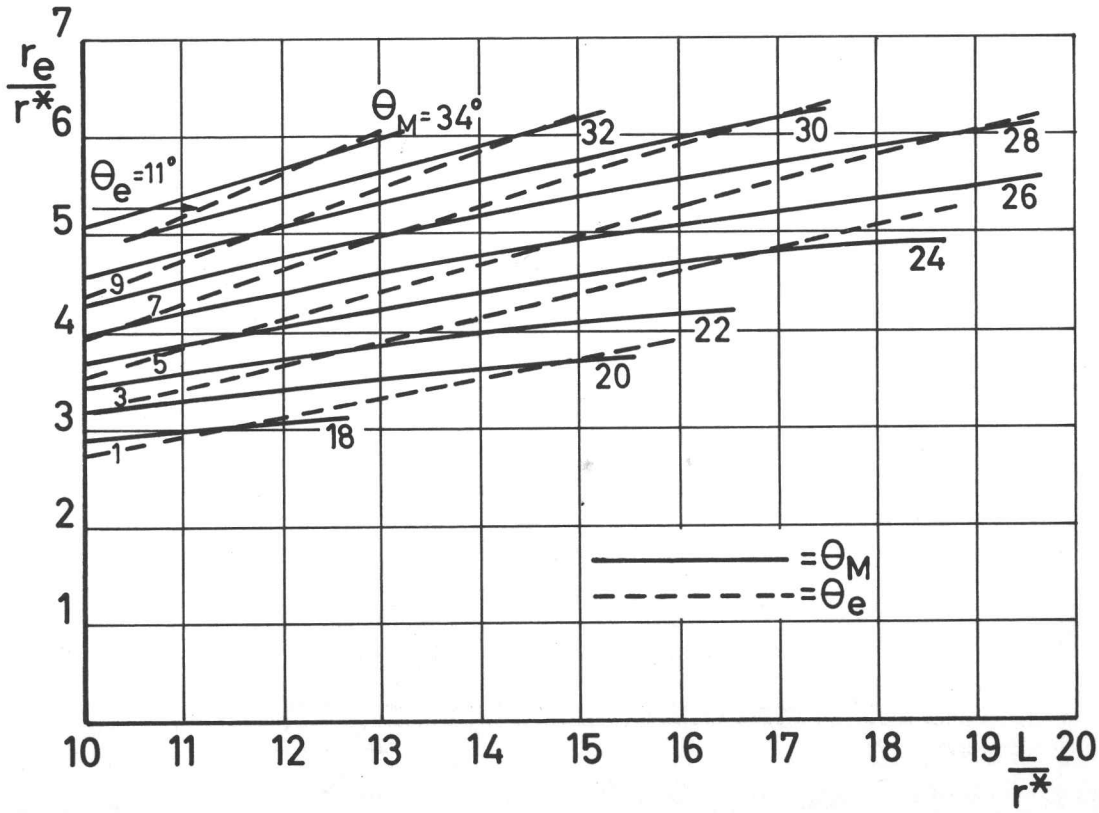

Fig. 2-9 WALL ANGLES AT INFLECTION POINT AND EXIT OF OPTIMUM NOZZLES (ref. 2-23)

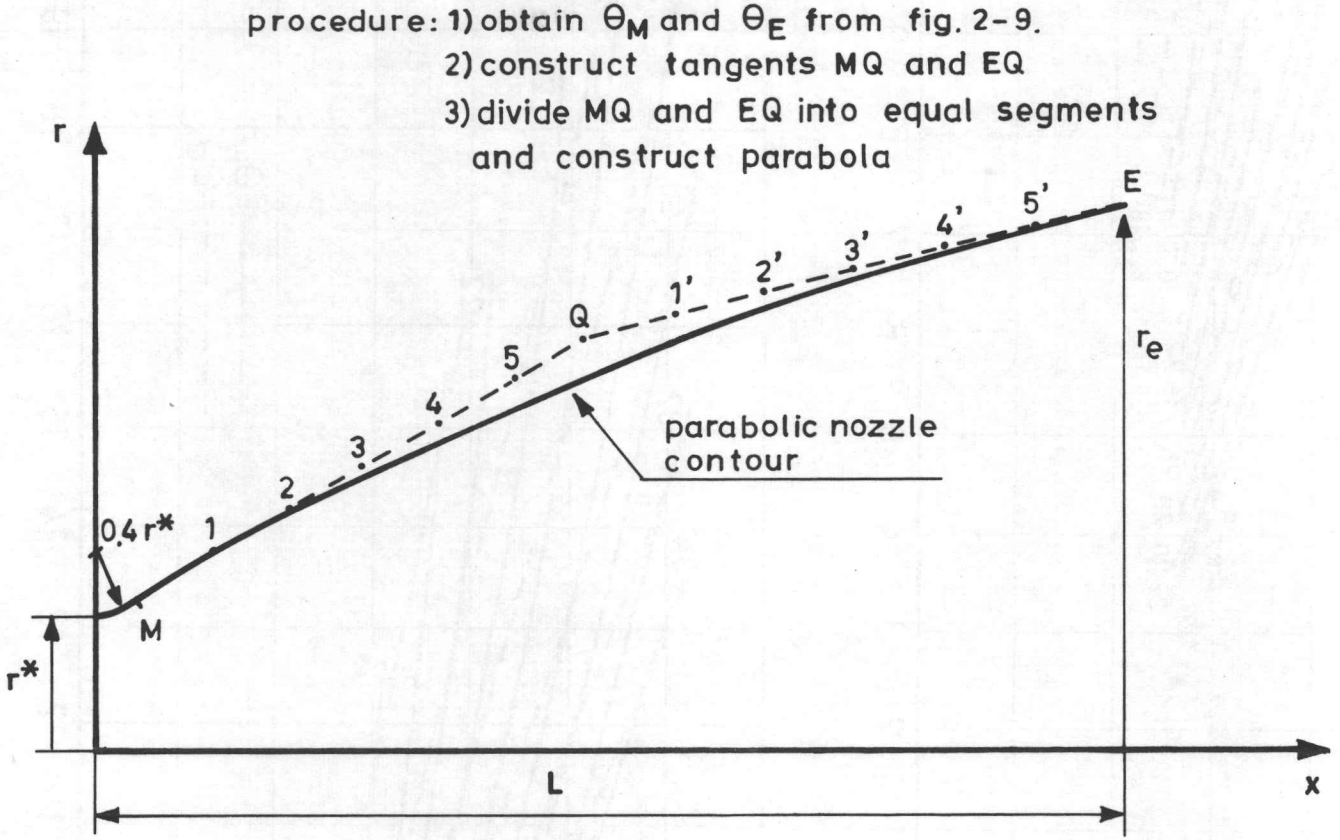

Fig. 2-10 APPROXIMATE CONSTRUCTION OF OPTIMUM NOZZLE CONTOUR (ref. 2-23)

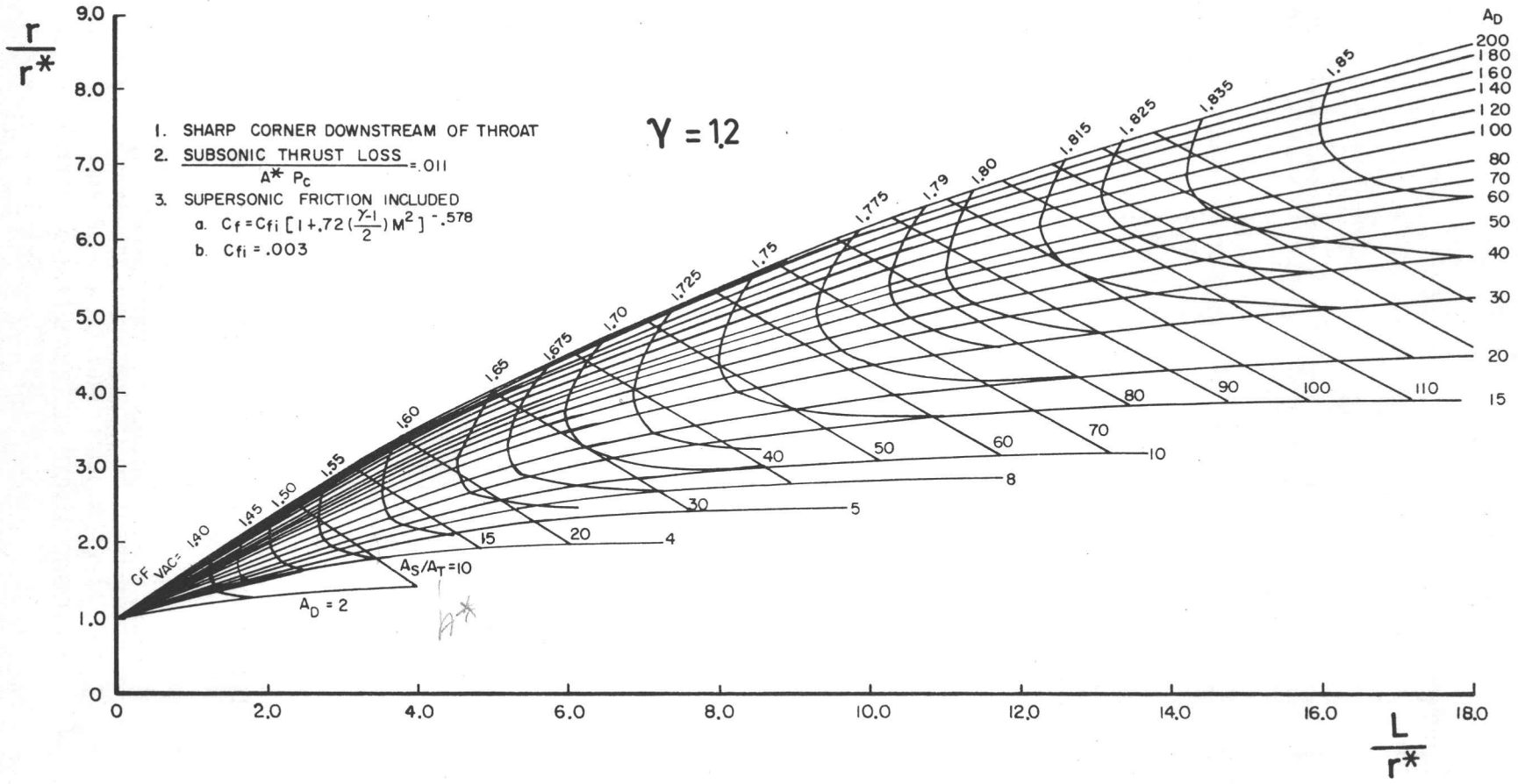

Fig. 2-11 TRUNCATED PERFECT NOZZLE SHAPES (ref. 2 - 8)

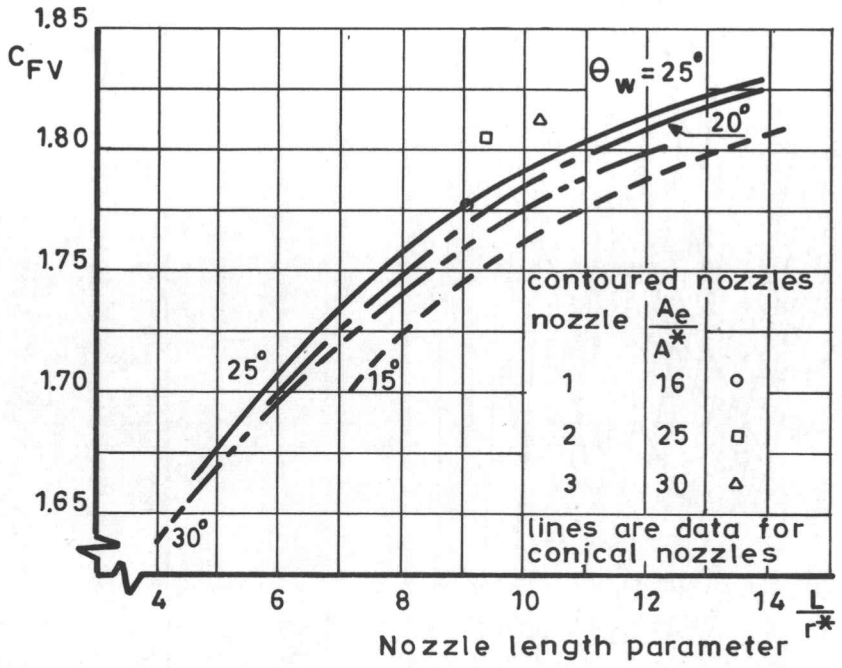

a) Comparison based on nozzle length

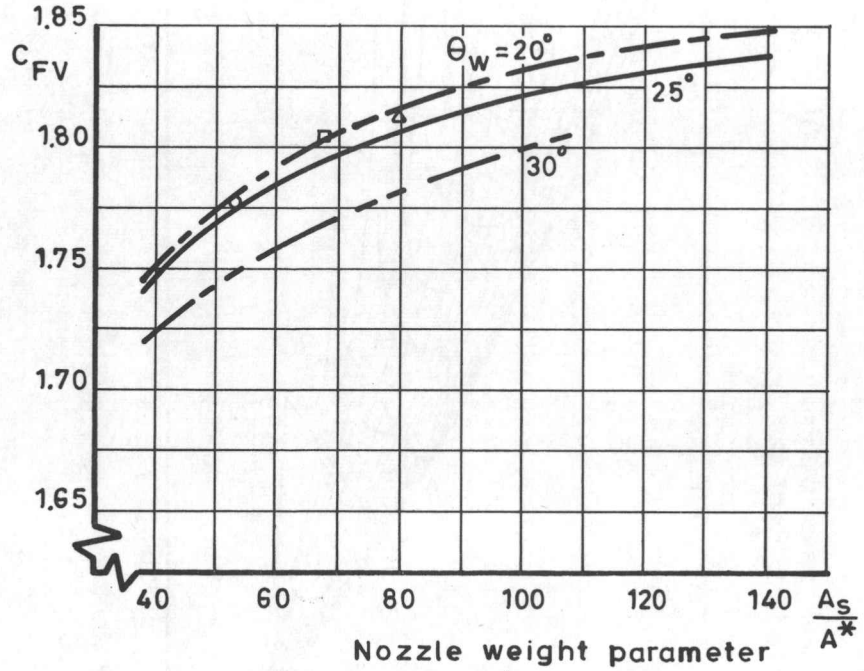

b) Comparison based on nozzle weight

Fig. 2 - 12 EXPERIMENTAL PERFORMANCE OF CONTOURED NOZZLES (ref. 2 - 24)

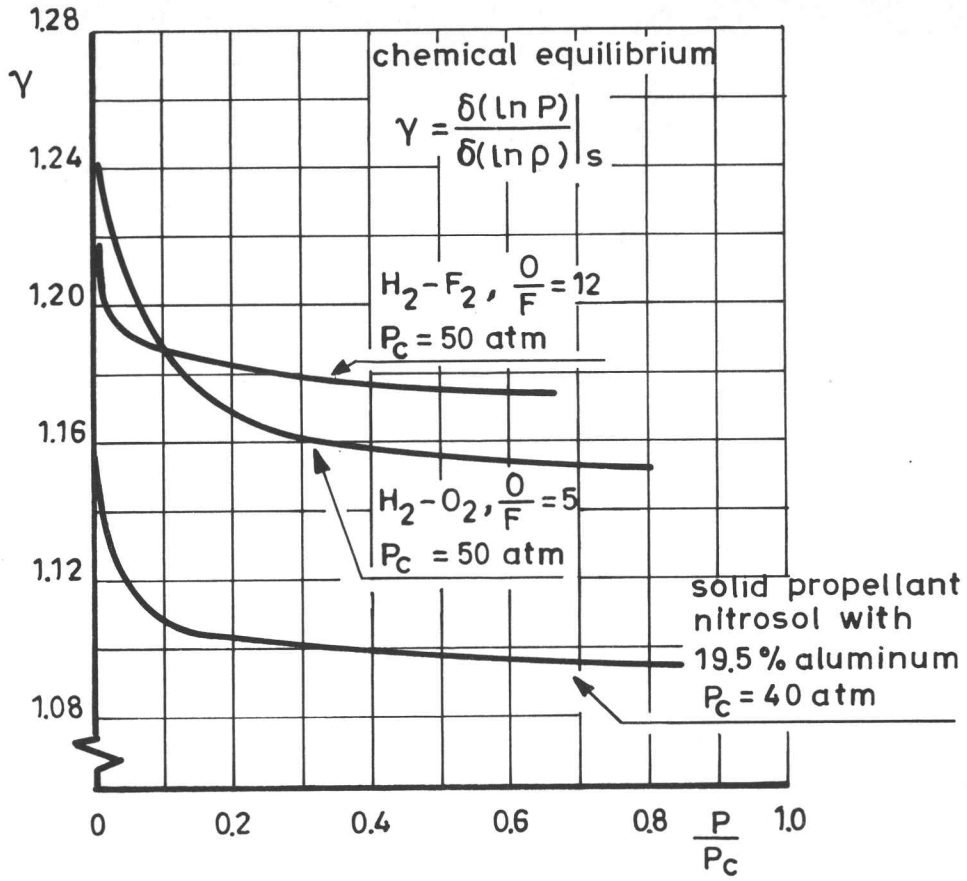

Fig. 2-13 VARIATION OF γ FOR TYPICAL PROPELLANTS (ref. 2-14)

8100
71
46 5800
46 6000
16 9800

CHAPTER 3

TWO PHASE FLOW IN ROCKET NOZZLES

3.1 INTRODUCTION

Metal additives (usually aluminum) are used in solid propellants for two purposes: (1) to suppress high frequency combustion instability, and (2) to increase the energy release of the propellant. The mechanism of suppression of combustion instability is not well understood, but empirical data have established the effectiveness of metal additives.

With respect to the higher energy release of metallized propellants, the theoretical performance improvement is never achieved in practice. The combustion temperature of a solid propellant is increased by adding metal, but condensable metallic oxides are formed in the exhaust products. These condensable oxides, which make up 30-40% by weight of the exhaust products, cause the exhaust nozzle performance to be substantially below ideal. The main reason for the decreased performance is that the condensed liquid (or solid) particleshave finite mass, and always lag the gas velocity to a certain extent. Energy nonequilibrium between the phases has a lesser effect on the nozzle performance.

In addition to causing a loss in thrust, the particles may impinge on the wall and alter the heat transfer rates. Serious erosion of the wall may also result.

Although the primary interest is in metallized solid propellants, certain liquid propellant combinations (containing pentaborane, for example) also produce exhaust products containing sizable amounts of condensable metallic oxides.

During recent years many investigators have been working on the prediction of two phase nozzle flows. Hoglund (Ref. 3-1) presented an excellent review of the state of the art in this field up to 1962. Kliegel (Ref. 3-2) and Hoffman (Ref. 3-3) have also discussed the various investigations in this field.

3.2 ONE DIMENSIONAL GAS-PARTICLE FLOWS

3.2.1 Limiting equilibrium and nonequilibrium cases

Altman and Carter (Ref. 3-4) examined nozzle performance for various arbitrary ratios of particle velocity to gas velocity at the nozzle exit. They ignored the coupling between the velocity and thermal lags of the particles and treated the gas expansion as frictionless. If the ratios $\left.\frac{u_p}{u_g}\right|_e$ and $\left.\frac{T_p}{T_g}\right|_e$ are known, the following equations may be used to calculate the specific impulse:

$$\frac{1}{2}\left[\frac{w_g}{w_g+w_p}\,u_{ge}^2 + \frac{w_p}{w_g+w_p}\,u_{pe}^2\right] = c_{pg}(T_c-T_{ge})+c_{pp}(T_c-T_{pe}) \tag{3-1}$$

and

$$I_{sp} = \frac{\left[u_{ge}+\frac{w_p}{w_g}\,u_{pe}\right]}{g_o\left[1+\frac{w_p}{w_g}\right]} \tag{3-2}$$

where the subscripts g, p, and e indicate gas, particle and exit plane, respectively.

To illustrate the nonequilibrium effects, Altman and Carter used the following typical rocket parameters

$$T_c = 3\,000°K$$

$$\frac{p_c}{p_e} = 20.4$$

$$\frac{w_p}{w_g + w_p} = 0.20$$

$$\mathcal{M}_g = 20$$

$$c_{pg} = 0.6 \text{ cal/°K}$$

$$c_{pp} = 0.1 \text{ cal/°K}$$

The following results were obtained, for the limiting cases of complete thermal equilibrium and complete thermal isolation.

$\left.\frac{u_p}{u_g}\right\|_e$	I_{sp}, sec., for $T_{pe}=T_{ge}$	I_{sp}, sec., for $T_{pe}=T_c$
0	206	203
0.25	217	214
0.50	224	221
1.00	230	227
no solid	254	254

We see that thermal nonequilibrium between the phases is of much less importance than kinetic nonequilibrium. The table also illustrates that, even under complete equilibrium, the performance is lower than for a propellant without metal additives.

3.2.2 Effect of particle size on performance

Gilbert, Davis and Altman (Ref. 3-5), were the first to relate performance losses to particle size. Their analysis was uncoupled, in that the velocity and thermal lags were treated independently. They also ignored the effect of the particles on the gas expansion.

For Re < 2, the particles are in the Stokes' regime where $C_D = \frac{24}{Re}$. The equation of particle motion is

$$m_p \frac{d^2x}{dy^2} = 6\pi\mu r_p(u_g - u_p) \qquad (3\text{-}3)$$

where m_p and r_p are the particle mass and particle radius. If $u_g(x)$ is linear, eq. (3-3) is integrable. A general flow can be approximated by a series of straight line segments for $u_g(x)$, and eq. (3-3) can be integrated in a stepwise manner. With $u_g(x) = u_{go} + ax$, eq. (3-1) becomes

$$m_p \frac{d^2x}{dt^2} = 6\pi\mu r_p(u_g(o) + ax - \frac{dx}{dt}) \qquad (3\text{-}3a)$$

The boundary condition is $\frac{dx}{dt} = u_{po}$ at $x = 0$, $t = 0$.

The particle motion is described by

$$\xi = e^{-\tau}\left(\cosh\tau\sqrt{1+2\lambda} + \frac{\phi\lambda}{\sqrt{1+2\lambda}}\sinh\tau\sqrt{1+2\lambda}\right) - 1$$

where $\xi = \frac{ax}{u_{go}}$, dimensionless distance

$\tau = \frac{\alpha t}{2}$, dimensionless time

$\alpha = \frac{6\pi\mu r_p}{m_p} = \frac{9\mu}{2\rho_s r_p^2}$, reciprocal time constant, where ρ_s is the density of the particle material

$\lambda = \frac{2a}{\alpha}$

$\phi = \frac{u_{po}}{u_{go}}$

The relative velocity is given by

$$\frac{u_g - u_p}{u_g} = \frac{\phi(1+\lambda) - 1 + (1-\phi)\sqrt{1+2\lambda}\coth\tau\sqrt{1+2\lambda}}{1+\lambda\phi+\sqrt{1+2\lambda}\coth\tau\sqrt{1+2\lambda}} \qquad (3\text{-}4)$$

<u>Extension to non-Stokes flow</u> - For the general case

$$m_p\frac{d^2x}{dt^2} = \frac{\pi}{2}C_D\rho_g r_p^2(u_g - u_p)^2 \qquad (3\text{-}5)$$

Eq.(3-5) may be made linear over a small range of Re by defining a correction factor, f_p,

$$f_p = \frac{28Re^{-.85} + 0.48}{24Re^{-1}}$$

so that eq.(3-5) becomes

$$m_p \frac{d^2x}{dt^2} = 6\pi\mu r_p (u_p - u_g) f_p \qquad (3\text{-}6)$$

The factor, f_p, which alters α in eq. (3-4), is given in the following table:

Re	f_p
1	1.19
5	1.58
10	1.84
100	4.33
1000	23.7
2000	43.3

$f_p = \frac{C_D Re}{24} = \frac{C_D}{C_{D_{Stokes}}}$

Results for a typical rocket - Gilbert, Altman and Davis calculated the velocity lag, $\frac{u_{ge} - u_{pe}}{u_{ge}}$, at the exit plane for a typical 1300 lb thrust rocket. The results are shown in fig. 3-1. The velocity distribution was approximated by a single chord, and also by three straight line segments.

3.2.3 Generalized equations for one dimensional gas-particle flows

Kliegel (Ref. 3-6) was the first of several investigators to treat the coupled nozzle flow problem, with simultaneous thermal and velocity lags. The following assumptions were used in Kliegel's formulation of the problem:

- 1. No mass or energy losses from the system,
- 2. No mass exchange between the phases,
- 3. The particles occupy negligible volume,
- 4. The thermal (Brownian) motion of the particles is negligible,
- 5. The particles do not interact,
- 6. The gas is inviscid except for interactions with the particles,
- 7. The gas phase is a perfect gas of constant composition,
- 8. The particles have a uniform internal temperature,
- 9. Energy exchange between phases occurs only by convection,
-10. The gas and particles have constant specific heats,
-11. The particles are spherical and of uniform size.

As an alternative to the last assumption, several investigators have approximated the particle size distribution with groups of different size spheres. It has been established that the foregoing assumptions are reasonable for a typical rocket engine.

Basic equations

Gas phase continuity:

$$\rho_g u_g A = w_g \tag{3-7}$$

Particle phase continuity:

$$\rho_p u_p A = w_p \tag{3-8}$$

where ρ_p is the mean density of the cloud of particles, not the density of the solid or liquid material.

Momentum:

$$w_g du_g + w_p du_p + A dp = 0 \qquad (3\text{-}9)$$

where p is the pressure of the gaseous phase only.

Energy:

$$w_g\left[c_{pg}(T_g - T_{go}) + \tfrac{1}{2}u_g^2\right] + w_p\left[c_{pp}(T_p - T_{po}) + \tfrac{1}{2}u_p^2\right] = 0 \qquad (3\text{-}10)$$

where the subscript o indicates the initial condition where the two phases are in kinetic and thermal equilibrium.

State:

$$p = \rho_g R_g T_g \qquad (3\text{-}11)$$

$R_g = R/M_g$

Particle drag:

$$u_p \frac{du_p}{d\bar{x}} = \frac{9}{2}\left(\mu_g f_p \frac{r^*}{m_p r_p^2}\right)(u_g - u_p) \qquad (3\text{-}12)$$

where $f_p = \frac{C_D Re}{24}$ $\left(\frac{\text{drag coefficient}}{\text{Stokes drag coefficient}}\right)$, r^* is the nozzle throat radius, $\bar{x}$ is the nondimensionalized axial coordinate, $\frac{x}{r^*}$.

Particle heat transfer:

$$u_p \frac{dT_p}{d\bar{x}} = -3\left(\frac{\mu_g g_p r^*}{m_p r_p^2}\right)\left(\frac{c_{pg}}{Pr\, c_{pp}}\right)(T_p - T_g) \qquad (3\text{-}13)$$

where $g_p = \frac{Nu}{2}$ $\left(\frac{\text{heat transfer coefficient}}{\text{Stokes heat transfer coefficient}}\right)$.

The momentum and energy equations contain terms which couple the momentum and energy of the two phases. Gas-particle nonequilibrium effects can be anticipated if the characteristic relaxation distances for particle velocity and temperature are of the same order as a characteristic nozzle dimension. Gas-particle nonequilibrium effects will also be more important if the particle mass faction is large.

Similarity of gas-particle flows - Equations (3-12) and (3-13) show that the characteristic relaxation lengths are of the same order for temperature and velocity, and are proportional to the ratio of a characteristic nozzle dimension to the square of the particle size. For the same chamber conditions, two gas-particle nozzle flows will be similar in geometrically similar nozzles if the ratio $\frac{r^*}{r_p^2}$ is the same in both cases. Because particle sizes formed during the combustion process are roughly independent of engine scale, it is not possible to establish nozzle performance by reduced scale testing.

Sound propagation - The momentum equation becomes, by use of eqs. (3-7), (3-10) and (3-11):

$$(Mg^2-1)\frac{du_g}{u_g} + \frac{1}{R_g T_g}\frac{w_p}{w_g}\left[\left(u_g - \frac{\gamma_g - 1}{\gamma_g} u_p\right)du_p - \frac{\gamma_g - 1}{\gamma_g} c_{pp} dT_p\right]$$

$$= \frac{dA}{A} \qquad (3\text{-}14)$$

Now consider an infinitesimal plane pressure discontinuity which is propagating through the two phase medium. Because of the finite relaxation times for the particle velocity and temperature,

these quantities will remain unchanged by the disturbance. The flow area also does not change across a plane disturbance, thus eq. (3-14) becomes

$$(M_g^2-1)\frac{du_g}{u_g} = 0 \qquad (3\text{-}14a)$$

which is the same equation as for a weak disturbance in a gaseous medium. The speed of sound is not affected by the presence of the particles, and it is given by $\sqrt{\gamma_g R_g T_g}$. This situation is similar to sound propagation in a chemically reacting mixture where the sound speed is found to be independent of the finite rate reactions. This result is valid for high frequency disturbances where the time during which the disturbance occurs is much less than the particle relaxation times.

Now consider the case of a low frequency disturbance such that the gas and particles remain in equilibrium. The momentum equation across the disturbance is

$$(M_{eq}^2-1)\frac{du_g}{u_g} = 0 \qquad (3\text{-}14b)$$

where the subscript eq denotes the equilibrium condition. The disturbance propagates at the equilibrium sound speed, $\sqrt{\gamma_{eq} R_g T_g (1+\frac{w_p}{w_g})}$, where

$$\gamma_{eq} = \frac{\gamma_g\left[1+\frac{w_p}{w_g}\frac{c_{pp}}{c_{pg}}\right]}{1+\gamma_g\left(\frac{w_p}{w_g}\frac{c_{pp}}{c_{pg}}\right)}$$

Because $\gamma_{eq} < \gamma_g$, the equilibrium sound speed is less than the speed of sound in the gas. Again, this result is similar to the case of sound propagation in a chemically reacting mixture.

Throat conditions - The second term of eq. (3-14) is always positive for an accelerating flow, therefore, the gas Mach number is always less than one at the geometric throat. At the sonic point (Mg = 1):

$$\frac{1}{R_g T_g} \frac{w_p}{w_g} \left[\left(u_g - \frac{\gamma_g - 1}{\gamma_g} u_p \right) \frac{du_p}{d\bar{x}} - \frac{\gamma_g - 1}{\gamma_g} c_{pp} \frac{dT_p}{d\bar{x}} \right]$$

$$= \frac{1}{A} \frac{dA}{d\bar{x}} \qquad (3\text{-}14a)$$

This equation determines the nozzle mass flow for a gas-particle system. The mass flow depends on the particle lag at the sonic point, and thus the flow is dependent upon the upstream nozzle geometry. The position of the sonic line also depends on the particle lags.

3.2.4 Constant fractional lag nozzles

Kliegel (Ref. 3-6) established a simple solution to the one-dimensional gas-particle equations by assuming that the particles are always in the Stokes' flow regime.

$$C_D = \frac{24}{Re} = \frac{12\mu_g}{\rho_g r_p |u_g - u_p|} = \frac{12\mu_g A u_g}{w_g r_p |u_g - u_p|} \qquad (3\text{-}15)$$

$$Nu = \frac{2hr_p}{k_g} = 2 \qquad \therefore \quad h = \frac{k_g}{r_p} \qquad (3\text{-}16)$$

where h = film coefficient of heat transfer

k_g = gas conductivity

Kliegel found that a family of exact solutions to eqs. (3-7) - (3-16) exists when

$$\frac{u_p}{u_g} = K , \qquad 0 \leq K \leq 1 \tag{3-17}$$

$$\frac{T_{go}-T_p}{T_{go}-T_g} = L \qquad 0 \leq L \leq 1 \tag{3-18}$$

and K and L are constants. Substituting eqs. (3-15) - (3-18) into the earlier equations yields the following equations:

$$\frac{u_g}{\gamma_g R_g T_g}\left[1+\frac{w_p}{w_g}\left\{K\left[\gamma_g(1-K)+K\right]+(\gamma_g-1)\frac{c_{pp}}{c_{pg}}L\left[\frac{1+\frac{w_p}{w_g}K^2}{1+\frac{w_p}{w_g}\frac{c_{pp}}{c_{pg}}L}\right]\right\}-\frac{\gamma_g R_g T_g}{u_g^2}\right]\frac{du_g}{d\bar{x}} = \frac{1}{A}\frac{dA}{d\bar{x}} \tag{3-19}$$

$$\frac{du_g}{d\bar{x}} = \frac{9}{2}\frac{\mu_g r^*(1-K)}{\rho_s r_p^2 K^2} \tag{3-20}$$

where ρ_s represents the density of the particle material.

$$\frac{du_g}{d\bar{x}} = \frac{3}{2}\frac{k_g r^*(1-L)}{\rho_s r_p^2 c_{pp} KL} \tag{3-21}$$

ρ_p = density of the cloud of the whole particles

$$T_g = T_{go} - \frac{1}{2} \frac{u_g^2}{c_{pg}} \left[\frac{1 + \frac{w_p}{w_g} K^2}{1 + \frac{w_p}{w_g} \frac{c_{pp}}{c_{pg}} L} \right] \qquad (3\text{-}22)$$

Equations (3-20) and (3-21) are indentical, therefore,

$$\frac{(1-L)}{L} = \frac{3 \mu_g c_{pp}}{k_g} \frac{(1-K)}{K} = 3 Pr_g \frac{c_{pp}}{c_{pg}} \frac{(1-K)}{K} \qquad (3\text{-}23)$$

For most cases of interest, $Pr_g \frac{c_{pp}}{c_{pg}} > \frac{1}{3}$, so that $L < K$ and the particle thermal lag, $(1-L)$, is greater than the velocity lag $(1-K)$.

Use the following substitutions:

$$B = \frac{1 + \frac{w_p}{w_g} K^2}{1 + \frac{w_p}{w_g} \frac{c_{pp}}{c_{pg}} L} \qquad (3\text{-}24)$$

$$C = 1 + \frac{w_p}{w_g} \left\{ K \left[(1-K)\gamma_g + K \right] + (\gamma_g - 1) \frac{c_{pp}}{c_{pg}} BL \right\} \qquad (3\text{-}25)$$

$$\bar{M} = C^{\frac{1}{2}} M_g \qquad (3\text{-}26)$$

$$\bar{\gamma} = 1 + (\gamma_g - 1) \frac{B}{C} \qquad (3\text{-}27)$$

The equations for the gas particle flow become:

$$\frac{dA}{A} = (\bar{M}^2 - 1)\frac{du_g}{u_g} \tag{3-28}$$

$$\frac{du_g}{d\bar{x}} = \frac{9}{2}\frac{\mu_g r^*(1-K)}{\rho_s r_p^2 K^2} \tag{3-20}$$

Solving these equations, we find that

$$\frac{A^2}{A^{*2}} = \frac{1}{\bar{M}^2}\left[\frac{2}{\bar{\gamma}+1}\left(1+\frac{\bar{\gamma}-1}{2}\bar{M}^2\right)\right]^{\frac{\bar{\gamma}+1}{\bar{\gamma}-1}} \tag{3-29}$$

$$\frac{T_{go}}{T_g} = 1+\frac{\bar{\gamma}-1}{2}\bar{M}^2 \tag{3-30}$$

$$\frac{\rho_{go}}{\rho_g} = \left[1+\frac{\bar{\gamma}-1}{2}\bar{M}^2\right]^{\frac{1}{\bar{\gamma}-1}} \tag{3-31}$$

$$\frac{p_{go}}{p_g} = \left[1+\frac{\bar{\gamma}-1}{2}\bar{M}^2\right]^{\frac{\bar{\gamma}}{\bar{\gamma}-1}} \tag{3-32}$$

$$\frac{u_g}{u_{gmax}} = \left[\frac{(\bar{\gamma}-1)\bar{M}^2}{2+(\bar{\gamma}-1)\bar{M}^2}\right]^{\frac{1}{2}} \tag{3-33}$$

$$u_g = \frac{9}{2} \frac{\mu_g r^*(1-K)}{\rho_s r_p^2 K^2} \bar{x} \qquad (3\text{-}34)$$

and

$$u_{gmax} = \left[\frac{2c_{pg} T_{go}}{B} \right]^{\frac{1}{2}} \qquad (3\text{-}35)$$

The particle velocity and temperature are given by eqs. (3-17) and (3-18). Equations (3-28) - (3-33) are the equations for one-dimensional isentropic flow, except that $\bar{\gamma}$ and $\bar{M}$ replace γ and M. One can, therefore, use the isentropic gas tables to compute the flow through a constant fractional lag nozzle. For equilibrium, K = L= 1, and $\bar{\gamma}$ and $\bar{M}$ become γ_{eq} and M_{eq}.

Equation (3-28) shows that $\bar{M} = 1$ at the throat of a constant fractional lag nozzle. The parameter C is greater than one, therefore, $M_g < 1$ at the throat. A plot of the M_g at the throat is shown in fig. 3-2 for a typical metallized solid propellant. $M_g\big|^*$ increases as the particle lag increases, and is only weakly dependent on the particle mass fraction.

The mass flow through the nozzle is also dependent on the particle lags, and therefore is dependent on the upstream nozzle geometry. The mass flow through a constant fractional lag nozzle is shown in fig. 3-3 for typical metallized propellants. The mass flow increases as the particle lags increase, and is strongly dependent on the particle lags.

The effective expansion coefficient, $\bar{\gamma}$, is shown in fig. 3-4 as a function of the particle lag for typical metallized

propellants. The effective expansion coefficient increases with increasing particle lag, but is relatively insensitive for small particle lags.

Nozzle geometry - Using eqs. (3-29), (3-33) and (3-34), we can show that the area variation in a constant fractional lag nozzle is given by

$$\frac{A}{A^*} = \left[\frac{\bar{\gamma}-1}{\bar{\gamma}+1}\right]^{\frac{1}{2}} \left[\frac{2}{\bar{\gamma}-1}\right]^{\frac{1}{\bar{\gamma}-1}} \frac{1}{Z} \left[\frac{1}{1-Z^2}\right]^{\frac{1}{\bar{\gamma}-1}} \qquad (3\text{-}36)$$

where

$$Z = \frac{9\mu_g r^*(1-K)}{2\rho_s r_p^2 K^2} \frac{\bar{x}}{u_{gmax}} \qquad (3\text{-}37)$$

A plot of $\frac{r}{r^*}$ is shown in fig. 3-5 for a constant fractional lag nozzle. The nozzle is approximately symmetrical through the throat, and most of the nozzle length is in the throat region.

One can show from eqs. (3-36) and (3-37) that the wall radius of curvature at the throat is given by

$$\frac{R_s}{r^*} = \frac{2u_g^{*2}}{(\bar{\gamma}+1)r^{*2}\left[\frac{du_g}{d\bar{x}}\right]^{*2}} = \frac{2}{(\bar{\gamma}+1)}\left[\frac{2}{9}\frac{\rho_s r_p^2 K^2}{\mu_g(1-K)}\frac{u_g^*}{r^*}\right]^2 \qquad (3\text{-}38)$$

where $\left[\frac{du_g}{d\bar{x}}\right]^*$ is the axial velocity gradient at the throat.

Note that the middle term of eq.(3-38) is the same as obtained by Sauer for a pure gas flow (section 2.3.3).

Solving eq. (3-38) for K, we obtain the following relation between particle lag and nozzle throat geometry:

$$K = \frac{9}{4} \frac{\mu_g r^*}{\rho_s r_p^2 u_g^*} \left[\frac{\bar{\gamma}+1}{2} \frac{R_s}{r^*} \right]^{\frac{1}{2}} \left\{ \left[1 + \frac{8}{9} \frac{\rho_s r_p^2 u_g^*}{\mu_g R^*} \left(\frac{\bar{\gamma}+1}{2} \frac{R_s}{r^*} \right)^{\frac{1}{2}} \right]^{\frac{1}{2}} - 1 \right\} \tag{3-39}$$

Fractional lag vs throat size is shown in fig. 3-6 for various particle diameters. The wall radius of curvature is equal to the throat radius.

For small particle lags, eq.(3-39) is approximately

$$1-K \approx \frac{2}{9} \frac{\rho_s r_p^2 u_g^*}{\mu_g r^*} \left(\frac{2}{\bar{\gamma}+1} \frac{r^*}{R_s} \right)^{\frac{1}{2}} \tag{3-40}$$

If the above dimensionless number is very small, gas-particle nonequilibrium effects will be negligible.

Equation (3-34) shows that the axial velocity gradient is constant for the constant fractional lag nozzle. This condition is approximately true in the throat region in most rocket nozzles, and it appears that the above results have general applicability.

Flow outside Stokes' regime - It has been observed that $\frac{C_D Re}{Nu} \approx 12$ even outside Stokes' regime, therefore, the relationship

between particle velocity and thermal lags is unchanged. The axial dimensions of the nozzle are changed because

$$\frac{du_g}{d\bar{x}} = \frac{9}{2} \frac{\mu_g f_p r^*}{\rho_s r_p^2} \frac{1+K}{K^2} \qquad (3\text{-}41)$$

when the particle is not in the Stokes' regime.

If a suitable mean value for f_p is chosen, the flow up to the nozzle throat may be predicted with reasonable accuracy by the constant fractional lag solution. To apply the equations for a constant fractional lag nozzle, replace μ_g in the equations by $f_p \mu_g$.

Particle solidification - It has been assumed up to this point that the particles do not undergo phase change. Constant lag nozzle flow with particle solidification will be briefly discussed here.

Assume that the particle temperature remains constant during solidification, and denote the condition at the onset of solidification by the subscript m. From eqs. (3-10), (3-13) and (3-34), the equation governing the gas temperature during solidification is given by

$$u_g \frac{dT_g}{d\bar{x}} - \frac{3k_g r^* w_p}{w_g c_{pg} \rho_s r_p^2 K} (T_{pm} - T_g) + \frac{9}{2} \frac{\mu_g r^* (1-K)}{\rho_s r_p^2 K^2} \left[1 + \frac{w_p}{w_g} K^2\right] \frac{u_g^2}{c_{pg}} =$$

(3-42)

$T_{solid} = 2319^{\circ}K$ $\}$ Al_2O_3 $\Delta H_{solid} = 254$ cal/gram.

$c_{pl} \simeq 0.34$

$c_{ps} \simeq 0.34$

Solving eq.(3-42), with the boundary conditions at the beginning of solidification ($T_p = T_{pm}$, $u_g = u_{gm}$, $T_g = T_{gm}$) we find that

$$T_g = T_{gm} - \left[\frac{1+\frac{w_p}{w_g}K^2}{1+\frac{1}{3}\frac{w_p}{w_g}\frac{K}{Pr_g(1-K)}}\right]\frac{u_g^2}{2c_{pg}} - \left\{T_{pm} - T_{gm} - \left[\frac{1+\frac{w_p}{w_g}K^2}{1+\frac{1}{3}\frac{w_p}{w_g}\frac{K}{Pr_g(1-K)}}\right]\frac{u_{gm}^2}{2c_{pg}}\right\}\left[\frac{u_g}{u_{gm}}\right]^{-\frac{2}{3}\frac{w_p}{w_g}\frac{K}{Pr_g(1-K)}} \qquad (3\text{-}43)$$

where

$$T_{gm} = T_{go} - \frac{(T_{go}-T_{pm})}{L} \qquad (3\text{-}44)$$

and

$$u_{gm} = \left\{\left[\frac{1+\frac{w_p}{w_g}\frac{c_{pp}}{c_{pg}}L}{1+\frac{w_p}{w_g}K^2}\right]\frac{2c_{pg}}{L}(T_{go}-T_{pm})\right\}^{\frac{1}{2}} \qquad (3\text{-}45)$$

The gas undergoes an isothermal expansion ($T_g = T_{pm}$) only if there is no particle lag (which implies an infinite heat transfer coefficient). From eqs. (3-18) and (3-29) - (3-31) we find that the area ratio at the onset of solidification is

$$\frac{A_m}{A^*} = \frac{u_g^*}{u_{gm}} \left[\frac{T_g^* L}{T_{p_m} - (1-L) T_{go}} \right]^{\frac{1}{\gamma-1}} \qquad (3\text{-}46)$$

For most cases of interest, $T_{pm} < T_g^*$, so that particle solidification can only occur in the divergent section of the nozzle. The minimum area ratio at which solidification can occur is obtained when there is no lag (L = 1). The area ratio, $\frac{A_m}{A^*}$, becomes infinite when $L = 1 - \frac{T_{pm}}{T_{go}}$. To make most efficient use of the particle solidification energy one must have a low lag nozzle so that the heat of solidification is added to the flow at the lowest possible area ratio.

It is possible in principle to solve eq.(3-43), along with the other governing equations, for all of the flow properties during solidification. The required integrals cannot be expressed in closed form, however, because of the last term of eq.(3-43). Kliegel stated that further investigation must be carried out numerically (Ref. 3-6). Kliegel did work out the special case of a zero lag flow during particle solidification. More recently, Kliegel stated that appreciable particle solidification rarely occurs in rocket nozzles of engineering interest (Ref. 3-2).

3.2.5 Inputs for numerical solutions of gas-particle flows

The generalized equations for onedimensional gas-particle flow can only be solved numerically. As pointed out by Hoglund (Ref. 3-1), the following information is needed for

numerical solution of the equations:

1. particle size distribution (or average particle size)
2. particle drag and heat transfer coefficients
3. gas viscosity and conductivity
4. gas and particle heat capacities

The information on particle size and physical properties is also necessary for application of the constant fractional lag solution. Hoglund (Ref. 3-1) presented a detailed discussion of the state of knowledge of these quantities, up to 1962.

Particle size distribution - The size of the condensed metallic oxide particles depends in a complicated way on the incompletely understood processes of metal combustion and oxide condensation. Most of the numerical computations are based on the experimental particle size distribution obtained by Brown (Ref. 3-7) for aluminum oxide particles. Brown found a mean particle size of about one micron, with a mean particle weight corresponding to between 2 and 3 microns. The distribution of particle sizes obtained by Brown is shown in Fig. 3-7. Brown found that the particle size distribution was independent of engine size, geometry, propellant composition or chamber pressure. These results were obtained from rather large engines.

More recently, Sehgal (Ref. 3-8) has presented experimental particle size distributions obtained by firing small aluminized solid propellant rockets into a collection tank. He found that the particle size is independent of aluminum loading, combustion temperature and convergent nozzle geometry. The solid aluminum oxide particles were found to near-perfect

spheres containing negligible amounts of unburned aluminum . In contrast to Brown's results, Sehgal found that particle size is strongly dependent on chamber pressure, with the volume average diameter under 0.5 micron for p_c = 5 atm and almost 5 microns for p_c = 68 atm. Sehgal also found that the particle size is dependent on the residence time in the chamber, with a larger residence time decreasing the particle diameter. In view of the uncertainties in Sehgal's results for small rockets, Brown's results are probably more reliable since they were obtained from rather large scale engines.

Very little is known about the particle sizes for metallic fuels other than aluminum .

Particle drag coefficient - Early numerical computations were made with C_D obtained from the standard drag curve for spheres, which is empirical for Re > 1. Hoglund (Ref. 3-1), in his discussion of the drag coefficient , indicated that the following factors should be considered for the gas-particle flow in rocket nozzles:

1. Rarefaction effects
2. Compressibility
3. Free stream acceleration
4. Free stream turbulence.

Kliegel (Ref. 3-2) noted that, for the particle size distribution of Brown in a typical rocket, only rarefaction effects are important. He recommended use of the standard drag curve, along with the rarefaction corrections of Schaaf and Chambre (Ref.3-8).

Hoglund commented that the effect of free stream turbulence could be quite large. Limited experimental results indicate that large scale free stream turbulence causes the drag coefficient to decrease sharply, which is detrimental to the performance of a two phase nozzle flow.

More recently (1964), Carlson and Hoglund (Ref. 3-9), investigated the flow regimes for typical gas-particle flows. They found that the slip flow regime ($\frac{\sqrt{Re}}{M} \simeq 100$) is encountered near the throat, with increasing rarefaction effects downstream of the throat. The maximum particle Reynolds number probably does not greatly exceed 100. Carlson and Hoglund suggested the following empirical relation for the sphere drag coefficient, which includes rarefaction, compressibility and inertial effects:

$$C_D = \frac{24}{Re} \frac{(1+0.15\ Re^{0.687}) \left[1+\exp\left\{\frac{0.427}{M^{4.63}} - \frac{3.0}{Re^{0.88}}\right\}\right]}{1+\frac{M}{Re}\left[3.82+1.28\exp(-1.25\ \frac{Re}{M})\right]} \qquad (3\text{-}47)$$

M and Re are based on the velocity relative to the particle.

Particle heat transfer coefficient - Carlson and Hoglund (Ref. 3-9) suggested the following expression for Nu, based on the continuum expression of Drake and the transition regime expression of Kavanau and Drake:

$$Nu = \frac{2+0.459\ Re^{0.55}}{1+3.42(\frac{M}{Re})(2+0.459\ Re^{0.55})} \qquad (3\text{-}48)$$

Because thermal lag has much less influence on nozzle performance than does particle lag, the uncertainty in Nu is less serious than uncertainty in C_D.

Physical properties of gas and particles - The thermodynamic properties are probably the best known of the input quantities. The gas transport properties are less well established, especially for reacting gases. The most important transport property is the viscosity because it affects directly the particle velocity lag. Hoglund (Ref. 3-1) estimated that the transport properties can be calculated with an accuracy of $\pm$ 10% if the Chapman-Enskog theory for pure nonpolar monatomic is used with the empirical mixture rules presented by Hirschfelder, Curtiss and Bird (Ref. 3-10).

3.2.6 Generalized one dimensional solutions

Kliegel and Nickerson (Ref. 3-11), Bailey, et al. (Ref. 3-12) and others have programmed the generalized one dimensional gas-particle flow equations (eqs. 3-7 to 3-13) for computer solution. Some of the results presented by Kliegel (Ref. 3-2) will be discussed here. The particle sizes were those of Brown (Fig. 3-7), and the nozzle geometry is shown in Fig.3-8.

The axial distribution of the one dimensional gas velocity is shown in fig. 3-9, along with the prediction of the constant fractional lag theory. The velocity and temperature lags are shown in figs. 3-10 and 3-11. Note that particle solidification occurs within the nozzle only for very small particles.

The ratio of particle density to gas density is shown in fig. 3-12. It is seen that the velocity lag causes the density ratio in the nozzle to be higher than the initial value. The relative increase in the particle mass in the nozzle occurs during the starting transient.

The nozzle efficiency, defined as $I_{sp}/I_{sp\ eq}$, is shown in fig. 3-13. Finite particle lags cause an appreciable thrust loss, most of which occurs upstream of the throat. Figs.(3-9)-(3-13) indicate that the constant fractional lag solution is excellent at the throat and fairly good for the rest of the nozzle.

3.3 ANALYSIS OF AXISYMMETRIC GAS-PARTICLE FLOWS

The one dimensional solutions are incapable of predicting the detailed nature of the particle streamlines relative to the gas streamlines. The important problems of particle impingement on the wall and nozzle optimization depend on a detailed treatment of the axisymmetric two phase flow.

3.3.1 Uncoupled analysis of axisymmetric flow

Bailey, et al. (Ref. 3-12) determined particle trajectories in a prescribed gas flow field. This technique provides useful results when the particle mass fraction is small. The axisymmetric analysis predicts a strong segregation of the various particle sizes, with the large particles being concentrated along the nozzle axis.

FEIN - Theoretical Model for predicting particle size in single sheet in Rocket exhausts

AIAA J. Vol 4. No 1. June 1966. Pg 92

Travis (Ref. 3-13) also treated the uncoupled axisymmetric problem for typical rocket nozzle configurations. He considered the case where the particles have a radial velocity component in the chamber, and found that the throat region is where most of the wall impingement occurs. The effect of wall impingement on heat transfer was treated in an approximate manner. Travis concluded that, to minimize wall impingement, the particles should be directed in an axial direction while the gas velocities are low.

3.3.2 Coupled axisymmetric solutions

Kliegel and Nickerson (Ref. 3-11) were the first to treat the coupled axisymmetric flow in a gas-particle nozzle. It was found that the method of characteristics could be extended to the gas-particle flow problem when $M_g > 1$. Hoffman (Ref. 3-3) has also treated the axisymmetric flow in a manner similar to that of Kliegel and Nickerson.

Assumptions - The analysis incorporates the same assumptions as used for the generalized one dimensional analysis. Both Kliegel and Nickerson and Hoffman have approximated the particle size distribution by groups of different size spheres. For simplicity, however, we will consider here only a single particle size.

Basic equations - The following equations govern the steady, axisymmetric, gas-particle flow (Ref. 3-3):

Gas continuity equation:

$$\rho_g \frac{\partial u_g}{\partial x} + \rho_g \frac{\partial v_g}{\partial r} + u_g \frac{\partial \rho_g}{\partial x} + v_g \frac{\partial \rho_g}{\partial r} = - \frac{\rho_g v_g}{r} \quad (3\text{-}49)$$

Particle continuity equation:

$$\rho_p \frac{\partial u_p}{\partial x} + \rho_p \frac{\partial v_p}{\partial r} + u_p \frac{\partial \rho_p}{\partial x} + v_p \frac{\partial \rho_p}{\partial r} = - \frac{\rho_p v_p}{r} \quad (3\text{-}50)$$

The axial momentum equation:

$$\rho_g u_g \frac{\partial u_g}{\partial x} + \rho_g v_g \frac{\partial u_g}{\partial r} + A\rho_p (u_g - u_p) + \frac{\partial p}{\partial x} = 0 \quad (3\text{-}51)$$

where

$$A = \frac{9}{2} \frac{f_p \mu_g}{\rho_s r_p^2} \quad (3\text{-}52)$$

The radial momentum equation

$$\rho_g u_g \frac{\partial v_g}{\partial x} + \rho_g v_g \frac{\partial v_g}{\partial r} + A\rho_p (v_g - v_p) + \frac{\partial p}{\partial r} = 0 \quad (3\text{-}53)$$

Energy equation

$$u_g \frac{\partial p}{\partial x} + v_g \frac{\partial p}{\partial r} - c^2 \left[u_g \frac{\partial \rho_g}{\partial x} + v_g \frac{\partial \rho_g}{\partial r} \right] - A\rho_p B \quad (3\text{-}54)$$

where

$$B = (\gamma_g - 1) \left[(u_g - u_p)^2 + (v_g - v_p)^2 + \frac{2}{3} C(T_p - T_g) \right] \quad (3\text{-}55)$$

and

$$C = \frac{g_p}{f_p} \frac{c_{pg}}{Pr_g} \quad (3\text{-}56)$$

Particle drag in axial direction

$$u_p \frac{\partial u_p}{\partial x} + v_p \frac{\partial u_p}{\partial r} = A(u_g - u_p) \qquad (3\text{-}57)$$

Particle drag in radial direction

$$u_p \frac{\partial v_p}{\partial x} + v_p \frac{\partial v_p}{\partial r} = A(v_g - v_p) \qquad (3\text{-}58)$$

Particle heat balance

$$u_p \frac{\partial h_p}{\partial x} + v_p \frac{\partial h_p}{\partial r} = -\frac{2}{3} AC(T_p - T_g) \qquad (3\text{-}59)$$

Equation of state for gas

$$p_g = \rho_g R_g T_g \qquad (3\text{-}60)$$

Equation of state for the particles

$$T_p = f(h_p) \qquad \text{(tabulated)} \qquad (3\text{-}61)$$

Speed of sound in gas

$$c^2 = \gamma_g R_g T_g \qquad (3\text{-}62)$$

Definition of Mach number

$$M_g^2 = \frac{(u_g^2 + v_g^2)}{c^2} \qquad (3\text{-}63)$$

Viscosity-temperature relation for gas

$$\mu_g = \mu_g(T) \qquad \text{(tabulated)} \tag{3-64}$$

Method of characteristics - Equations (3-49) - (3-53) and (3-57) - (3-59) form a set of 4 quasi-linear, nonhomogeneous partial differential equations of first order. It has been shown that this set of equations may be solved by use of the method of characteristics (see Ref. 3-3 for a complete discussion). The following characteristic equations result:

Along the gas streamlines:

$$\frac{dr}{dx} = \frac{v_g}{u_g} \tag{3-65}$$

$$\rho_g\left[u_g du_g + v_g dv_g\right] + dp = -A\rho_p\left[(u_g - u_p)dx + (v_g - v_p)dr\right] \tag{3-66}$$

and

$$\frac{dp}{p} - \gamma_g \frac{d\rho_g}{\rho_g} = \frac{A\rho_p B dx}{p u_g} \tag{3-67}$$

Along the gas Mach lines:

$$\frac{dr}{dx} = \frac{u_g v_g \pm c^2\sqrt{M_g^2 - 1}}{u_g^2 - c^2} \tag{3-68}$$

and

$$(u_g dr - v_g dx)(A\rho_p B dx - u_g dp) + c^2 \left\{ A\rho_p \left[(u_g - u_p)dr - (v_g - v_p)dx \right] dx \right.$$

$$\left. + \rho_g \left[v_g du_g - u_g dv_g - \frac{v_g}{r}(u_g dr - v_g dx) \right] dx + dp dr \right\} = 0 \quad (3\text{-}69)$$

Along the particle streamlines:

$$\frac{dr}{dx} = \frac{v_p}{u_p} \quad (3\text{-}70)$$

$$u_p du_p = A(u_g - u_p)dx \quad (3\text{-}71)$$

$$v_p dv_p = A(v_g - v_p)dr \quad (3\text{-}72)$$

$$u_p dh_p = -\frac{2}{3} AC(T_p - T_g)dx \quad (3\text{-}73)$$

$$\partial \psi_p = 0 \quad (3\text{-}74)$$

$$\frac{\partial \psi_p}{\partial r} = \rho_p u_p \quad (3\text{-}75)$$

and

$$\frac{\partial \psi_p}{\partial x} = -\rho_p v_p \quad (3\text{-}76)$$

where ψ_p is the particle stream function.

This set of characteristic equations is completely hyperbolic for $M_g > 1$, and the flow may be determined by numerical solution of eqs. (3-65) - (3-76). Equation (3-68) indicates that the characteristics in the physical plane are identical to the gas Mach lines, and are independent of the presence of the particles in the flow.

Unit process

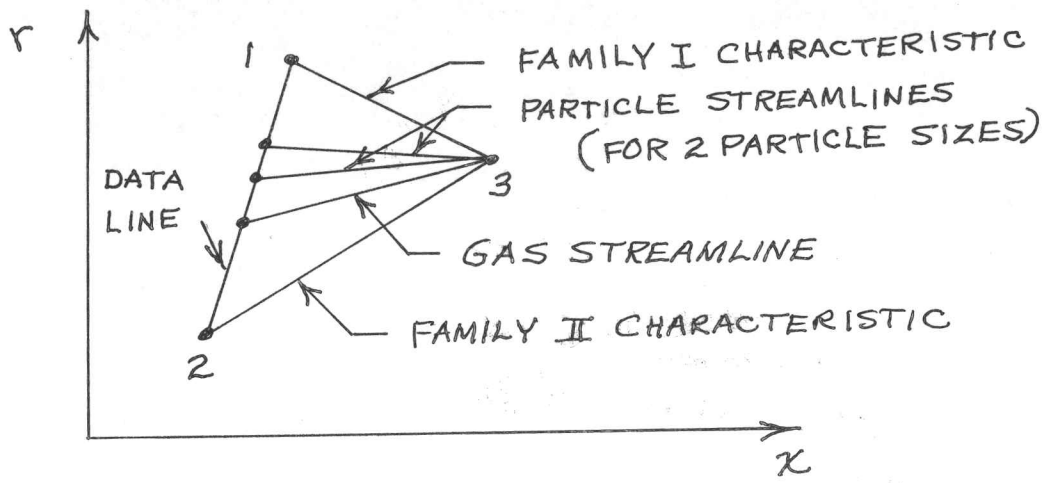

The calculation procedure is similar to the case of rotational gas flow, with the additional complication that one must calculate both the gas streamlines and the particle streamlines.

Subsonic and transonic flow - When $M_g < 1$ the gas Mach lines are imaginary. The gas and particle streamlines are real, however, and the characteristic equations can be employed to determine the particle streamlines if the velocity components, u_g and v_g, can be determined by some other procedure. Some simplification of the original problem is obtained even when the complete method of characteristics solution is not applicable.

The procedure of Kliegel and Nickerson (and also of Hoffman) is to use the generalized one dimensional solution (section 3.2.5) for the subsonic section of the nozzle. Instead of using the plane cross sectional area, a one dimensional sink flow model is assumed where the area is a spherical cap.

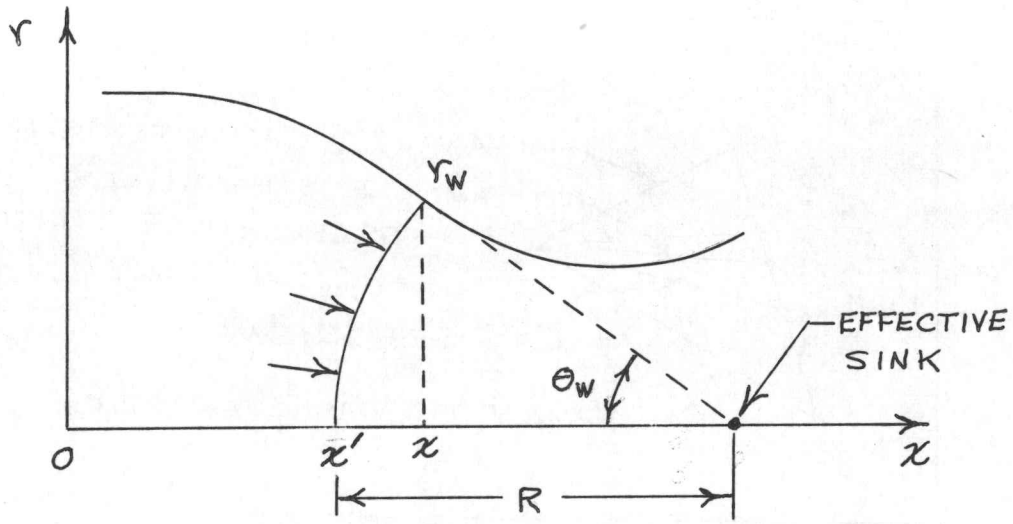

The solution is similar to the source flow analysis for conical nozzles (section 2.5.1) except that the position of the effective sink varies with the local wall slope, θ_w. The area of the spherical cap, A', is given by

$$A' = 2\pi R^2(1-\cos\theta) \tag{3-77}$$

$$R = \frac{r_w}{\sin\theta_w} \tag{3-78}$$

$$x' = x-R(1-\cos\theta) \tag{3-79}$$

Using the relation for A', the solution is continued until the solution diverges because of the $\sqrt{1-M_g^2}$ term. In general, $M_g < 1$ at the geometrical throat, so the subsonic solution can be calculated up to the throat. The mass flow through the nozzle is established by conditions downstream of the throat, where $M_g = 1$. To initiate the subsonic and transonic flow solutions, the mass flow must be estimated, and subsequently corrected to agree with the mass flow at the supersonic starting line. The

initial estimate may be obtained by using the constant lag analysis (section 3.2.4).

The transonic flow field between the throat and the supersonic starting line is determined by using the constant lag analysis. By using the effective parameters $\bar{\gamma}$ and $\bar{M}$ (with K* determined by the subsonic analysis), the Sauer technique is used to determine the flow up to the supersonic starting line. The mass flow along this line is compared with the estimated mass flow, and the subsonic and transonic solutions are repeated until the two mass flows agree.

The subsonic and transonic gas flow field is now established, and the method of characteristics is used to calculate the particle streamlines up to the supersonic starting line.

Typical results - Kliegel (Ref. 3-2) presented some results of his axisymmetric analysis for the nozzle geometry of Fig. 3-8. The particle size distribution of Brown (Fig. 3-7) was used in the calculations.

Kliegel found that the particles are unable to follow the gas streamlines downstream of the throat, and that there is a limiting particle streamline for each particle size. The limiting streamlines for the nozzle of fig. 3-8 are shown in fig. 3-14.

The tendency of the particles to congregate near the axis is illustrated by fig. 3-15, which shows the particle density distribution at the nozzle exit plane. The steps in the particle density distribution result from approximating the

particle size distribution by a finite number of groups of particles.

The axial distributions of gas velocity and temperature, at the wall and at the nozzle axis, are shown in figs. 3-16 and 3-17.

The nozzle efficiency, $I_{sp}/I_{sp\ eq}$, is shown in fig. 3-18. The generalized one dimensional analysis agrees qualitatively with the axisymmetric analysis, and underestimates the loss in I_{sp} by less than 1%.

Hoffman and Lorenc (Ref. 3-14) have used the axisymmetric analysis to make a parametric study of gas-particle flows in conical nozzles.

Comparison with experiments - Kliegel and Nickerson (Ref. 3-11) compared the results of the axisymmetric analysis with experimental results from several small solid propellant engines. To separate the losses caused by gas-particle flow from other losses, calculations were made for the heat losses and friction losses. The results for six different conical nozzles are shown in the following table ($r^* = 3.35$ cm).

A_e/A^*	3.5	20	24	24	24	24
R_s/r^*	2	2	2	5	5	5
Cone angle, θ_w, deg	25.2	21.5	24	12	18	24
Calculated heat loss, %	0.6±.2	0.8±.2	0.9±.3	1.3±.4	1.1±.3	1.0±.3
Calculated friction losses, %	0.7±.2	1.5±.3	1.4±.4	2.9±.9	2.0±.6	1.6±.5
Experimental $I_{sp}/I_{sp\ id}$ x 100	95.4±.3	94.7±.3	94.7±.6	95.1±.3	95.1±.3	95.1±.3
Measured gas-particle losses, %	3.3±.7	3.0±1.0	3.0±1.3	0.7±1.6	1.8±1.2	2.3±1.1
Calculated gas-particle losses, %	5.0±1.0	4.8±1.0	4.9±1.0	3.5±1.0	4.1±1.0	4.6±1.0

It should be noted that the experimental performance is predicted just as well by Kliegel's one dimensional analysis.

The effect of nozzle throat geometry on nozzle efficiency is shown in fig. 3-19 for a rocket with a convergent nozzle. The effect of subsonic nozzle geometry is shown in fig. 3-20.

The effect of gas-particle flow on the performance of contoured nozzles is illustrated in fig. 3-21. All the nozzles had the same length and area ratio, but different maximum wall angles. The axisymmetric theory predicts accurately the optimum maximum wall angle of approximately 26°. Note that the performance of the best contoured nozzle is only about 1% better than a conical nozzle of the same length. The performance improvement of contoured nozzles over conical nozzles is generally considerably less for gas-particle flows than for pure gas flows.

Lorenc and Hoffman (Ref. 3-15) have reported similar experimental results for a series of rocket engines. The axisymmetric theory of Hoffman was found to predict the effect of nozzle geometry to within about 1% of the experimental results. Their results indicate that the optimum maximum wall angle for contoured nozzles is about 22-24°, slightly less than the result of Kliegel and Nickerson.

3.4 EXPERIMENTAL TECHNIQUES FOR GAS-PARTICLE FLOWS

Carlson (Ref. 3-16) presented experimental results for particle thermal lags. A slurry of M_gO particles (of known size) in RPI was used for the rocket fuel. He measured the gas temperature by using the sodium D-line technique, and used the particle emission to determine the particle temperature. Carlson obtained excellent correlation between his experimental results and the prediction of a simple axisymmetric gas-particle theory.

The experimental determination of particle velocities is much more difficult. Carlson (Ref. 3-17) determined experimental velocity lags in his slurry-fueled rocket. The extinction of emission from a tungsten filament lamp was related to the particle density, which in turn was related to velocity lag. The experimental results show considerable scatter, but the results agree fairly well with the theoretical prediction.

Fulmer and Wirtz (Ref. 3-18) measured particle velocities by means of streak photographs. A two dimensional convergent nozzle was used with helium. Experimental velocity lags of aluminum particles up to 40 microns were found to be less than predicted by constant lag theory.

Dobbins (Ref. 3-19) used a light scattering technique to determine the diameter of the particles used in Carlson's experiments. Good agreement with the predetermined particle sizes was obtained, indicating that the method may have considerable usefulness.

3.5 NOZZLE DESIGN CONSIDERATIONS

In view of the uncertainties in the input parameters, such as particle diameter and drag coefficient, the axisymmetric theories provide surprisingly accurate predictions of gas-particle nozzle flows. The greatest drawback in the use of these theories is their extreme numerical complexity. In many cases, the simpler one dimensional theory provides equally accurate prediction of overall nozzle performance, but the one dimensional theory can provide no information on particle impingement or on the effect of nozzle contouring.

The results of many investigators lead to several generalizations about the design of gas-particle nozzles:

1. Thrust losses up to 5% can occur because of particle lag in nozzles of practical scale.
2. Most of the thrust loss can be attributed to the throat region and appears as a loss in c^* rather than a loss in C_F. This points out why c^* is a poor indicator of combustion efficiency for solid propellant rockets.
3. No appreciable recovery of the thrust loss is obtained by making the supersonic section very long.
4. The best way to reduce the thrust loss is to add length to the nozzle throat region.
5. A constant radius of wall curvature through the throat is recommended to prevent large local velocity gradients.
6. The subsonic nozzle geometry has measurable effect on the overall performance.
7. Nozzle contouring is less effective for gas-particle flows than for pure gas flows.

8. For a given particle size, the thrust loss is dependent on engine scale (see fig. 3-22 for typical results).
9. Subscale nozzle testing is less useful for gas-particle flows than for pure gas flows.

In contrast to the case of pure gas flow, no rigorous optimization technique is currently available for gas-particle nozzles. Marble (Ref. 3-21) used one dimensional theory, linearized with the assumption of small lags, to determine optimum thrust nozzle contours. His optimum nozzle has essentially the same characteristics as Kliegel's constant lag nozzle: long gradual throat contour and a divergent section without an inflection point. The analytical model, however, is too unrealistic to yield reliable results on the relative merits of various nozzle shapes. It appears that the best alternative at this time is to use the complete axisymmetric theory to make parameter studies of various nozzle configurations. The most promising contour can then be selected on an empirical basis.

REFERENCES

3-1 HOGLUND: Recent advances in gas-particle nozzle flows.
ARS Jnl, vol. 32, no 5, May 1962, p. 662.

3-2 KLIEGEL: Gas particle nozzle flows.
Ninth Symposium (International) on Combustion.
Academic Press, New York, 1963, p. 811.

3-3 HOFFMAN: An analysis of the effects of gas-particle mixtures on the performance of rocket nozzles.
Purdue University, Jet Propulsion Center, Report no TM-63-1 (AD 408270), January 1963.

3-4 ALTMAN & CARTER: Expansion processes, two phase flow, High Speed Aerodynamics and Jet Propulsion, Vol. II, Combustion Processes, Princeton University Press, Princeton, 1956, pp. 52-63.

3-5 GILBERT, DAVIS & ALTMAN: Velocity lag of particles in linearly accelerated combustion gases.
Jet Propulsion, vol. 25, no 1, Jan.1955, pp 26-30.

3-6 KLIEGEL: One dimensional flow of a gas particle system.
Space Technology Laboratories, TR 59-0000-00746, July 1959.

3-7 BROWN: Particle size of condensed oxides from combustion of metallized solid propellants.
Eight Symposium (International) on Combustion, The Williams and Wilkins Company, Baltimore, 1962, p.814.

3-8 SEHGAL: An experimental investigation of a gas-particle system.
Jet Propulsion Laboratory TR No32-238 (AD 274314), March 1962.

3-9 CARLSON & HOGLUND: Particle drag and heat transfer in rocket nozzles.
AIAA Jnl, vol. 2, no 1, November 1964, pp. 1980-1984.

3-10 HIRSCHFELDER, CURTISS & BIRD: Molecular theory of gases and liquids.
John Wiley & Sons, New York, 1954.

3-11 KLIEGEL & NICKERSON: Flow of gas-particle mixtures in axially symmetric nozzles.
Progress in Astronautics and Rocketry, vol. 6, Detonation and two phase flow.
Academic Press, New York, 1962
(also ARS, Preprint 1713-61).

3-12 BAILEY, et al.: Gas particle flow in an axisymmetric nozzle.
ARS Jnl, vol. 31, no 6, June 1961, pp. 793-798.

3-13 TRAVIS: Heat transfer and particle trajectories in solid rocket nozzles.
Aerojet-General Report no 0162-01 TN-17 (AD 289681) October 1962.

3-14 HOFFMAN & LORENC: A parametric study of gas-particle flows in conical nozzles.
AIAA Jnl, vol. 3, no 1, January 1965, p. 103.

3-15 LORENC & HOFFMAN: Correlation of performance of conical and contoured nozzles for gas-particle flow.
AIAA Jnl, vol. 4, no 1, Jan. 1966, p. 169.

3-16 CARLSON: Experimental determination of thermal lag in gas-particle nozzle flow.
ARS Jnl, vol. 32, no 7, July 1962, p. 1107.

3-17 CARLSON: Experimental determination of velocity lag in gas-particle nozzle flow .
AIAA Jnl, vol. 3, no 2, February 1965, p. 354.

3-18 FULMER & WIRTZ: Measurement of individual particle velocities in a simulated rocket exhaust.
AIAA Jnl, vol. 3, no 8, August 1965, p. 1506.

3-19 DOBBINS: Measurement of mean particle size in a gas-particle flow.
AIAA Jnl, vol. 1, no 8, August 1963, p. 1940.

3-20 GILBERT, ALLPORT & DUNLAP: Dynamics of two-phase flow in rocket nozzles.
ARS Jnl, vol. 32, no 12, December 1962, p. 1929.

3-21 MARBLE: Nozzle contours for minimum particle-lag loss.
AIAA Jnl, vol. 1, no12, December 1965, p. 2793.

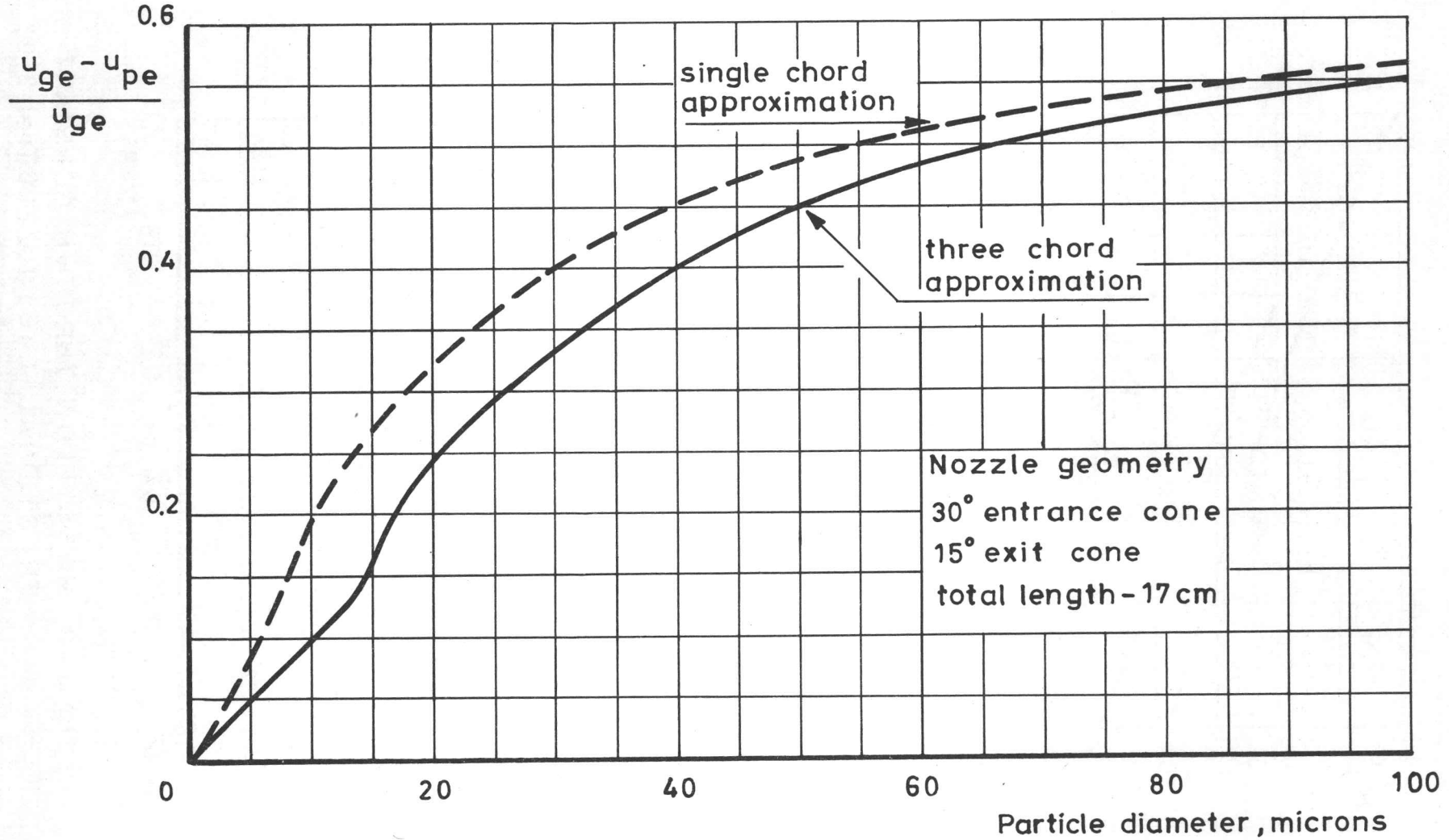

Fig. 3-1 PARTICLE LAG AT NOZZLE EXIT FOR TYPICAL ROCKET (ref. 3-5)

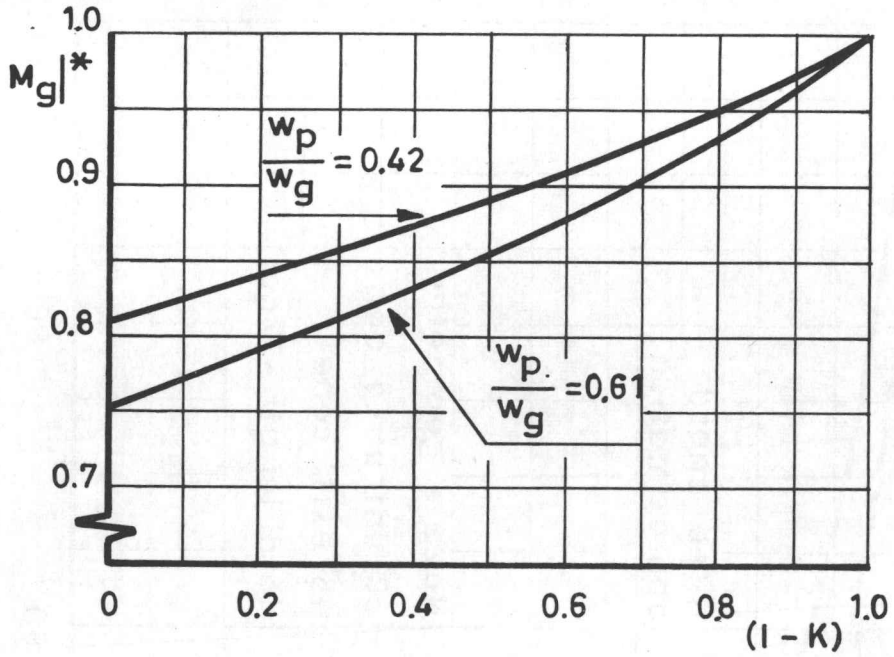

Fig. 3-2 GAS MACH NUMBER AT THROAT OF A CONSTANT FRACTIONAL LAG NOZZLE (ref. 3-2)

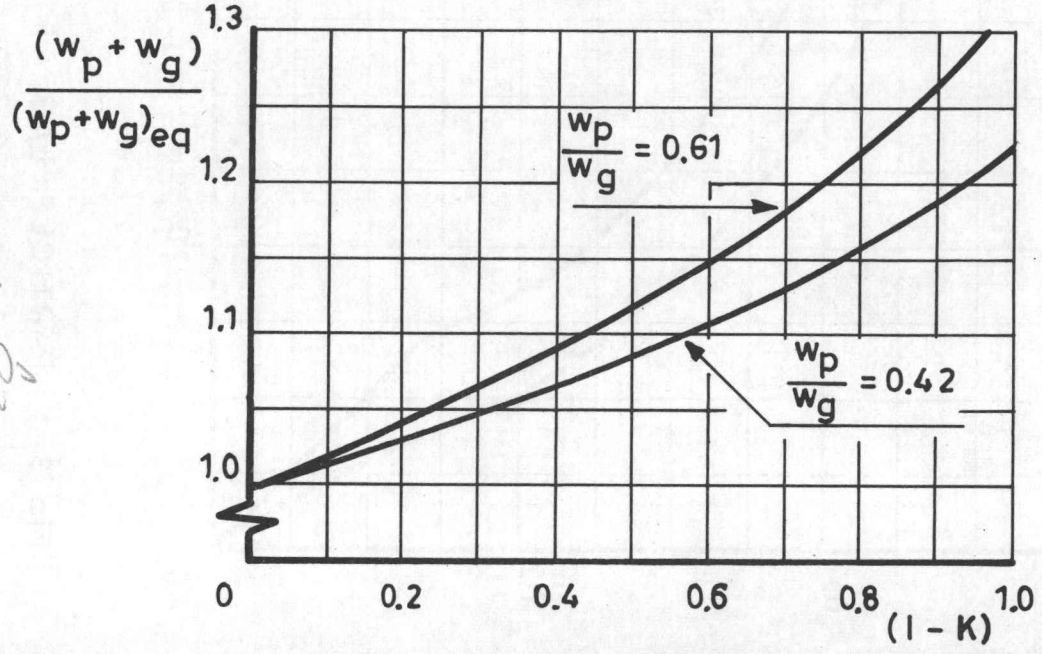

Fig. 3-3 MASS FLOW THROUGH CONSTANT FRACTIONAL LAG NOZZLE (ref. 3-2)

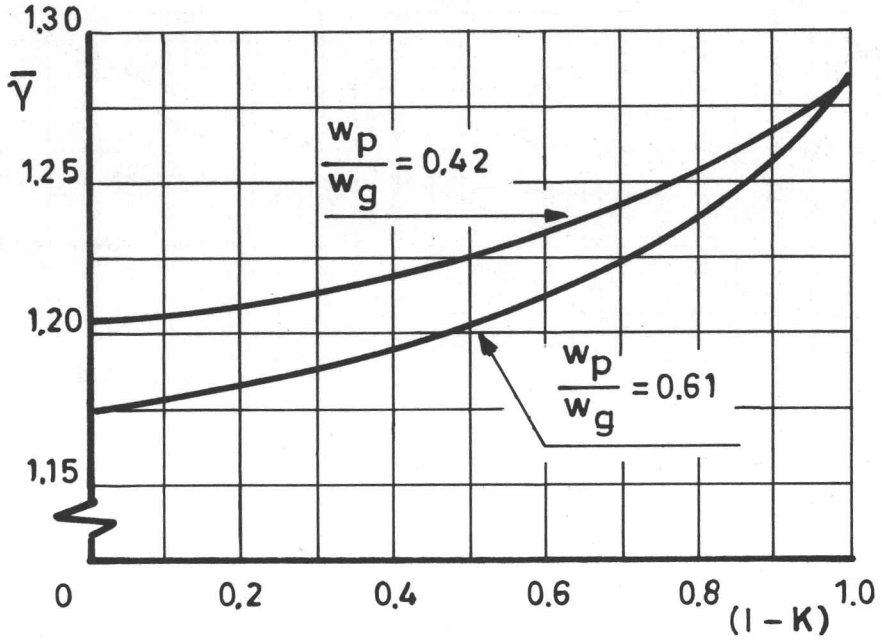

Fig. 3-4 EFFECTIVE EXPANSION COEFFICIENT IN A CONSTANT FRACTIONAL LAG NOZZLE (ref. 3-2)

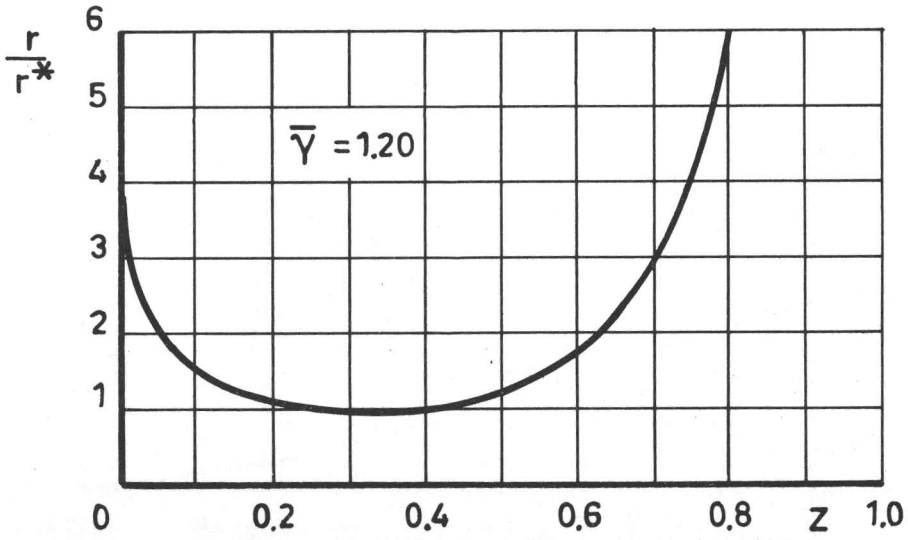

Fig. 3-5 CONSTANT FRACTIONAL LAG NOZZLE PROFILE (ref. 3-6)

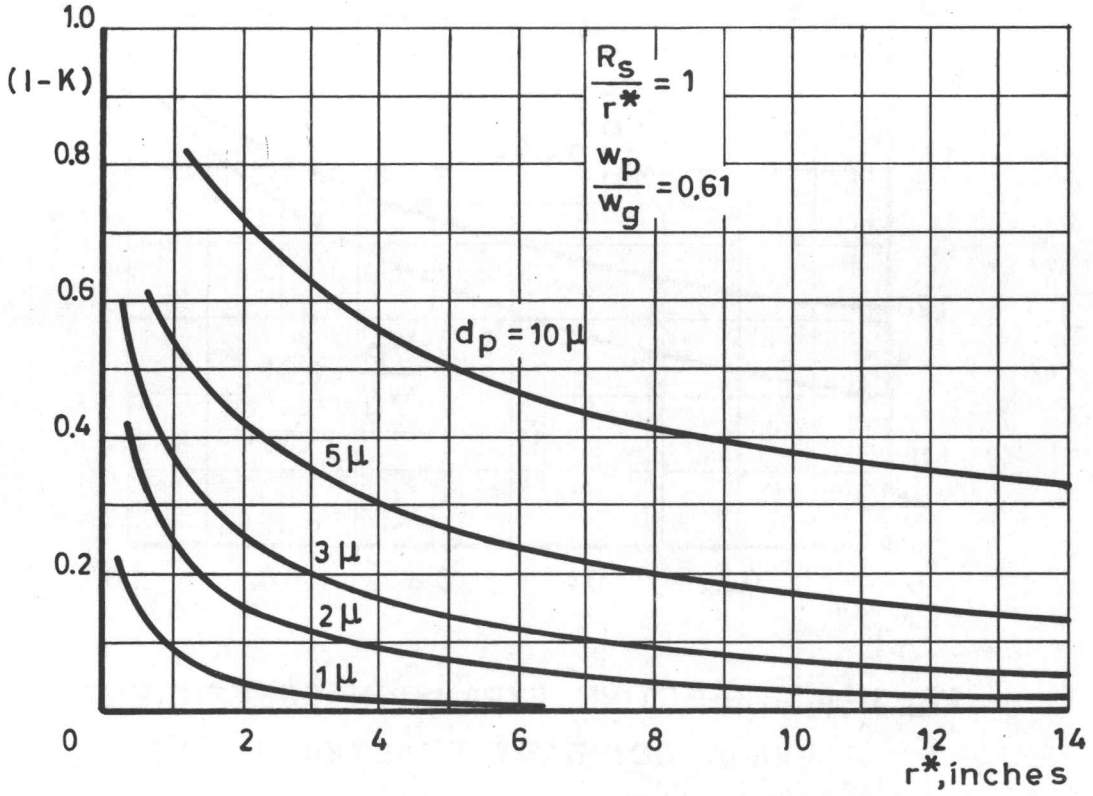

Fig. 3-6 PARTICLE VELOCITY LAG FOR CONSTANT FRACTIONAL LAG NOZZLES (ref. 3-2)

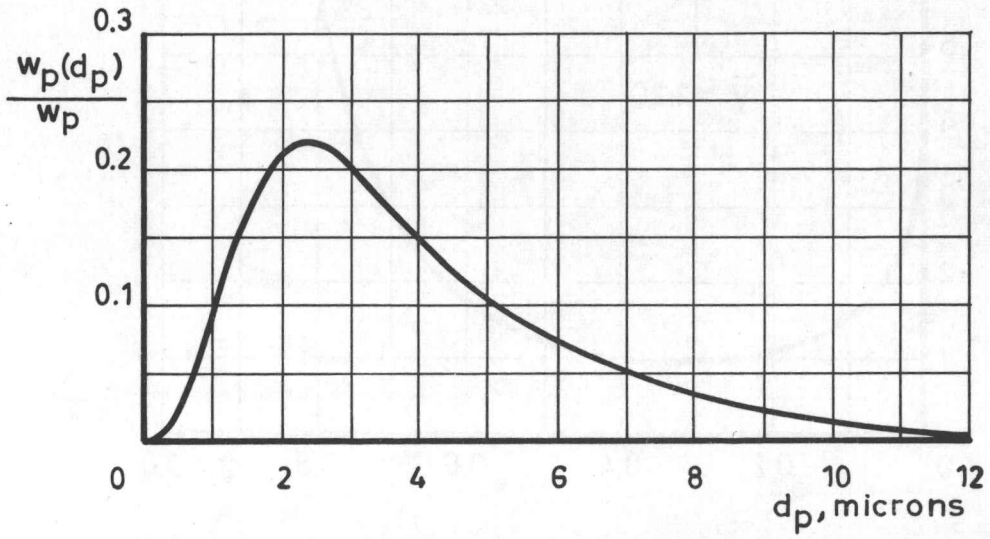

Fig. 3-7 EXPERIMENTAL PARTICLE SIZE DISTRIBUTION (ref. 3-7)

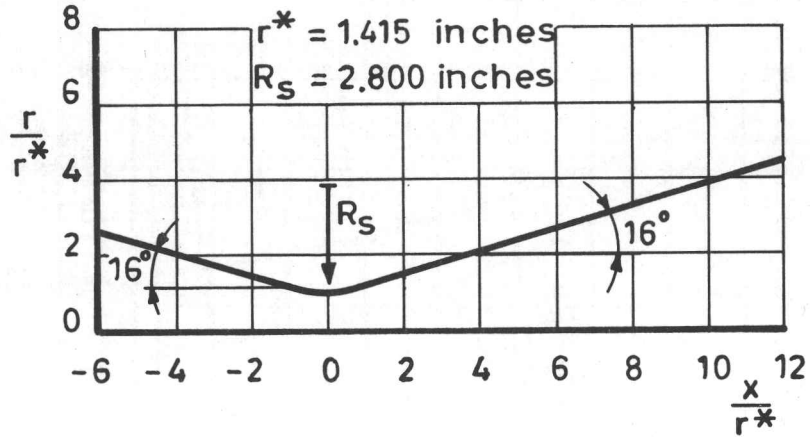

Fig. 3-8 KLIEGEL'S NOZZLE GEOMETRY (ref. 3-2)

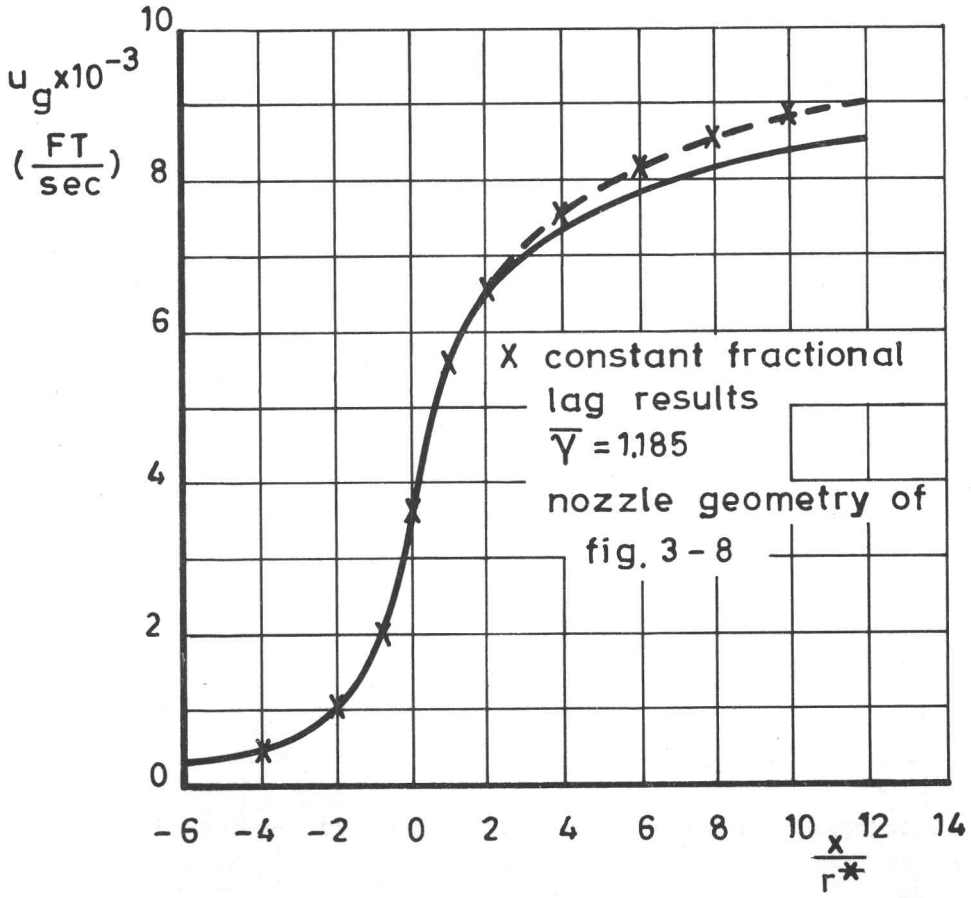

Fig. 3-9 ONE DIMENSIONAL GAS VELOCITY PROFILE (ref. 3-2)

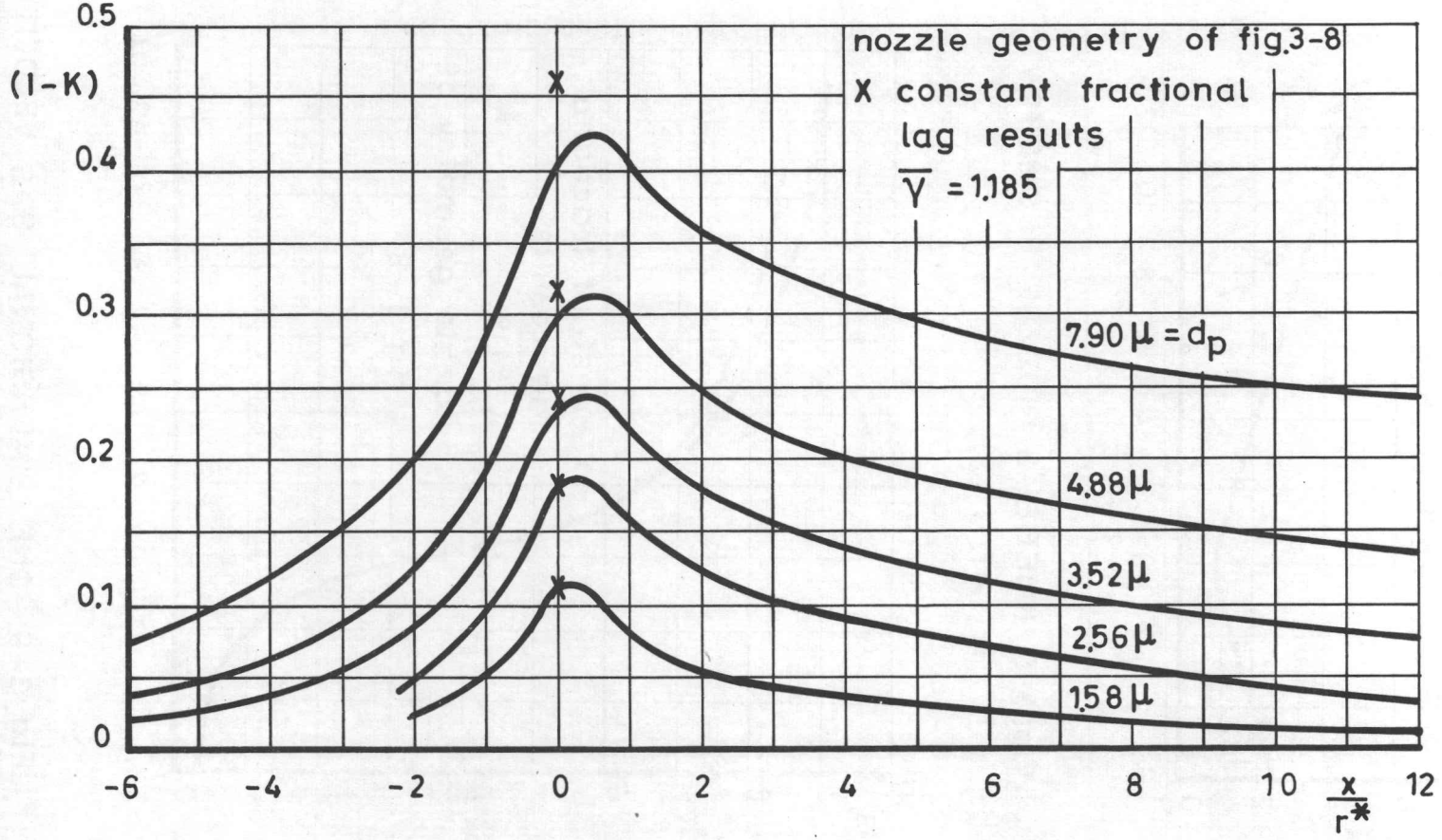

Fig. 3-10 ONE DIMENSIONAL PARTICLE VELOCITY LAGS (ref. 3-2)

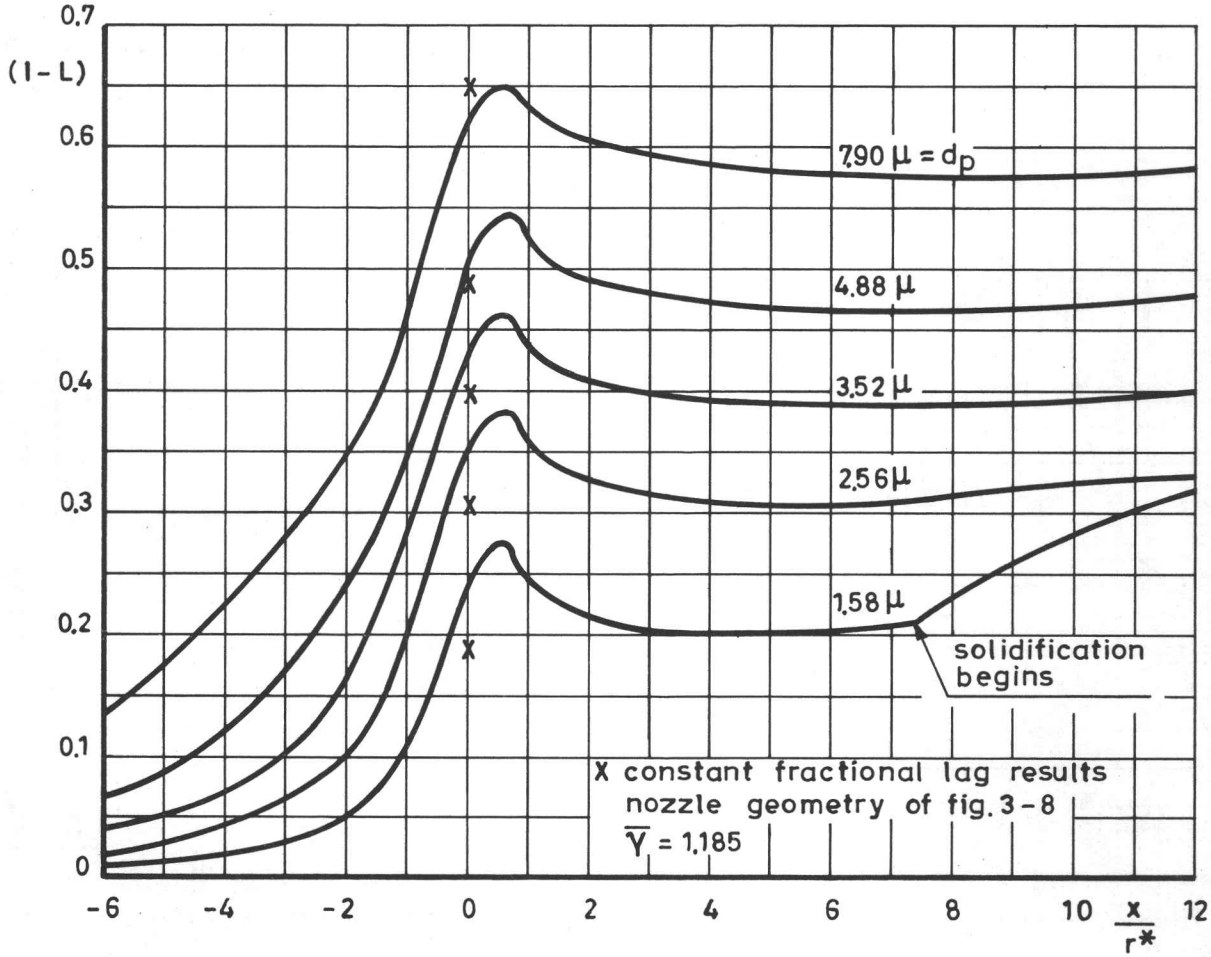

Fig. 3 - 11 ONE DIMENSIONAL PARTICLE TEMPERATURE LAGS (ref. 3 - 2)

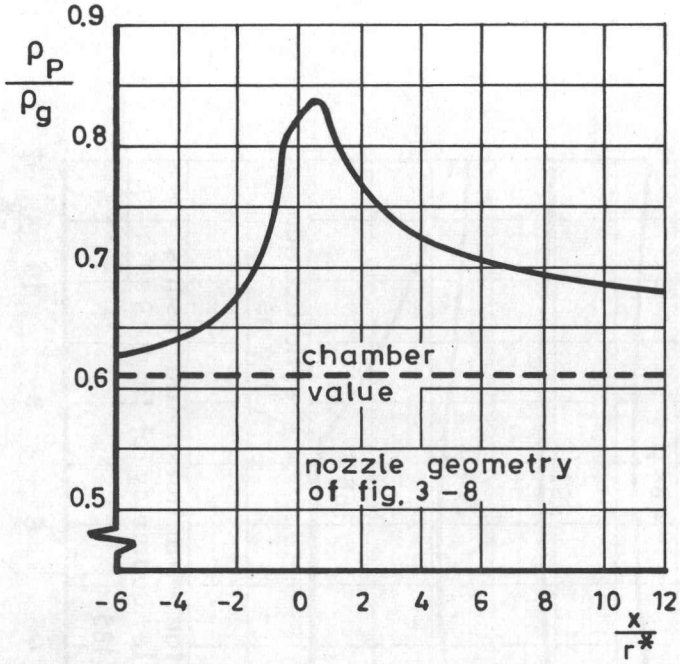

Fig. 3-12 ONE DIMENSIONAL GAS-PARTICLE DENSITY RATIO (ref. 3-2)

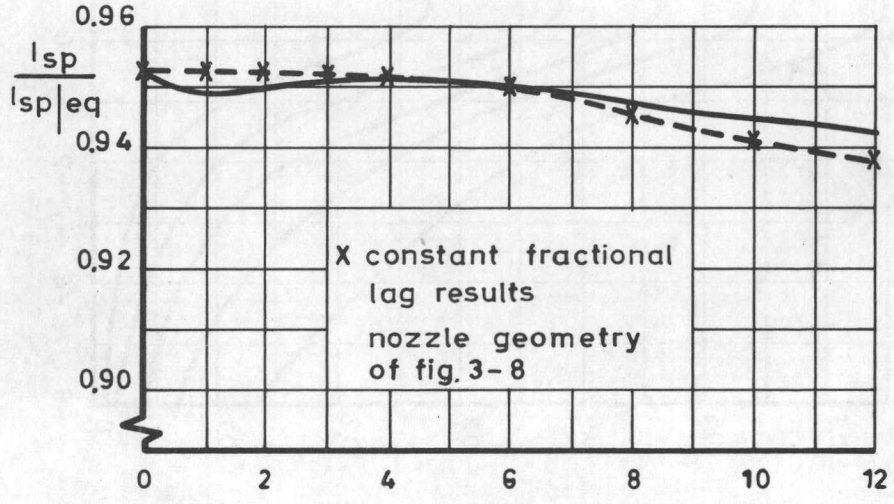

Fig. 3-13 ONE DIMENSIONAL NOZZLE EFFICIENCY (ref. 3-2)

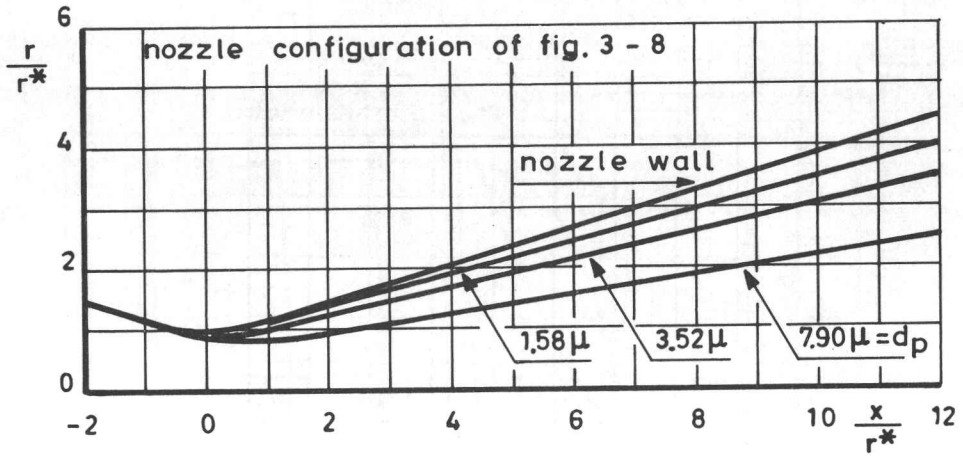

Fig. 3 - 14 LIMITING PARTICLE STREAMLINES (ref. 3 - 2)

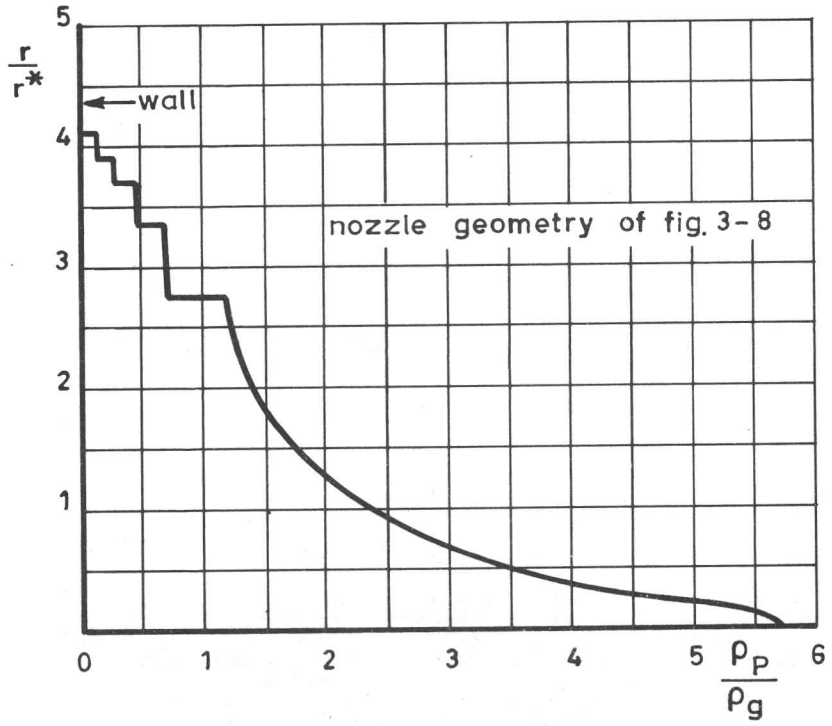

Fig. 3 - 15 RADIAL DISTRIBUTION OF PARTICLE DENSITY AT NOZZLE EXIT PLANE (ref. 3 - 2)

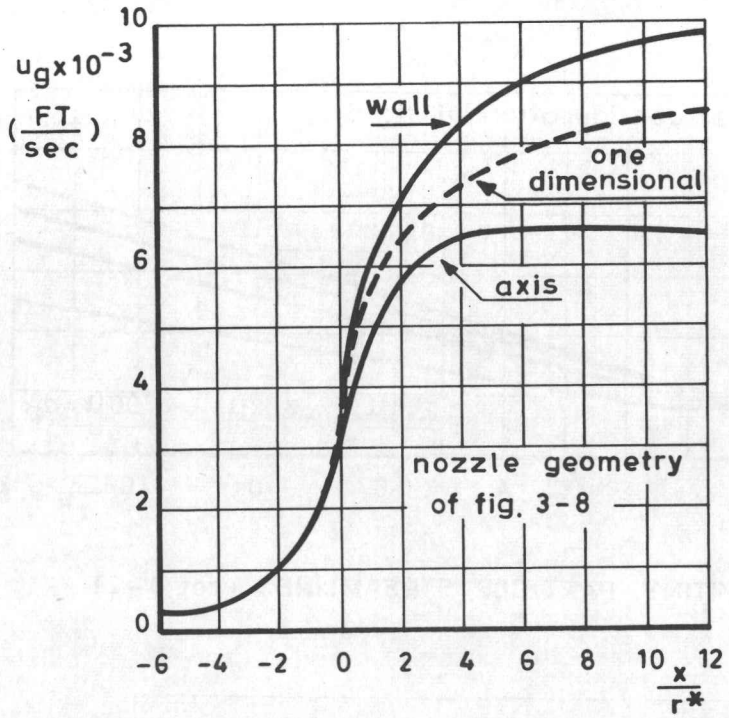

Fig. 3-16 AXIAL DISTRIBUTION OF GAS VELOCITY(ref.3-2)

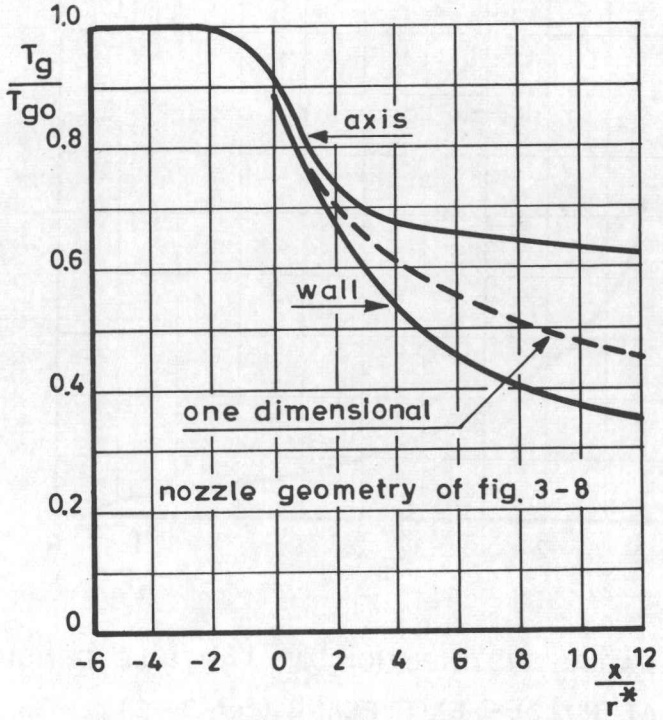

Fig. 3-17 AXIAL DISTRIBUTION OF GAS TEMPERATURE (ref.3-2)

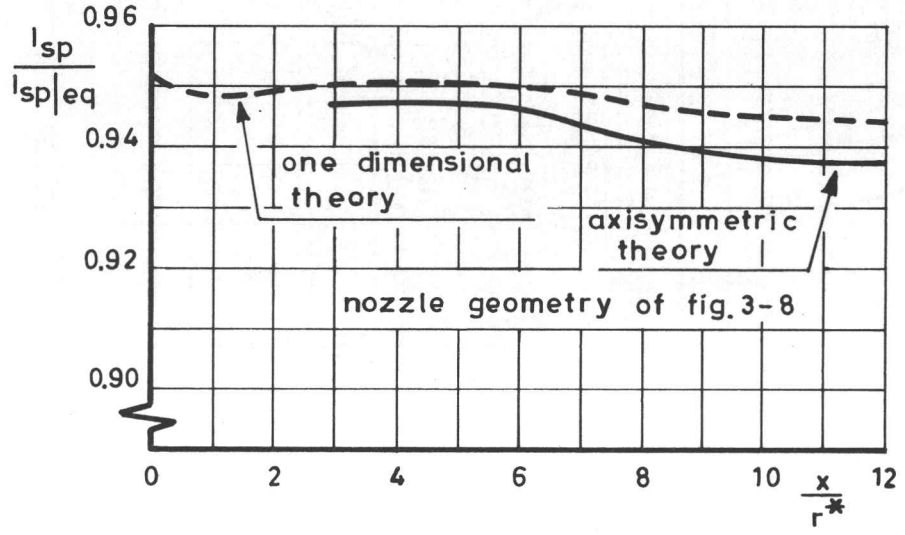

Fig. 3-18 NOZZLE EFFICIENCY (ref. 3-2)

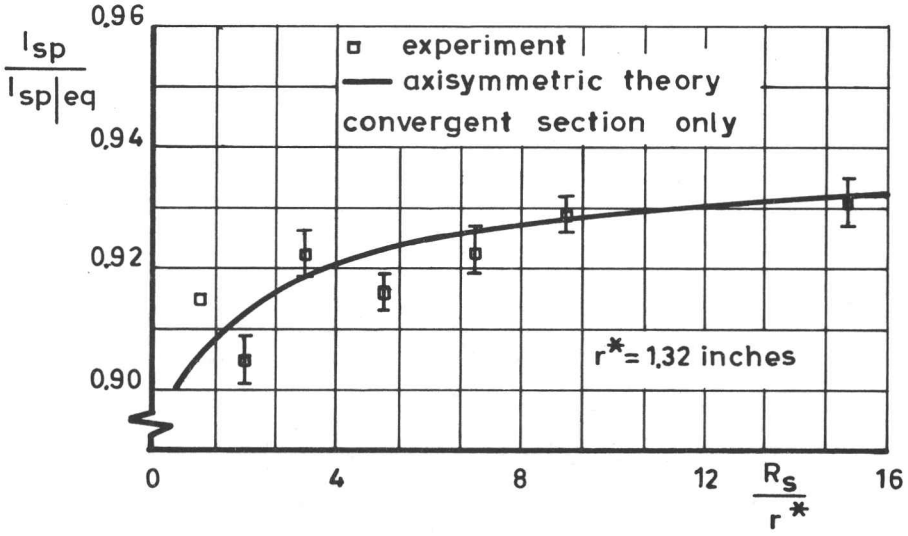

Fig. 3-19 EFFECT OF NOZZLE THROAT GEOMETRY ON NOZZLE PERFORMANCE (ref. 3-11)

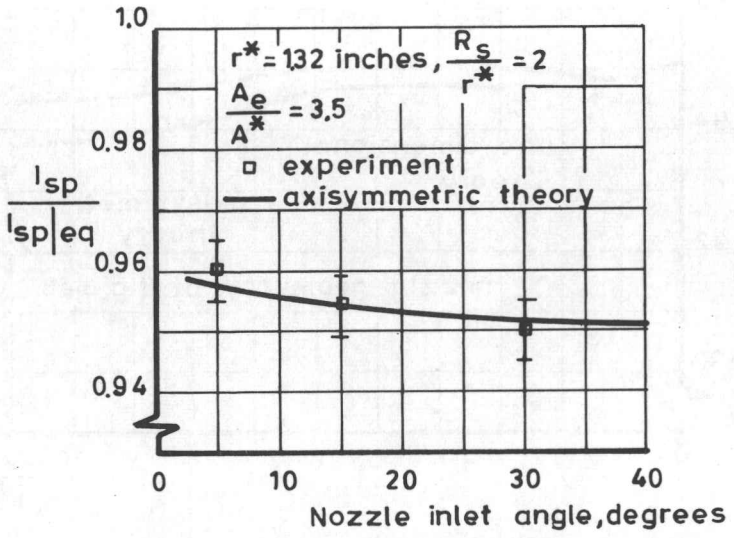

Fig. 3 - 20 EFFECT OF INLET GEOMETRY ON NOZZLE EFFICIENCY (ref. 3 - 11)

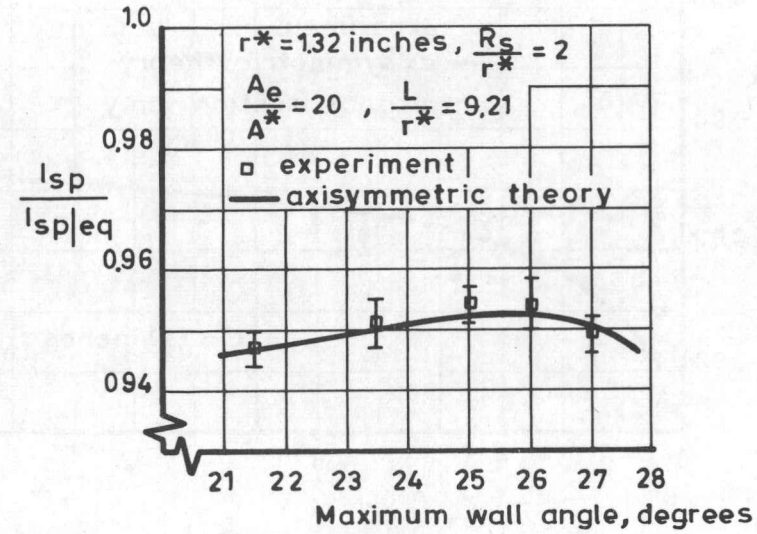

Fig. 3 - 21 PERFORMANCE OF CONTOURED NOZZLES (ref. 3 - 11)

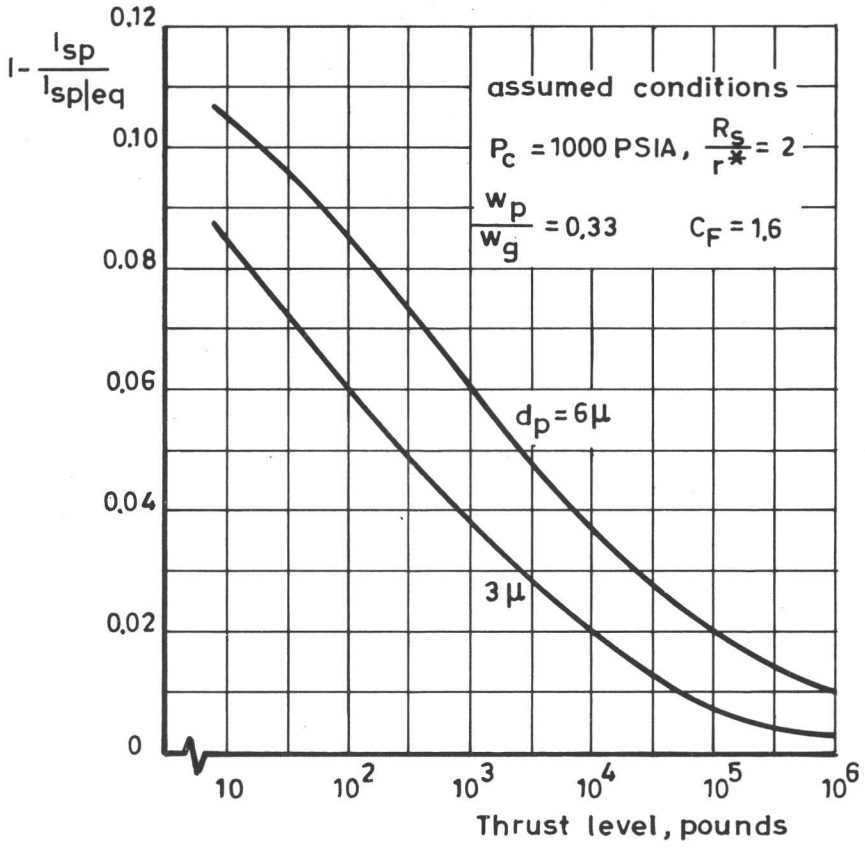

Fig. 3-22 EFFECT OF ROCKET SCALE ON GAS-PARTICLE THRUST LOSSES (ref. 3-20)

CHAPTER 4

THRUST VECTOR CONTROL

4.1 METHODS OF THRUST VECTOR CONTROL

Some method of providing transverse thrust forces is necessary for the guidance and control of a rocket propelled missile. Several techniques for providing the transverse control forces have been used or proposed:

1. Aerodynamic surfaces
2. Auxiliary jets
3. Rocket engine gimballing
4. Vanes in the exhaust stream
5. Jet tabs
6. Jetavators
7. Secondary injection into the exhaust nozzle.

The first two methods are independent of the main rocket engine. Aerodynamic surfaces are useful in the lower atmosphere, but cannot be used for flight at high altitudes or at low vehicle speeds. Auxiliary jets, either small vernier rockets or jets of inert gas, may be used to provide the control forces. Multiple jets are necessary to provide control of both pitch and yaw.

Methods 3-7 provide the vector control forces by deflecting the jet of the main rocket engine. Gimballing of the complete rocket engine is feasible for liquid propellant engines which have flexible propellant supply lines. Although the

actuation forces are not large, the gimbal bearings must withstand the entire thrust of the rocket. Gimballing is not practical for solid propellant rockets because of the large size of the combustion chamber which contains all of the propellant. In principle, it would be possible to pivot the nozzle independently of the combustion chamber, but the high temperature sealing problem is extremely difficult.

Vanes, jet tabs (fig. 4-1a) and jetavators (fig.4-1b) deflect the main exhaust stream by placing a mechanical obstacle in the stream. Vanes in the exhaust stream are effective, but are subject to severe erosion, and also cause a permanent loss of axial thrust. Jet tabs and jetavators are immersed in the exhaust stream only during the time that control forces are required, and do not cause a permanent loss of axial thrust. Rather complex actuation devices are required for each of the mechanical jet deflection methods of thrust vector control.

Hausmann (ref. 4-1) first suggested the technique of injecting a secondary fluid through a port in the divergent part of the main exhaust nozzle. The injected fluid forms an obstruction, which causes a shock wave and asymmetrical pressure forces on the wall of the nozzle (fig. 4-1c). Because of the interaction with the main flow, the side force generated is much larger than would result from using the same secondary fluid as an auxiliary jet. Secondary injection thrust vector control (SITVC) avoids erosion and sealing problems, is simple and compact, has high frequency response, and is applicable to solid propellant rockets. Because of these advantages, many experimental and theoretical investigations of SITVC have been

made in recent years. The remainder of this chapter is devoted to a brief description of analytical and experimental results on SITVC.

Both liquids and gases have been proposed for use as secondary injectants. Liquids are desirable from the standpoint of packaging and handling, but the side force is usually larger for a gaseous injectant.

Description of flow - The effectiveness of SITVC depends on the interaction of the injected fluid with the main nozzle flow. The general features of the interaction process are illustrated in the following sketch.

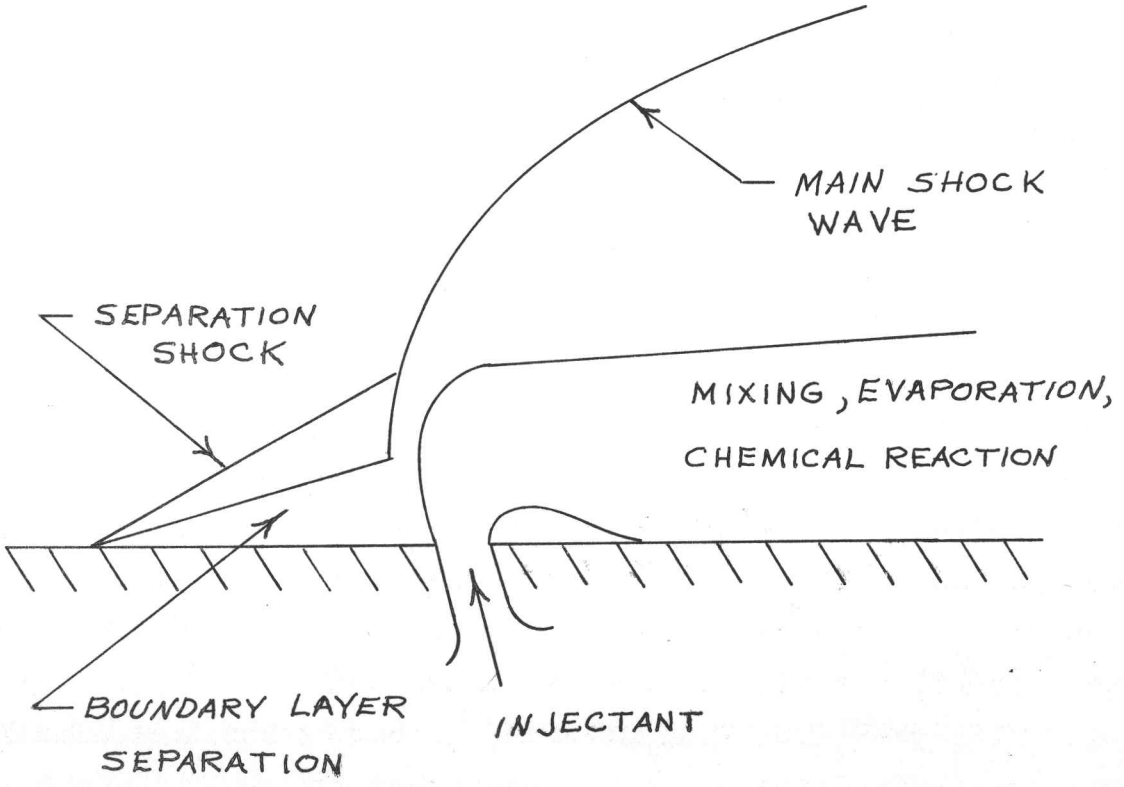

The flow pattern upstream of the injection port is similar to the flow near the nose of a blunt body in free flight. The effective blunt body shape is determined by the properties of the injectant. One major exception to the blunt body analogy is the interaction with the wall boundary layer, which does not occur in free flight. The shock wave travels outward from the initial disturbance and intersects the rocket nozzle along a line which is approximately parabolic.

The side force on the rocket nozzle consists of two components, the initial thrust of the injected fluid and the resulting pressure interaction forces on the nozzle wall. As the injectant flow rate is increased, the main shock becomes steeper and the intersection of the main shock wave with the nozzle wall advances up the wall. Eventually, the shock wave intersects the opposite wall of the nozzle, and the pressure forces are not exerted in the desired direction. This loss in side force performance is termed "cosine loss".

4.2 EXPERIMENTAD RESULTS FOR SECONDARY INJECTION THRUST VECTOR CONTROL

The flow mechanisms of SITVC are extremely complex, and the initial developments on the concept were based primarily on experimental studies. More recently, several different analytical approaches have been developed which have varying degrees of usefulness, depending on the particular application.

4.2.1 General experiments on secondary injection

Several investigators have made wind tunnel studies

of the flow pattern resulting from a transverse jet injected into the supersonic flow along a flat plate. Amick and Hays (ref. 4-3) presented pressure distributions and normal force measurements, using air for the injected fluid. Zukowski and Spaid (ref. 4-4) made an experimental study of the flow field around the injection port at free stream Mach numbers from 1.38 to 4.54. Gaseous nitrogen, argon and helium were used for the injectants. Measurements were made of the main shock shape, length of separated flow region, and pressure distributions on the plate. In addition, the penetration height and rate of mixing downstream of the injection port were determined by concentration measurements. Both laminar and turbulent boundary layers on the plate were observed. As expected, the length of the boundary layer separation region upstream of the port was much larger for the laminar boundary layer.

Bankston and Barnes (ref. 4-5) measured the shock wave and pressure effects of air injection into a two dimension nozzle having glass walls.

4.2.2 Secondary injection into axisymmetric nozzles

Numerous investigators have made side force measurements for injection of various fluids into axisymmetric nozzles. Rodriguez (ref. 4-6) used nozzles having $A_e/A^* = 16$ and 25, with injection at various axial stations. The main stream fluid used was cold air, and also the products of LOX-RPI combustion. Air and LOX-RPI mixtures were used for the secondary injectant. For most of the experiments, the injection port was a convergent nozzle oriented normal to the wall or inclined 30° upstream. Data were presented on the total side force, and

also on the increment of axial thrust produced by injection.

Walker, Stone and Shandor (ref. 4-7) made side force measurements in a conical nozzle ($\frac{A_e}{A^*} = 4$, $\theta_w = 15°$), using the products of hydrogen peroxide decomposition for the main nozzle flow. Various diameter injection ports were investigated, located in all cases at a nozzle area ratio of 2.6 ($M_1 = 2.34$). The injector was oriented normal to the nozzle axis. The following gaseous injectants were investigated: hydrogen, helium, helium-argon mixture, nitrogen, carbon dioxide and argon.

Newton and Spaid (ref. 4-8) have presented side force data, using freon 12, water and gaseous nitrogen. A solid propellant rocket, having a conical nozzle ($\frac{A_e}{A^*} = 25$, $\theta_w = 15°$), was used. Most of the data were obtained for injection at a nozzle area ratio of 8.81. Measurements were made of side force and of wall pressure distributions. Typical values of side force specific impulse were 45, 100 and 180 sec. respectively, for injection of water, freon 12 and nitrogen.

Green and McCullough (ref. 4-9) have made extensive measurements of the performance of liquid injectants, using both liquid propellant and solid propellant rockets. The following injectants were investigated:

- water
- freon 12
- perchloroethylene
- nitrogen tetroxide
- bromine
- UDMH-IRFNA (simultaneous injection)

Conical nozzles ($\frac{A_e}{A^*} = 8.15$, $\theta_w = 15°$) were used for all the experiments. The effect of axial location of the injector and the effect of injectant pressure were determined. The side force specific impulse (I_{sp_s}) varied from approximately 45 sec (water injection) to approximately 110 sec (bipropellant injection).

Generalization of experimental results - Based on the experimental studies, several generalizations can be made about the performance of SITVC:

1. For a constant injector area, the side force is approximately linear with injected mass flow for low rates of injection.
2. The performance decreases rapidly at high rates of injection because of cosine losses.
3. The effectiveness of the injectant is increased by increasing the injectant velocity (for a given injectant flow).
4. There is a "saturation effect" which causes the performance to decrease at very high flow rates. This effect is independent of the cosine losses.
5. Shock wave pressure decreases rapidly with distance downstream of injection, indicating that most of the side force is generated near the port.
6. Cosine losses limit performance for injection at low nozzle area ratios.
7. Side force is a weak function of the stream pressure, p_1, at the injection station.
8. The injectant momentum provides only about 10-30% of the total side force for liquid injectants, and about 50% for gaseous injectants.
9. The desired characteristics for a liquid injectant are (ref. 4-9): (a) low specific heat in liquid and vapor phases,

(b) low boiling point, (c) low heat of vaporization, (d) high heat of reaction or exothermic decomposition, (e) low molecular weight in gaseous phase and (f) high density in the liquid phases (for packaging).

10. The desired characteristics of a gaseous injectant are essentially those of a high performance rocket propellant: high temperature, low molecular weight, etc.

4.3 THEORETICAL ANALYSIS OF SECONDARY INJECTION THRUST VECTOR CONTROL

Zimmerman, et al (Ref. 4-10) have reviewed the various analytical approaches which have been proposed. The most detailed analyses consider the complex flow mechanisms near the injection port and are based on prediction of the equivalent blunt body formed by the injectant. Less detailed analyses have proven more useful for side force predictions. These semi-detailed analyses are based on (1) linearized theory, (2) the blast wave analogy, or (3) integration of the flow properties at the nozzle exit plane.

4.3.1 Blunt body analyses

Analysis of Wu, Chapkis and Mager - Wu, et al (ref. 4-11) used the blunt body analogy to analyze the case of gas injection. Their flow model is illustrated in the following sketch.

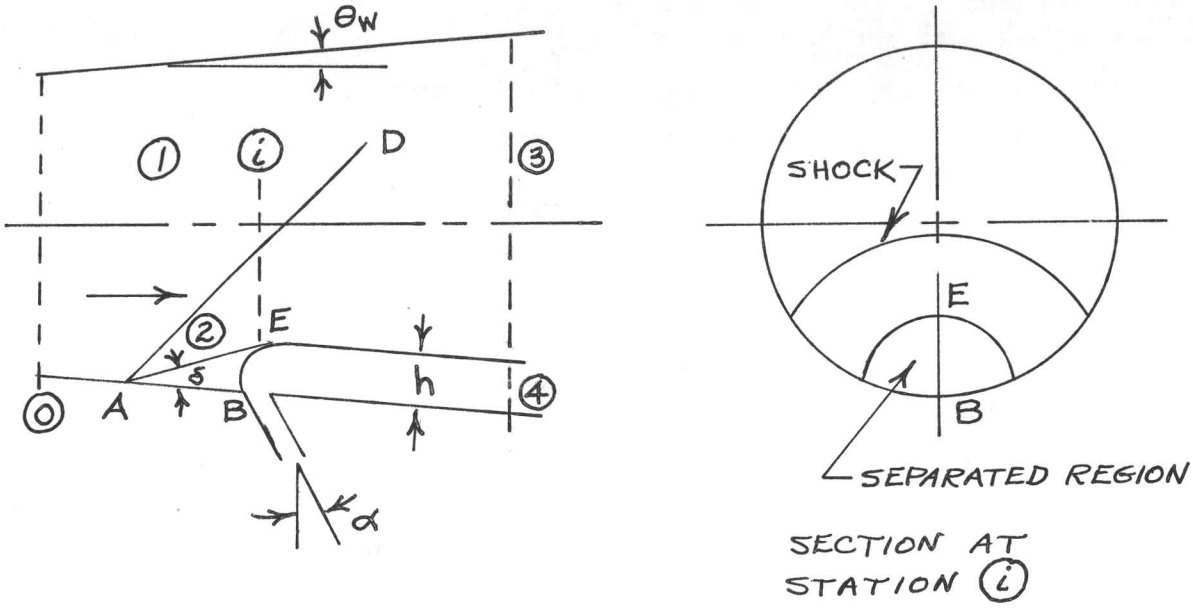

The nozzle is assumed to be cylindrical over the length involved ($\theta_w = 0$). The separation angle, δ, pressure, and separation shock angle are determined with the method of Mager (ref. 4-12). The length of the separated region can be determined in terms of h, the height of the equivalent solid body which is assumed to be semi-circular. Both streams are assumed one dimensional at sections 3 and 4, and conservation equations written from section 0 to sections 3 and 4 are used to solve for h. The separation region is assumed to be conical, with a conical separation shock. The distance from the shock vertex to the center of the injection port, X, is given by

$$X = h\left[\cot\delta+\tan(\theta_w+\alpha)\right] \qquad (4\text{-}1)$$

It is assumed that there is no side force contribution downstream of the port. The entire interaction force is given by the pressure forces acting on the region of the wall upstream of the port which is affected by the conical separation shock. After deriving the projected area of the shock on the wall, ΔA, and the mean pressure on the wall, $\bar{p}_2$, the side force is given by the following equation:

$$F_s = \left[\left(\frac{\bar{p}_2}{p_1} -1\right)(\Delta A - Xh)+\left(\frac{p_{sep}}{p_1} -1\right)\left(Xh - \frac{A_i}{2}\right)\right] p_1 \cos\theta_w$$

$$+p_1 A_i \cos\alpha\left(\frac{p_i}{p_1} -1\right)+w_i V_i \cos\alpha \qquad (4\text{-}2)$$

where A_i is the area of the injection port and
V_i is the injectant velocity.

The pressure $\bar{p}_2$ is given approximately by

$$\bar{p}_2 = p_{sep} - \frac{1}{3}(p_{sep} - p_2) \qquad (4\text{-}3)$$

The boundary layer separation characteristics define p_{sep}, δ and the shock configuration (ΔA).

Wu, et al. correlated the theory with a limited number of gas injection experimental data, and the theory was found to predict F_s within about 15%. The theoretical effect of variation of the parameters on I_{sps} is illustrated in fig. 4-2. Figure 4-2a shows the effect of varying M_1 with all other parameters

held constant. Fig. 4-2b shows the effect of the injected gas Mach number, M_i, for constant injected mass flow. The effect of varying M_i, while holding A_i constant, is shown in fig.4-2c. Fig. 4-2d illustrates the effect of M_1 on I_{sps}, with $p_i = p_{sep}$. The effect injectant molecular weight, $\mathcal{M}_i$, is shown in fig. 4-2e, for two values of the main stream specific heat ratio. The "magnification factor" is the ratio of side force to the momentum of the injectant. Finally, the effect of the injection angle, α, is shown in fig. 4-2f.

Fig. 4-2a indicates that it is desirable to inject at a low value of M_1, if the injectant parameters are held constant. This trend results from the assumption that the entire side force occurs upstream of the injection port, therefore, the cosine losses are ignored. Realizing this neglect, Wu et al, stated that the optimum port location would occur when the shock just reaches the centerline of the nozzle wall at the exit plane:

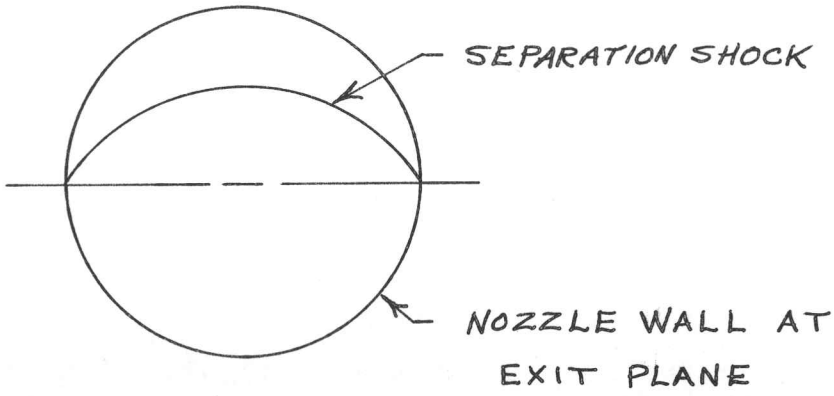

If the injectant pressure is correspondingly reduced, fig. 4-2d indicates that the most effective axial location for

injection is at the nozzle exit plane. Again, this conclusion results from ignoring the side force contribution downstream of the injection port.

Blunt body analysis of Zukowski and Spaid - Zukowski and Spaid (ref. 4-4) developed a blunt body analogy to correlate their data for single port injection into the supersonic flow past a flat plate.

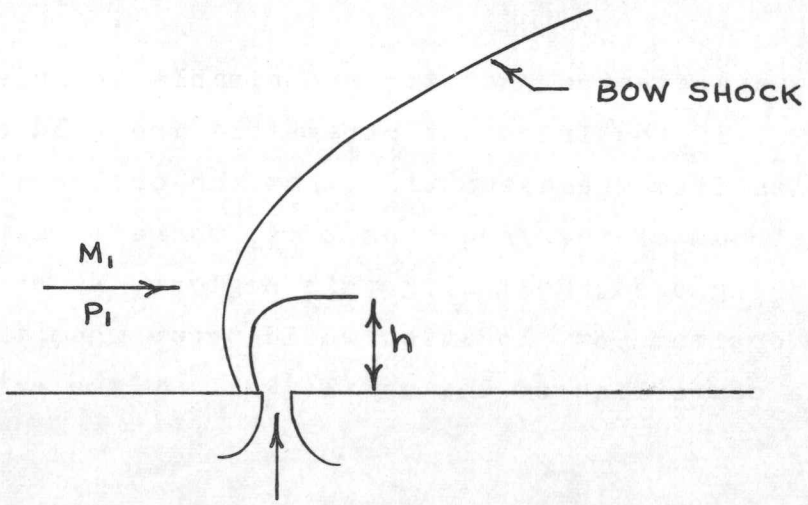

The following assumptions were made:

1. The injected jet is sonic
2. No mixing occurs near the injector
3. The equivalent body shape is a quarter sphere
4. The pressure forces on the sphere can be calculated by using Newtonian flow (as modified by Lees)
5. The injected flow expands isentropically to the ambient pressure at the downstream surface of the quarter sphere
6. Boundary layer interactions are negligible.

The modified Newtonian flow gives

$$\frac{C_p}{C_{po}} = \frac{\sin^2\theta}{\sin^2\theta_o}$$

where C_p is the pressure coefficient and θ is the local inclination angle of the body surface. C_{po} and θ_o are the values at the nose of the body ($\theta_o = 90°$). Normal shock relations determine C_{po} as a function of γ_1 and M_1, and the pressure distribution is defined. Integrating the pressure distribution over the spherical body yields the drag on the body. This drag is equated to the axial momentum imparted to the injected flow, yielding

$$\frac{h}{d_i} = \left[\left(\frac{1}{M_1}\right)\left(\frac{p_{oi}}{p_1}\frac{\gamma_i}{\gamma_1}\frac{2}{C_{po}}\right)^{\frac{1}{2}} \left\{ \frac{2}{\gamma_i - 1}\left(\frac{2}{\gamma_i+1}\right)^{\frac{\gamma_i+1}{\gamma_i-1}} \left[1-\left(\frac{p_1}{p_{oi}}\right)^{\frac{\gamma_i-1}{\gamma_i}} \right] \right\} \right]^{\frac{1}{4}} \tag{4-4}$$

where d_i is the effective diameter of the injectant port (the actual diameter of the flow coefficient is unity). Zukowski and Spaid noted that the term to the one-fourth power varies slowly, as does C_{po}, with γ_1 and M_1, so the following approximation was suggested

$$h \propto \frac{d_i}{M_1}\left(\frac{p_{oi}}{p_1}\right)^{\frac{1}{2}} \tag{4-5}$$

In terms of the injectant flow rate, w_i, eq. 4-5 can be written

$$h \propto \frac{1}{M_1}\left(\frac{w_i}{p_1}\right)^{\frac{1}{2}} \left(R_i T_{oi}\right)^{1/4} \tag{4-6}$$

Eqs. (4-5) and (4-6) are good approximations for $M_1 > 2$ and $\frac{p_1}{p_{oi}} << 1$.

Zukowski and Spaid show good agreement between eq. (4-4) and their experimental penetration heights, indicating that the approximate analysis does include the pertinent variables. The pressure distributions on the plate were found to correlate reasonably well with $\frac{x}{h}$, with h determined from eq. 4-4.

Zukowski and Spaid also used eq. (4-4) to develop a scaling law for injection into rocket nozzles. The following expression was obtained:

$$\frac{F_s}{F_{ax}} \propto \frac{w_i}{w_c}\left[\frac{T_{oi}}{T_{oc}}\frac{\mathcal{M}_c}{\mathcal{M}_i}\right]^{\frac{1}{2}} \qquad (4\text{-}7)$$

where the subscript c denotes the main rocket flow. Note that the dependence on $\mathcal{M}_i$ is the same as predicted by Wu, et al.

4.3.2 Linearized theory

Wu, Chapkis and Mager (ref. 4-11) used linearized theory for the case of liquid injection into rocket nozzles. It is assumed that the liquid turns immediately and flows along the nozzle wall.

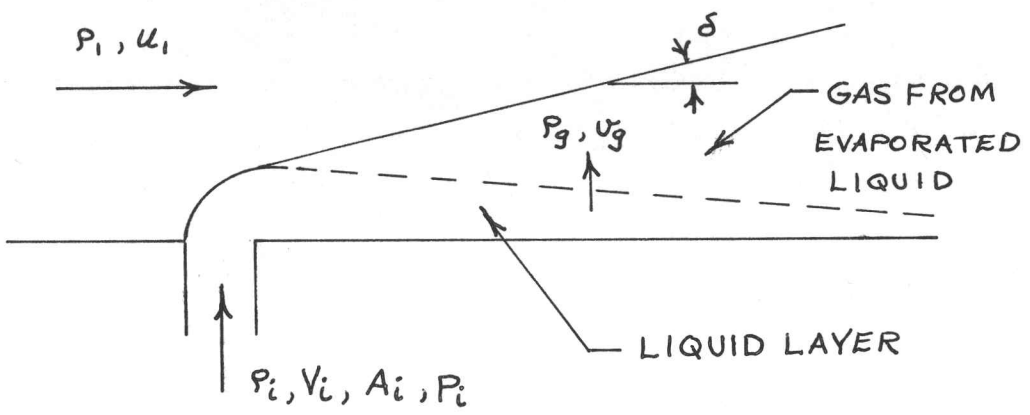

As the liquid evaporates, mass is assumed to enter the gas layer as though a uniform distribution of sources exists along the interface. The mass addition is

$$w_g = \rho_g v_g A_g$$

where A_g is the area of the gas-liquid interface. It is assumed that the rate of mass addition is low enough so that supersonic linearized theory applies, indicating that the distributed sources are equivalent to a wedge of half angle $\delta = v_w/u_1$. Wu, et al., show that the equivalent wedge upwash velocity, v_w, is approximately $\frac{\rho_g}{\rho_1} v_g$, and the force normal to the wall is found to be $(w_g u_1/\sqrt{M_1^2-1})$. Expressing the total side force in terms of the fraction of fluid evaporated, $\xi = w_g/w_i$, and the mass flow ratio, w_i/w_c:

$$F_s = \frac{2}{\sqrt{M_1^2-1}} q_1 \frac{\xi w_i}{w_c} \cos\theta_w + F_i \cos\alpha \qquad (4\text{-}8)$$

where $q_1 = \frac{1}{2} \rho_1 u_1^2$, α is the angle of the injection port, and F_i is the initial thrust of the injectant. For injection of liquids, $F_i << F_s$, therefore

$$F_s \simeq \frac{2}{\sqrt{M_1^2-1}} q_1 \frac{\xi w_i}{w_c} \cos\theta_w \qquad (4\text{-}9)$$

The ratio F_s/F_{ax} is plotted in fig. 4-3 for typical operating parameters. Holding ξ and w_i/w_c fixed, eq. (4-9) indicates that it is advantageous to inject at low Mach numbers. For example, injection at $M_1 = 3$ results in F_s being only about half as large as for injection at $M_1 = 1.4$.

The linearized theory can be extended to include the case of heat addition as well as mass addition. A heat source is equivalent to a fluid source, and the heat and mass fluxes are related by

$$\frac{(\gamma-1)Q}{c_1^2 A} = \frac{w}{A}$$

where c_1 is the free stream speed of sound. The additional upwash velocity caused by a total heat addition rate, Q, is

$$\left(\frac{v}{u_1}\right)_q = (\gamma_1-1) \frac{Q}{\rho_1 c_1^2 u_1 A_g}$$

The added side force caused by heat addition is

$$F_s\Big|_q = \frac{\gamma_1-1}{u_1} \frac{M_1^2}{\sqrt{M_1^2-1}} Q \cos\theta_w \qquad (4\text{-}10)$$

Wu, et al., correlated their linearized theory with limited experimental data for injection of water and freon 12. The water injection data correlated well with the assumption that $\xi = 0.35$. For freon 12 injected through the same size port $\xi = 0.54$ correlated the data. Doubling the experimental injection port area required $\xi = 0.76$ to correlate the data for freon 12, indicating that the evaporation rate is dependent on the detailed flow near the injection station.

The linearized theory should only be valid for low rates of injection. The primary disadvantage of the theory is that the evaporation factor, ξ, is dependent on the detailed flow mechanisms. Theoretical prediction of ξ would require detailed analysis of the mass transfer phenomena.

4.3.3 Blast wave analogy

Analysis of Broadwell - Broadwell (ref. 4-13) applied the blast wave analogy to the prediction of the side force caused by secondary injection. The blast wave analogy applies the solution for the unsteady cylindrical flow produced by the explosion of a line charge to the case of axisymmetric steady flow around a blunt body. Broadwell used the blast wave analogy to predict the pressure distribution behind the shock caused by the injectant, and thereby calculated the interaction force on the wall.

The radius, R, of the shock formed by the sudden release of energy, E, per unit length along a line may be written as a power series in terms of the inverse of the shock Mach number squared (ref. 4-14):

$$\left(\frac{c}{u}\right)^2 \left(\frac{R_o}{R}\right)^2 = J_o \left[1+\lambda_1\left(\frac{c}{u}\right)^2+\lambda_2\left(\frac{c}{u}\right)^4+ \ldots\right] \qquad (4\text{-}11)$$

where c is the speed of sound in the undisturbed gas and u is the shock velocity. R_o is a characteristic length defined by

$$R_o = \left(\frac{E}{2\pi p_1}\right)^{\frac{1}{2}} \qquad (4\text{-}12)$$

where p_1 is the undisturbed gas pressure.
The constants J_o and λ_1 in eq. 4-11 have been numerically evaluated by Sakurai for $\gamma_1 = 1.4$, but only J_o has been evaluated for other γ's. Broadwell used the first order theory $\left(\lambda_1\left(\frac{c}{u}\right)^2 << 1\right)$, and eq. 4-11 becomes

$$\left(\frac{c}{u}\right)^2\left(\frac{R_o}{R}\right)^2 = J_o \qquad (4\text{-}11a)$$

Sakurai gave the first order pressure distribution behind the shock as

$$\frac{p}{p_1}\left(\frac{c}{u}\right)^2 = g\left(\frac{r}{R}\right) \qquad (4\text{-}13)$$

Sakurai presented $g\left(\frac{r}{R}\right)$ for various values of γ.
Noting that $u = \frac{dR}{dt}$, eq. 4-11a may be integrated to yield

$$\frac{R}{R_o} = \sqrt{\frac{2ct}{R_o J_o^{\frac{1}{2}}}} \qquad (4\text{-}14)$$

We may transform the solution to the steady, axisymmetric case by making the substitution $t = \frac{x}{u_1}$:

$$R^* = \sqrt{\frac{2x^*}{J_o^{\frac{1}{2}} M_1}} \tag{4-15}$$

where $R^* = \frac{R}{R_o}$ and $x^* = \frac{x}{R_o}$.

Similarly

$$\frac{p}{p_1} = \tfrac{1}{2} \frac{\sqrt{J_o} M_1 g(\frac{r}{R})}{x^*} \tag{4-16}$$

By assuming that the energy was released along a flat plate, Broadwell deduced the following expression for the interaction force on the plate, F_w:

$$F_w = \frac{2E}{\pi} \left[\frac{1}{2^{\frac{1}{2}} J_o^{3/4}} \bar{g} \, M_1^{\frac{1}{2}} L^{*\frac{1}{2}} - \frac{2^{\frac{1}{2}}}{3 J_o^{1/4}} M_1^{-\frac{1}{2}} L^{*3/2} \right] \tag{4-17}$$

where $L^* = \frac{L}{R_o}$ and $\bar{g} = \int_o^1 g(\frac{r}{R}) d(\frac{r}{R})$. The value of $\bar{g}$ is always about $\frac{1}{2}$, independent of γ. The value of L is arbitrary, but not critical if the plate is sufficiently long.

The only remaining unknown is specification of E in terms of the fluid injection parameters. For hypersonic flow of a blunt body, E is set equal to the drag. In the case of fluid injection, the equivalent drag is that to accelerate the injected flow to free stream velocity, i.e. $w_i u_1$.

The energy is confined to the space above the wall, and

$$\frac{E}{2} = w_i u_1$$

Broadwell generalized the equivalent energy, E, to include the effect of volume addition. He assumed that the additional volume could be accounted for by finding the equivalent amount of heat which would cause the same volume change in a portion of the primary flow. The energy term becomes

$$E = w_i u_1 \left[1 + \frac{1 + \frac{\gamma_1 - 1}{2} M_1^2}{2(\gamma_1 - 1) M_1^2} \frac{\mathcal{M}_1}{\mathcal{M}_i} \frac{T_{oi}}{T_{o1}} \right] \qquad (4\text{-}18)$$

Broadwell took L* to be that which gives the maximum F_w, and obtained the following expression for F_w:

$$F_w = C\sigma M_1 u_1 \left[1 + \frac{2 + (\gamma_1 - 1) M_1^2}{2(\gamma - 1) M_1^2} \frac{\mathcal{M}_1}{\mathcal{M}_i} \frac{T_{oi}}{T_{o1}} \right] w_i \qquad (4\text{-}19)$$

where $\sigma = \dfrac{2\overline{g}^{3/2}}{3\pi J_o}$ $\begin{cases} \sigma = 0.10 & \text{for } \gamma_1 = 1.2 \\ \sigma = 0.17 & \text{for } \gamma_1 = 1.4 \end{cases}$

Because of the approximate nature of the theory, the constant C was included, and was determined from experiments. Broadwell correlated the data of Amick and Hays and found that $C \simeq 1.2$.

Applying the results to the case of a rocket nozzle, where the wall is not parallel to the axis, and including the

the initial jet thrust:

$$F_s = C\sigma M_1 u_1 \left[1+ \frac{2+(\gamma_1-1)M_1^2}{2(\gamma_1-1)M_1^2} \frac{\mathcal{M}_1}{\mathcal{M}_i} \frac{T_{oi}}{T_{o1}} \right] w_i \cos\theta_w + F_i \cos\alpha \qquad (4\text{-}20)$$

where F_i is the initial jet thrust and α is the inclination of the injectant port with respect to a normal to the nozzle centerline (section 4.3.1).

The increment of axial thrust caused by secondary injection, ΔF_{ax}, is given by

$$\Delta F_{ax} = C\sigma M_1 u_1 \left[1+ \frac{2+(\gamma_1-1)M_1^2}{2(\gamma_1-1)M_1^2} \frac{\mathcal{M}_1}{\mathcal{M}_i} \frac{T_{oi}}{T_{o1}} \right] w_i \sin\theta_w - F_i \sin\alpha \qquad (4\text{-}21)$$

Broadwell correlated his blast wave analysis with some of the cold flow experiments of Rodriguez (ref. 4-6). The nozzle area ratio, A_e/A^*, was 25 with injection at nozzle area ratios of 12.8 and 17.1. The results for injection at $\left.\frac{A}{A^*}\right|_i = 12.8$ are shown in fig. 4-4. The theory accurately predicts the side force only at very low injection rates, indicating that cosine losses become important at the higher flow rates. Cosine losses do not affect the axial thrust increment, and the theory accurately predicts ΔF_{ax} (fig. 4-4b). Neither side force nor axial thrust increment is accurately predicted for injection at a nozzle area ratio of 17.1, indicating that there was insufficient nozzle length downstream of the injector for the maximum interaction force to be developed.

Broadwell (ref. 4-15) also correlated his blast wave theory with the experiments of Walker, et al. (ref. 4-7) who used various gaseous injectants. The results for the side force F_s, (shown in fig. 4-5) indicate that the blast wave theory predicts with reasonable accuracy the effect of injectant gas molecular weight.

There is conflicting evidence on the effect of injectant molecular weight on side force. The theoretical results of Zukowski and Spaid, and of Wu, et al., indicate that F_s is inversely proportional to $\sqrt{\mathcal{M}_i}$. Several experimental investigations verify this dependence on $\mathcal{M}_i$. The blast wave theory, and the experimental results of Walker, et al., indicate that only the initial injectant thrust is inversely proportional to $\sqrt{\mathcal{M}_i}$, with the interaction force, F_w, being inversely proportional to $\mathcal{M}_i$.

Broadwell (ref. 4-13) extended his blast wave theory to the case of liquid injection. The fluid is assumed to vaporize immediately upon injection. Broadwell correlated his theory with the freon 12 injection experiments of Newton and Spaid (ref. 4-8). The results, shown in fig. 4-6, indicate that the blast wave theory is reasonably accurate for freon 12 injection. For fluids, such as water, which do not flash vaporize, it is not likely that the blast wave theory would be sufficient.

Analysis of Dahm - Dahm (ref. 4-16) also applied the blast wave analogy to SITVC. His theoretical development is similar to Broadwell's, except for the following:

1. The length, L, downstream of the injectant port is taken as the actual distance to the nozzle exit plane.
2. The second order blast wave results are used in an approximate manner.
3. A different method is used to calculate the equivalent energy E.

Like Broadwell, Dahm included an empirical constant, C, in his side force equation. Dahm obtained somewhat better correlation with the data of Walker, et al., than did Broadwell.

Dahm did not treat the case of liquid injection.

4.3.4 Integral analysis of thrust vector control

Karamcheti and Hsia (ref. 4-17) proposed an analysis of SITVC based on an integration of the flow properties at the nozzle exit plane. The analysis considers the overall changes in mass flow, momentum and energy in the portion of the nozzle flow disturbed by the injection process. At the exit plane:

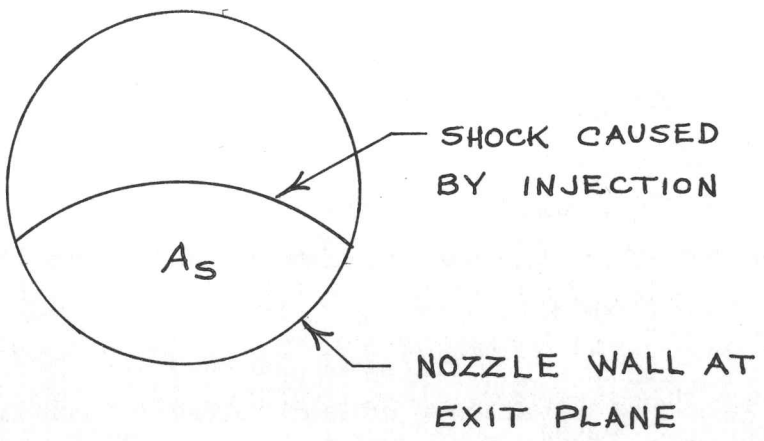

For an injectant which is a perfect gas, Karamcheti and Hsia assumed that the flow conditions over A_s are uniform, and obtained the following equation for F_s:

$$F_s = -(w_i+w_1 \frac{A_s}{A_e})+\left\{2(w_i+w_1 \frac{A_s}{A_e})(\frac{w_i}{w_1}\frac{h_i}{u_e^2}+\frac{h_1}{u_e^2}\frac{A_s}{A_e} - \frac{c_{ps}\mathcal{M}_s}{R}\frac{p_s}{w_1}\frac{A_s}{u_e}\right\} \tag{4-22}$$

where the subscript s refers to the region of disturbed flow (except for the side force, F_s). The subscript 1 refers to the flow approaching the injection station, and e to the undisturbed nozzle exit conditions. Equation 4-22 contains two unknowns, p_s and A_s. Karamcheti and Hsia used first order blast wave theory, as developed by Broadwell, to determine the shape of the shock at the nozzle exit plane. The unknown pressure, p_s, was written in terms of the axial thrust increment, ΔF_{ax}, as

$$\Delta F_{ax} \simeq (p_s-p_e)A_s + w_i u_e \tag{4-23}$$

If ΔF_{ax} is known, eqs. 4-22 and 4-23 define the side force F_s.

Karamcheti and Hsia found that, using the experimental values of ΔF_{ax}, the analysis accurately predicts F_s for the case of injection well upstream of the nozzle exit. For injection close to the nozzle exit plane, poor correlation was obtained, indicating that the assumption of uniform flow over A_s is in error.

The advantage of the integral analysis is that it implicitly includes the cosine losses, and the analysis predicts

the experimental fact that the curve of F_s vs w_i levels off at high values of w_i. There is need of additional work on the prediction of p_s, to eliminate the dependence on experimental values of ΔF_{ax}. The value of the analysis for prediction of liquid injection performance has not yet been determined.

4.3.5 Experiments on the shape of the injection shock

Hsia, et al., (ref. 4-18) presented experimental results on the shape of the injection shock. The nozzle was two dimensional, with nitrogen used as the working fluid. Gaseous nitrogen, liquid nitrogen and freon 12 were used for the injectant ($2.2 < M_1 < 3.2$). The results indicate that the first order blast wave solution is inadequate except for a short distance downstream from the injection port. Second order blast wave theory was found to predict the shock shape if the shock axis was assumed to be parallel to the nozzle axis rather than parallel to the wall.

Evers (ref. 4-19) presented experimental results on the shock shape caused by sonic injection of air through a circular orifice in a flat plate. The free stream Mach number was varied from 2.2 to 7. Evers found that second order blast wave theory, incorporating the equivalent energy term of Dahm, accurately predicts the shock shape if an origin shift is taken into account. The vertical origin shift was found to vary from 1 to 8 times the boundary layer thickness just upstream of the port, depending on the free stream Mach number and injection pressure ratio. The axial origin shift was found to be related to the radius of the equivalent blunt body, and

to be only weakly dependent on the free stream Mach number. The plate boundary layer was laminar for all operating conditions.

4.3.6 Summary of analytical methods

Because of their simplicity, the blast wave analogies of Broadwell and Dahm appear to be the most useful for gaseous injectants, or for liquid injectants which flash vaporize. At present, these analyses are limited to low rates of injection because the cosine losses are neglected. Zimmerman, et al.,(ref 4-10) used first order blast wave theory to develop an approximate relation for the cosine losses. By incorporating this relation, the SITVC analyses of Broadwell and Dahm could be extended to higher injection rates.

No analytical technique appears to be completely adequate for the injection of liquids which evaporate slowly, or for injectants which react with the main flow. Sehgal and Wu (ref. 4-20) developed a technique for calculating the effective blunt body caused by the evaporation of a liquid injectant. The complex processes of droplet formation, droplet trajectories and evaporation were treated in a highly simplified way. The general usefulness of the technique has not yet been established.

Throughout the chapter it has been assumed that the injectant is introduced through a single circular port. Wu, et al., (ref. 4-11) investigated the case of gas injection through a slot into a two dimensional flow, and found that this configuration yields a higher side force than does a single port. Broadwell (ref. 4-13) also treated the case of slot injection into two dimensional flow. He found that the side force is

about three times higher than for a circular port. A transverse slot configuration might offer some advantage in a rocket nozzle, but would tend to increase the sosine losses. A more practical configuration from a structural viewpoint would be a transverse array of circular ports. Hozaki, et al. (ref. 4-21) have investigated the interaction caused by a transverse array of circular holes.

REFERENCES

4-1 HAUSMANN: Thrust axis control of supersonic nozzles by airjet shock interference.
United Aircraft Corp., Rep. R-63143-24, May 1952.

4-2 HOLLSTEIN: Jet tab thrust vector control.
Jnl of Spacecraft & Rockets, vol. 2, n° 6,
November-December 1965, pp. 927-930.

4-3 AMICK & HAYS: Interaction effects of side jets issuing from flat plates and cylinders aligned with a supersonic stream.
WADD TR n° 60-329, June 1960.

4-4 ZUKOWSKI & SPAID: Secondary injection of gases into supersonic flow.
AIAA Jnl, vol. 2, n° 10, October 1964, pp. 1689-1696.

4-5 BANKSTON & BARNES: Thrust vectoring: shock wave and pressure effects of cold air injection into a two dimensional nozzle.
NOTS TP 2608 (AD 267 465), January 1961.

4-6 RODRIGUEZ: An experimental investigation of jet induced thrust vector control methods.
Bull. 17th Annual JANAF-ARPA-NASA Solid Propellant Meeting, vol. III, JHU/APL, pp 77-122, May 1961.

4-7 WALKER, STONE & SHANDOR: Secondary gas injection in a conical rocket nozzle.
AIAA Jnl, vol. 1, n° 2, Febr. 1963, pp 334-338.

4-8 NEWTON & SPAID: Interaction of secondary injectants and rocket exhaust for thrust vector control.
ARS Jnl, vol. 32, n° 8, August 1962, pp 1203-1211.

4-9 GREEN & McCULLOUGH: Liquid injection thrust vector control.
AIAA Jnl, vol. 1, n° 3, March 1963, pp 573-578.

4-10 ZIMMERMAN, STARRET & VELLINGA: Secondary injection thrust vector control.
AD 613 689.

4-11 WU, CHAPKIS & MAGER: Approximate analysis of thrust vector control by fluid injection.
ARS Jnl, vol. 31, n° 12, December 1961, pp 1677-1685.

4-12 MAGER: On the model of the free shock-separated turbulent boundary layer.
Jnl Aero. Sc. vol. 23, n° 2, Febr. 1956, pp 181-184.

4-13 BROADWELL: Analysis of the fluid mechanics of secondary injection for thrust vector control.
AIAA Jnl, vol. 1, n° 5, May 1963, pp 1067-1075.

4-14 SAKURAI: On the propagation and structure of the blast wave.
Part I: Jnl Physical Soc. Japan, vol. 8, 1953 pp 662-669
Part II: Jnl Physical Soc. Japan, vol. 9, 1954 pp 256-266

4-15 BROADWELL: Correlation of rocket nozzle gas injection data.
AIAA Jnl, vol. 1, n° 8, August 1963, pp 1911-1913.

4-16 DAHM: The development of an analogy to blast wave theory for the prediction of interaction forces associated with gaseous secondary injection into a supersonic stream.
VIDYA TN 9166-TN-3, May 1964. (AD 450 743).

4-17 KARAMCHETI & HSIA: Integral approach to an approximate analysis of thrust vector control by secondary injection.
AIAA Jnl, vol. 1, n° 11, November 1963, pp 2538-2544.

4-18 HSIA, SEIFERT & KARAMCHETI: Shocks induced by secondary fluid injection.
Jnl Spacecraft & Rockets, vol.2, n° 1, January-February 1965, pp 67-72.

4-19 EVERS: A study of the bow shock induced by secondary injection into supersonic and hypersonic flows.
von Karman Institute for Fluid Dynamics, Project Report 65-127, June 1965 (also VKI TN 29).

4-20 SEHGAL & WU: Thrust vector control by liquid injection into rocket nozzles.
Jnl Spacecraft & Rockets, vol. 1, n° 5, September-October 1964, pp 545-551.

4-21 HOZAKI, et al.: Investigation of boundary layer parameters in APG nozzle and the flow interference caused by secondary injection.
National Engineering Science Co, SN-101, 1963.

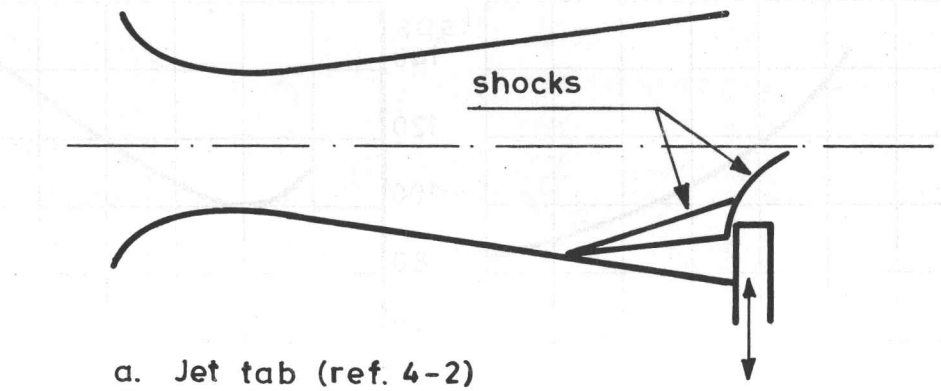

a. Jet tab (ref. 4-2)

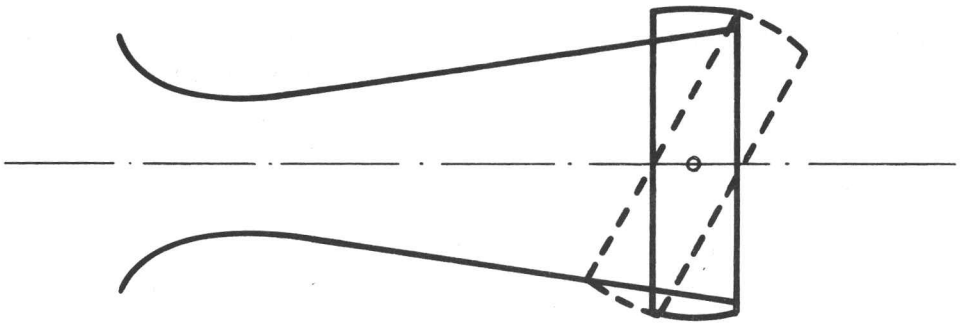

b. Jetavator

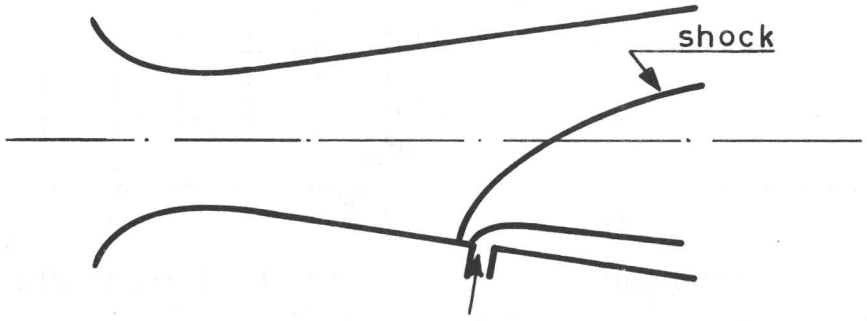

c. Secondary fluid injection

Fig. 4-1 METHODS OF THRUST VECTOR CONTROL

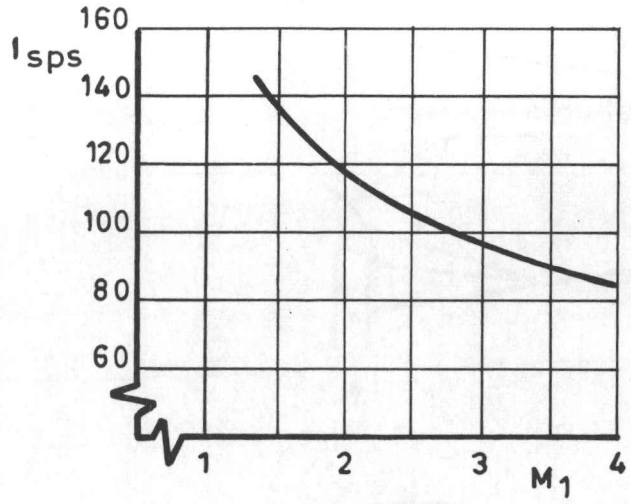

a. Effect of free stream Mach number (other parameters constant)

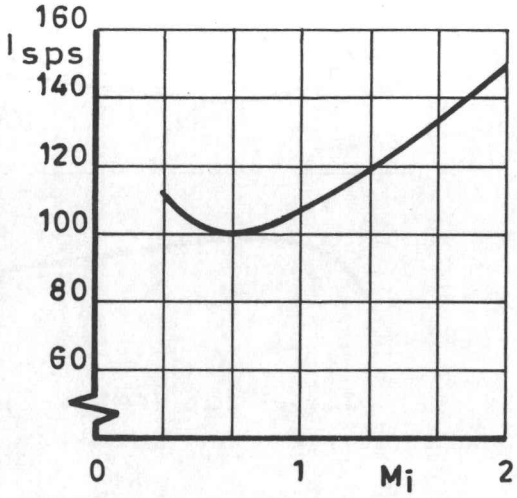

b. Effect of injectant Mach number (w_i constant)

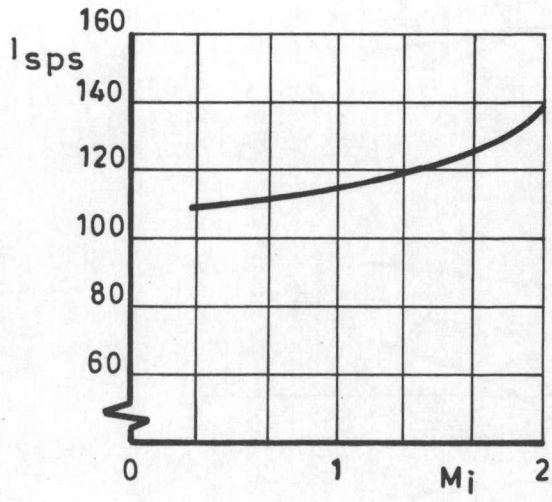

c. Effect of injectant Mach number (A_i constant)

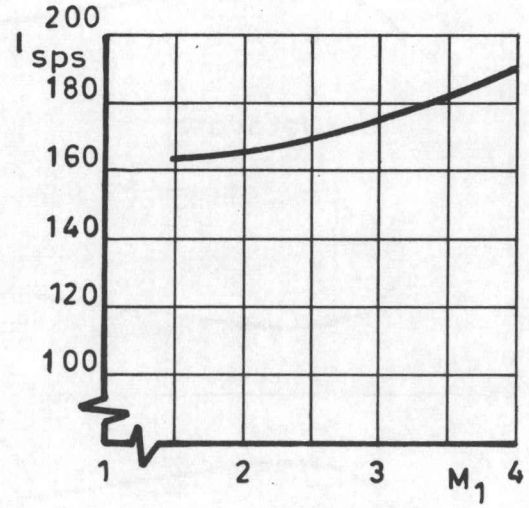

d. Effect of free stream Mach number ($P_i = P_{sep}$)

Fig. 4-2 EFFECT OF PARAMETERS ON GASEOUS SECONDARY INJECTION THRUST VECTOR CONTROL (ref. 4-11)

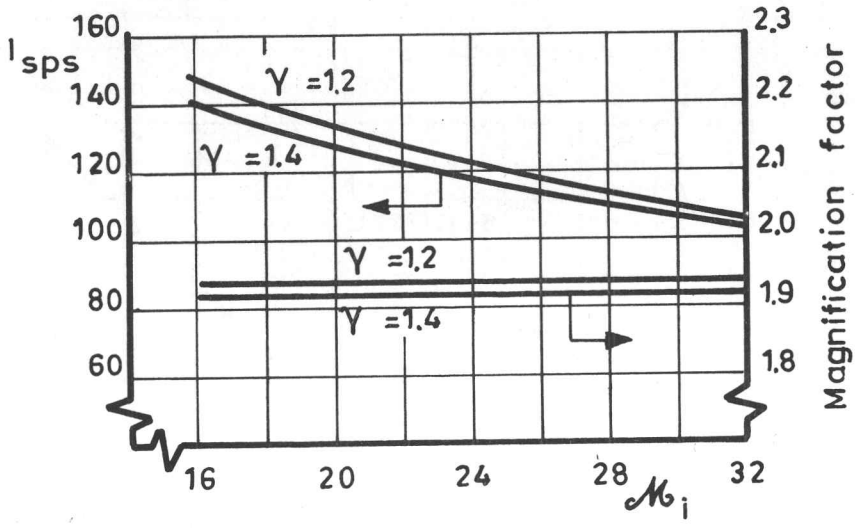

e. Effect of injectant molecular weight

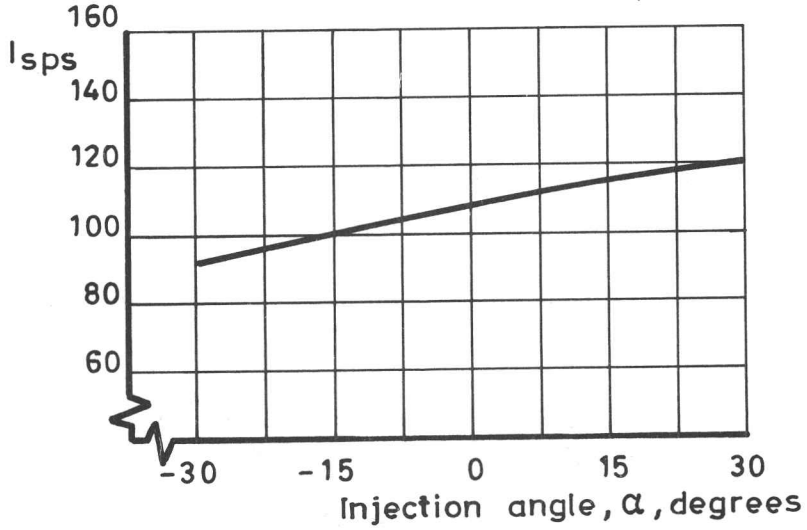

f. Effect of injectant angle

Fig. 4 - 2 (continued)

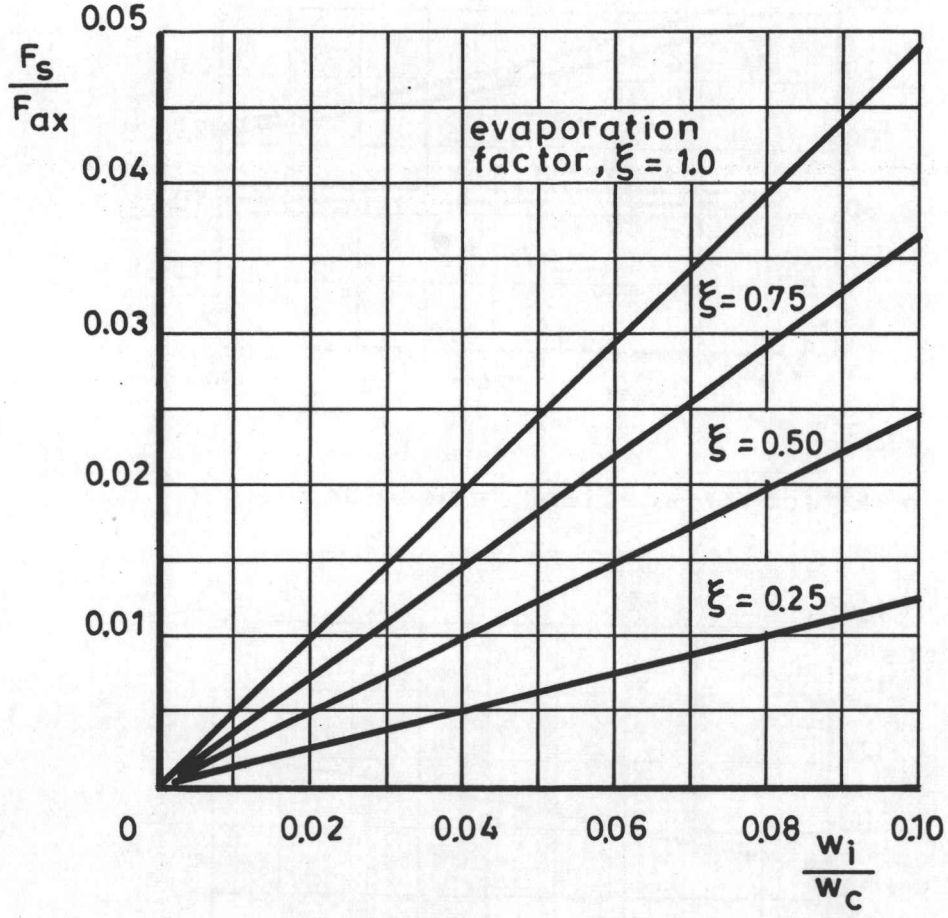

Fig. 4 - 3 LIQUID INJECTION SIDE FORCE PREDICTED BY LINEARIZED THEORY (ref. 4 - 11)

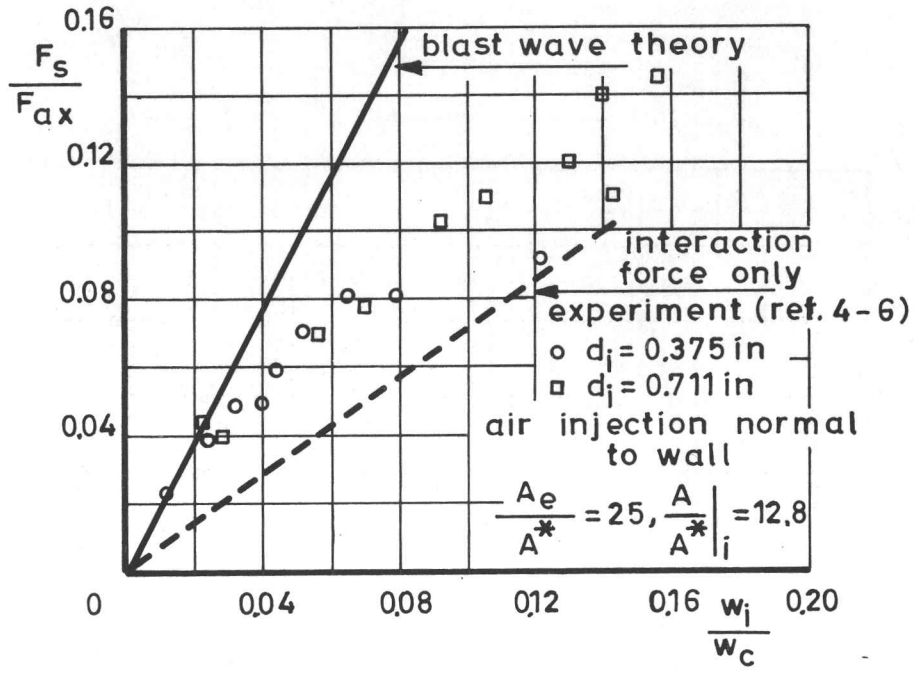

a. Side force

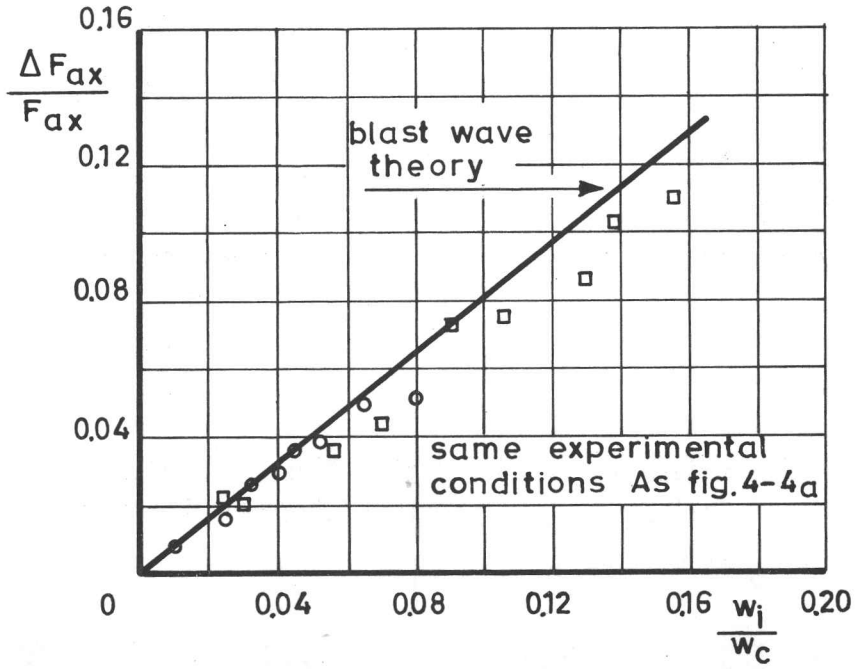

b. Axial thrust increment

Fig. 4-4 CORRELATION OF BLAST WAVE THEORY WITH GASEOUS INJECTION EXPERIMENTS (ref. 4-13)

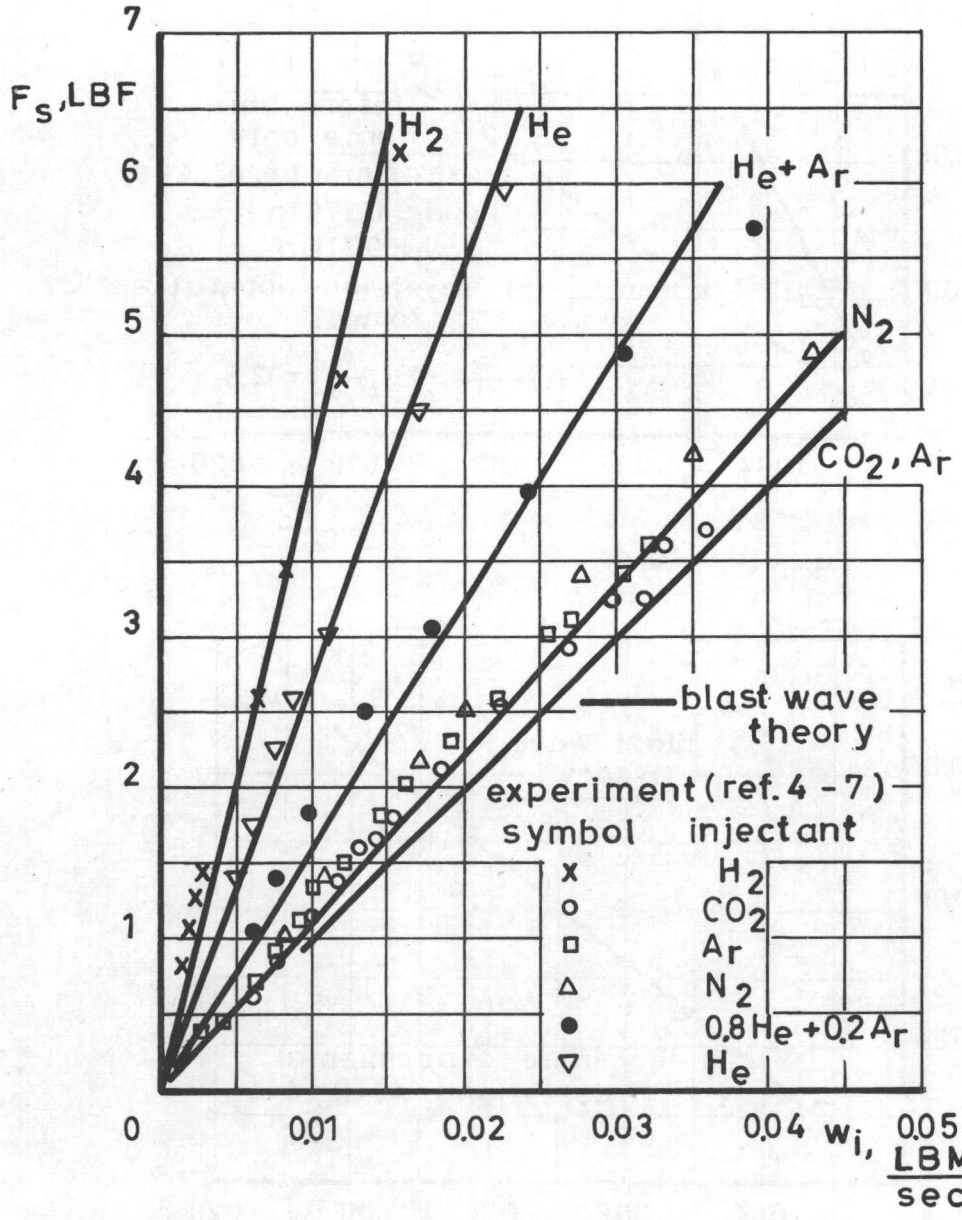

Fig. 4-5 CORRELATION OF BLAST WAVE THEORY WITH GASEOUS INJECTION EXPERIMENTS (ref. 4-15)

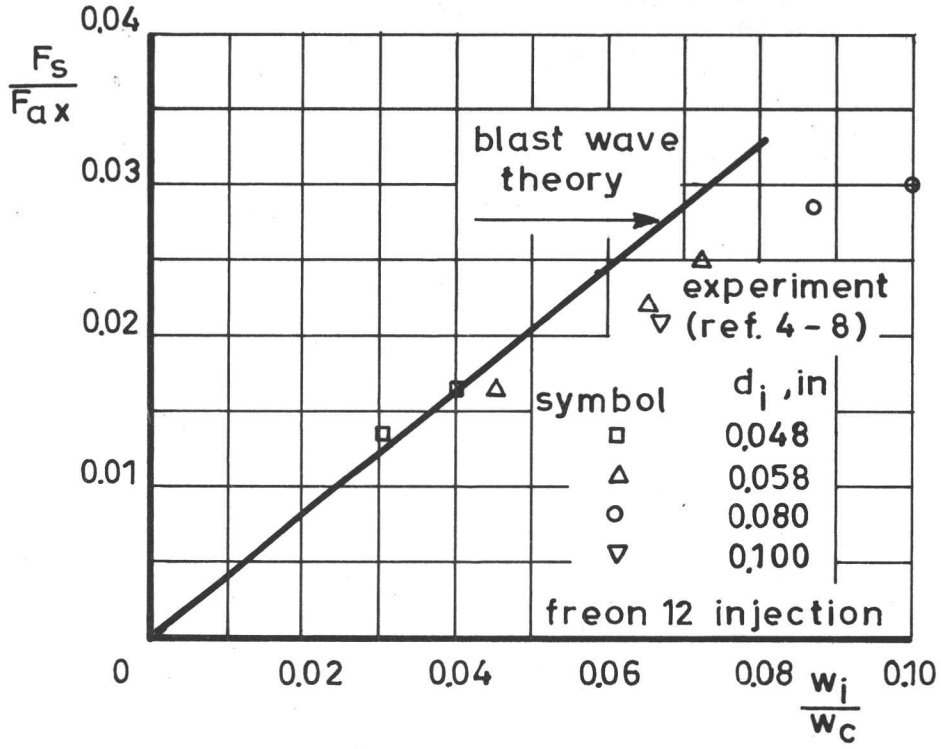

Fig. 4 - 6 CORRELATION OF BLAST WAVE THEORY WITH LIQUID INJECTION EXPERIMENTS (ref. 4 - 13)

CHAPTER 5

ADVANCED ROCKET NOZZLE CONCEPTS

5.1 CURRENT DESIGN TRENDS

High and low chamber pressure engines - Most operational liquid propellant rocket engines operate with chamber pressures in the range of 10 to 70 atm. There is currently considerable interest in liquid propellant engines which operate at very high chamber pressures (greater than 200 atm.). The high chamber pressure engines are attractive for several reasons. First, the high chamber pressure engine is relatively compact for a given thrust level. As the chamber pressure is increased, the amount of chemical dissociation in the chamber is decreased, resulting in higher c*. The higher pressure levels throughout the nozzle are conducive to attaining chemical equilibrium during the expansion process. From the viewpoint of the nozzle designer, the high chamber pressure is attractive because high area ratio nozzles may be used without incurring boundary layer separation at sea level. The improved nozzle performance resulting from use of high chamber pressure is illustrated in fig. 5-1, where the idealized one dimensional nozzle performance is compared for engines having p_c = 200 atm. and p_c = 40 atm. Both nozzles are designed for p_e = 0.5 atm. The thrust coefficient, C_F, is 7-15% higher for the high pressure engine over the altitude range shown in fig. 5-1a. The performance of the high area ratio nozzle is also closer to ideal over the entire altitude range (fig. 5-1b). The major practical difficulty in the use of high chamber pressures is the very high rate of heat transfer to the nozzle walls in the region of the throat.

At the other extreme, very low chamber pressure engines ($p_c \approx 1$ atm.) are of interest for space applications. The primary advantage of the low chamber pressure engine is that the structure may be effectively cooled by radiation, or by other simple cooling techniques (refs. 5-1 and 5-2). From the viewpoint of the nozzle designer, the major problem will probably be the large viscous effects in the nozzle.

Clustered rockets - With each succeeding generation of booster vehicles requiring greater total thrust, the clustering together of a number of well developed engines offers several advantages. One basic engine design can be incorporated into a variety of vehicles, resulting in increased reliability, decreased development time and decreased development costs. The clustering concept has, of course, already been applied to the Saturn series of boosters. An incidental advantage of clustering, which may be important in some applications, is that the overall vehicle length is less than the length for a single large engine.

The interaction of the individual exhaust jets with the external stream and with each other may result in an intense recirculation flow in the missile base region. The recirculation of the hot exhaust gases can cause severe heating of the missile base. Experiments and theory show that the base recirculation problem can be extremely serious when the nozzles are arranged in a circular pattern (ref. 5-3).

Plug-cluster nozzle - Mulready, et al. (ref. 5-4), have discussed the concept of the plug-cluster exhaust nozzle. The plug-cluster engine consists of a series of high pressure

engines arranged in a tight circular cluster about a truncated plug (fig. 5-2). The individual engine nozzles are of low area ratio and are tilted toward the plug axis. Mulready, et al., show experimental cold flow data which indicate that the performance of a plug-cluster nozzle with tightly spaced nozzles is similar to the performance of an annular plug nozzle. The plug-cluster nozzle appears to offer the advantages of clustering along with the altitude-compensating feature of the annular plug nozzle.

5.2 AIR AUGMENTED ROCKET-OVERALL ANALYSIS

The usual rocket engine operates fuel rich, therefore, substantial amounts of unburned or partially burned fuel are contained in the exhaust stream. During atmospheric flight of the rocket, it would be possible to capture free stream air and to direct it around the fuel rich exhaust jet. The resulting mixing and burning of the two streams inside a duct could result in a net improvement in the propulsive performance of the vehicle.

The concept of a combination rocket-air breathing propulsion system is hardly new; the ramrocket (fig. 5-3a) has received sporadic attention for the past 15 or 20 years. The main features of the ramrocket are:

(1) a small rocket which is operated with excess fuel,
(2) a cylindrical mixing section, and
(3) an aft nozzle.

The rocket and air streams mix and burn in the mixing section, with subsonic flow at the downstream end of the mixing section, and are subsequently accelerated in the aft nozzle. Based on

the extensive analytical results of Glassman and Charyk (ref. 5-5), the ramrocket would appear to be applicable to a high subsonic Mach number mission where a powerplant of high thrust per unit cross sectional area is desired. The classical ramrocket is basically an extension of the ramjet, with little of the total thrust being contributed directly by the rocket. Typically, the ratio of air flow to rocket flow is 10 to 30.

More recently, the concept of the air augmented rocket has received considerable attention. The air augmented rocket (fig. 5-3b) falls closer to the rocket side of the powerplant spectrum, with most of the thrust originating from the rocket. The primary features of the air augmented rocket, which distinguish it from the ramrocket, are:

1. It is designed primarily for the supersonic flight regime.
2. The mixing and burning occurs in a divergent mixing section, with no aft nozzle.
3. The ratio of air flow to rocket flow is less than 5.

In contrast to the ramrocket, the rocket stream may remain supersonic throughout the duct.

<u>One dimensional analysis of the air augmented rocket</u> - Perini, Walker and Dugger (ref. 5-6) have analyzed the performance of the air augmented rocket, using the assumption of one dimensional flow. The flow model is shown in the following sketch.

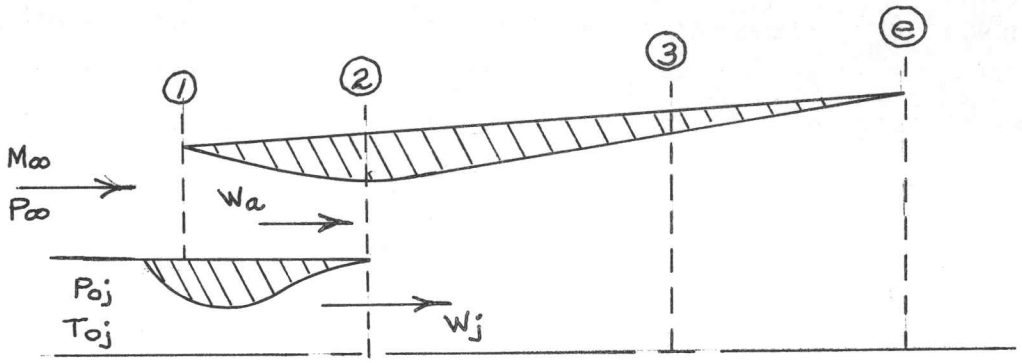

The following assumptions are made in the analysis:

1. The flow is one dimensional at all stations.
2. The air flow (subscript a) diffuses isentropically from free stream conditions to section 2a.
3. $P_{a2} = P_{j2}$.
4. The two streams mix and burn at constant pressure between sections 2 and 3.
5. The flow expands, in chemical equilibrium, from station 3 to a prescribed p_e.
6. Frictional effects are neglected.
7. Mixing duct weight and external drag are not considered.

The equations for the process 2-3 are:

Continuity:

$$\rho_{a2} u_{a2} A_{a2} + \rho_{j2} u_{j2} A_{j2} = \rho_3 u_3 A_3 \qquad (5\text{-}1)$$

Momentum (constant pressure)

$$\rho_{a2} u_{a2}^2 A_{a2} + \rho_{j2} u_{j2}^2 A_{j2} = \rho_3 u_3^2 A_3 \qquad (5\text{-}2)$$

Energy

$$\rho_{a2} u_{a2} H_{a2} + \rho_{j2} u_{j2} H_{j2} = \rho_3 u_3 H_3 \qquad (5\text{-}3)$$

where H is the total enthalpy, including heats of formation. Equations (5-1)-(5-3), along with the assumption of equilibrium chemistry, define the flow properties at station 3. The mixture is then expanded in chemical equilibrium to p_e, thus defining u_e.

The specific impulse is defined as

$$I_{sp} = \frac{F_{aug}}{w_j g_o} \qquad (5\text{-}4)$$

where

$$F_{aug} = (p_e A_e + w_e u_e) - (p_\infty A_{1a} + w_a u_\infty) - p_\infty (A_e - A_{1a}) \qquad (5\text{-}5)$$

Perini, et al., made an extensive series of calculations for the following conditions:

Free stream: $M_\infty = 3$

altitude = 40 000ft

$p_\infty = 2.7$ psia

$p_{o\infty} = 100$ psia.

Rocket: aluminized solid propellant

p_{oj} = 1 000 psia

T_{oj} = 4 150°K

Fraction of solids in rocket exhaust $\cong$ 47%

(particle lag effects neglected).

The effect of the following parameters was investigated: p_{a2}, p_e, and w_a/w_j. The system performance was found to be strongly dependent on the pressure at which the mixing and combustion takes place (fig. 5-4a), with the best performance being attained when the air is introduced at the highest possible pressure (therefore at a low subsonic Mach number). As in the case of a conventional rocket, it is desirable to expand the flow to the ambient pressure (fig. 5-4b).

Perini, et al. also analyzed in an approximate way the effect of diffuser inefficiency and the effect of incomplete mixing on the performance. Decreasing the diffuser kinetic energy efficiency from 1.0 to 0.95 reduced the I_{sp} approximately 8%. The approximate model indicated that the performance defect caused by incomplete mixing is not extremely serious.

The one dimensional analysis of the air augmented rocket, although very idealized, does point out the inherent potential of the concept. The duct shape required to realize the assumed pressure distribution cannot be predicted by the one dimensional theory, and information on the duct shape is required to evaluate the weight of the duct and the external drag on the duct. Realistic evaluation and optimization of the air augmented rocket requires a perceptive theory for the complex flow processes occuring within the mixing duct.

5.3 DETAILED ANALYSIS OF THE FLOW IN THE MIXING DUCT

The flow in the mixing duct is shown schematically in the following sketch:

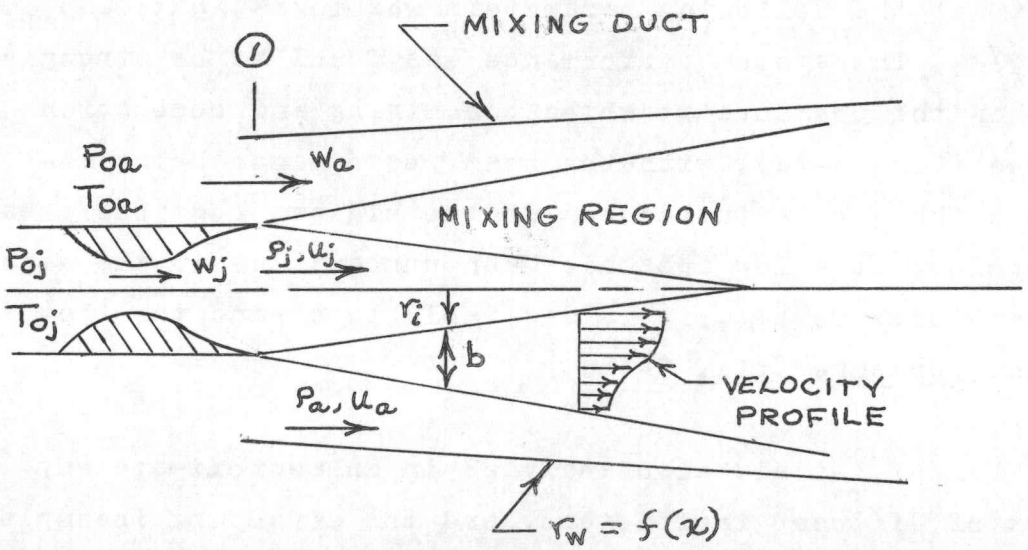

Analysis of the free turbulent mixing with chemical reactions is not only of interest for the air augmented rocket, but is also required for evaluation of the supersonic combustion ramjet. The mixing zone is essentially a high speed turbulent diffusion flame.

Analysis of turbulent mixing processes - Engineering analysis of free turbulent mixing processes is necessarily semi-empirical in nature because no fundamental quantitative flow model of turbulence has yet been derived. Free turbulent processes are usually analyzed by making the following assumptions:

1. The time average flow is treated with the boundary layer assumptions, using phenomenological, or effective, values

for the transport coefficients.

2. The molecular transport is negligible compared to the turbulent transport.

The boundary layer equations in axisymmetric coordinates are:

Global continuity:

$$\frac{\partial}{\partial x}(\rho u) + \frac{1}{r}\frac{\partial}{\partial r}(\rho v r) = 0 \qquad (5\text{-}6)$$

Axial momentum:

$$\rho u \frac{\partial u}{\partial x} + \rho v \frac{\partial u}{\partial r} = \frac{1}{r}\frac{\partial}{\partial r}\left(\rho \varepsilon r \frac{\partial u}{\partial r}\right) - \frac{\partial p}{\partial x} \qquad (5\text{-}7)$$

where ε is the turbulent eddy viscosity.

Energy

$$\rho u \frac{\partial H}{\partial x} + \rho v \frac{\partial H}{\partial r} + \frac{1}{r}\left[\frac{\rho \varepsilon}{Pr} r \frac{\partial H}{\partial r} + \frac{(Pr-1)}{Pr} \rho \varepsilon r u \frac{\partial u}{\partial r}\right.$$

$$\left. + \frac{(Le-1)}{Pr} \rho \varepsilon r \sum_{i=1}^{n} h_i \frac{\partial Y_i}{\partial r}\right] \qquad (5\text{-}8)$$

where H is the stagnation enthalpy (including heats of formation),

Y_i is the mass concentration of species i,

h_i is the static enthalpy of species i, and

the Prandtl and Lewis numbers are the effective turbulent values.

Species continuity

$$\rho u \frac{\partial Y_i}{\partial x} + \rho v \frac{\partial Y_i}{\partial r} = \frac{1}{r}\frac{\partial}{\partial r}\left(\frac{Le}{Pr} \rho \varepsilon r \frac{\partial Y_i}{\partial r}\right) + \dot{w}_i \qquad (5\text{-}9)$$

where $\dot{w}_i$ is the rate of chemical formation of species i.

These energy and species continuity equations may be considerably simplified by assuming that the Prandtl and Lewis numbers are unity.

$$\rho u \frac{\partial H}{\partial x} + \rho v \frac{\partial H}{\partial r} = \frac{1}{r} \frac{\partial}{\partial r} \left(\rho \varepsilon r \frac{\partial H}{\partial r}\right) \tag{5-8a}$$

and

$$\rho u \frac{\partial C_i}{\partial r} \quad \rho v \frac{\partial C_i}{\partial r} = \frac{1}{r} \frac{\partial}{\partial r} \left(\rho \varepsilon r \frac{\partial C_i}{\partial r}\right) \tag{5-9a}$$

where C_i is the mass fraction of elemental species i. Using C_i, rather than Y_i, eliminates the chemical formation term, $\dot{w}_i$ (Libby, ref. 5-7).

We see that, for the case of constant pressure, equations (5-7), (5-8a) and (5-9a) are identical in form, indicating that the solutions for u, H and C_i are linearly related. In terms of the present nomenclature:

$$\frac{u-u_a}{u_j-u_a} = \frac{H-H_a}{H_j-H_a} = \frac{C_i-C_{ia}}{C_{ij}-C_{ia}} \tag{5-10}$$

The solution of the original set of equations is now reduced to solving global continuity and momentum equations, assuming that the state of the mixing zone chemistry is specified as either frozen or equilibrium. Conceptually, the solution could be obtained if the eddy viscosity were known in terms of the other variables.

Models for the eddy viscosity - For constant density flow, the eddy viscosity or turbulent shear stress models of

Prandtl or Taylor yield results which are satisfactory when compared to experiment. These shear stress models are, of course, semi-empirical and contain one experimental constant. The most widely used expression is the Prandtl eddy viscosity model:

$$\varepsilon = kb(u_j - u_a) \qquad (5\text{-}11)$$

where k is an empirical constant and b is the width of the mixing zone.

Many models have been proposed for mixing with large density gradients, none of which appears to be valid over a significant range of parameters. The only practical procedure at this time is to choose a particular eddy viscosity model, then adjust the empirical constants to give correlation of the theory with experimental results in the range of parameters where the theory is to be applied. The resulting "theory" is not applicable to mixing problems in general, but allows limited extrapolation of experimental data, and also leads to insight into the way the variables interact.

To date, solution of the mixing equations has been accomplished by one of three methods: (1) numerical solution of the boundary layer equations using an assumed model for the turbulent transport (see Vasiliu, ref. 5-8, for example), (2) compressibility transformation technique, and (3) integral method. Most of the work related to the air augmented rocket and to the supersonic combustion ramjet has been achieved with one of the last two methods.

Compressibility transformation technique - Mager (ref. 5-9) proposed a compressibility transformation of the boundary layer equations which is the turbulent counterpart of the Howarth transformation for laminar flow. Ting and Libby (ref. 5-10) used Mager's transformation to derive an eddy viscosity expression for variable density free mixing.

In two dimensional flow

$$\rho^2 \varepsilon = \rho_r^2 \bar{\varepsilon} \tag{5-12}$$

where $\bar{\varepsilon}$ is the constant density eddy viscosity and ρ_r is an unspecified reference density. In axisymmetric flow, eq.(5-12) becomes

$$\rho^2 r^2 \varepsilon = \bar{\varepsilon} \rho_r^2 \int_o^r 2\left(\frac{\rho}{\rho_r}\right) r\,dr \tag{5-12a}$$

Libby (ref. 5-7) analyzed constant pressure axisymmetric two stream mixing with the compressibility transformation technique. Basically, Libby's solution consists of introducing the stream function, ψ, into eq. (5-7). A new axial coordinate is then introduced:

$$\xi = \int_o^x \left(\frac{\rho_r}{\rho \varepsilon}\right) \frac{\bar{\varepsilon}}{u_a \psi_j}\,dx \tag{5-13}$$

$$\text{where} \quad \psi_j = r_{j1}\left[\frac{\rho_j u_j}{\rho_a u_a}\right]^{\frac{1}{2}} \tag{5-14}$$

A linearized solution of the momentum equation was obtained in (ψ, ξ) coordinates, i.e. $\dfrac{u-u_a}{u_j-u_a} = f(\psi, \xi)$.

To obtain the solution in the physical plane, two inverse transformations are required. The first, given by eq. (5-13) requires specification of $\bar{\varepsilon}$, for which Libby used Prandtl's eddy viscosity model (eq. 5-11). Libby also specified that the reference density, ρ_r, is the jet density, ρ_j, in the near field, or the centerline density, ρ_c, far downstream.

The second inverse transformation is required to transform the solution from the ψ coordinates to the radial coordinate:

$$r = \left[\int_0^{\psi} 2\left(\frac{\rho_e u_e}{\rho u}\right) \psi \, d\psi \right]^{\frac{1}{2}} \qquad (5\text{-}15)$$

Other investigators have used essentially the same transformation technique, with changes in the method of linearization of the basic transformed equation, or with different assumptions for the reference density, ρ_r.

For application to the ducted mixing of the air augmented rocket, the compressibility transformation solution is used to solve the indirect problem, i.e. the initial conditions and the assumption of constant pressure define the flow field. The duct contour is then determined by using a mass integral to locate the streamline which corresponds to the wall. The method is not suitable for solution of the direct problem where an arbitrary duct contour is specified and the flow field must be determined. One of the major problems in the evaluation of the air augmented rocket is to determine the performance of a fixed duct geometry for a range of initial

conditions, therefore the compressibility transformation technique has limited usefulness for this application.

Integral methods - The integral method, in which the basic equations are satisfied on the average across the mixing zone, is useful for the analysis of the flow in the air augmented rocket. The greatest advantage of the integral method is that the overall results, such as wall pressure distribution, are relatively insensitive to the choice for the shape of the mixing zone profiles.

Peters, et al (ref. 5-11), made an experimental and theoretical investigation of ducted two stream mixing. Experimental data were obtained for conditions approximating those of the air augmented rocket. An integral mixing theory was developed with the objective of predicting the wall pressure distribution when the initial stream conditions and wall geometry are specified. The following assumptions were used:

1. The inviscid streams are one dimensional and isentropic.
2. The static pressure is constant across any duct section.
3. Viscous effects at the duct wall are neglected.
4. Equation (5-10), relating u, H and C_i may be applied to mixing with axial pressure gradients.
5. The mixing zone chemistry is either frozen or in equilibrium.

The following integral equations were used:

Axial momentum:

$$\frac{d}{dx}\int_0^{r_w} \rho u^2 r dr = -\frac{dp}{dx}\int_0^{r_w} r dr \qquad (5\text{-}16)$$

Continuity

$$\frac{d}{dx}\int_{o}^{r_w} \rho u r dr = 0 \qquad (5\text{-}17)$$

These equations may be expanded as follows (see sketch on page 158 for nomenclature):

$$\frac{d}{dx}\left\{ \rho_j u_j^2 \frac{r_i^2}{2} + \rho_a u_a^2 \left[\frac{r_w^2-(r_i+b)^2}{2}\right] + \int_{r_i}^{r_i+b} \rho u^2 r dr \right\}$$

$$= - \frac{dp}{dx} \frac{r_w^2}{2} \qquad (5\text{-}16a)$$

and

$$\frac{d}{dx}\left\{ \rho_j u_j \frac{r_i^2}{2} + \rho_a u_a \left[\frac{r_w^2-(r_i+b)^2}{2}\right] + \int_{r_i}^{r_i+b} \rho u \, r dr \right\} = 0 \qquad (5\text{-}17a)$$

The mixing zone velocity profile was assumed to exhibit shape similarity and to be represented by a cosine function:

$$\frac{u-u_a}{u_j-u_a} = \tfrac{1}{2}\left[1+\cos\pi\left(\frac{r-r_i}{b}\right)\right] \qquad (5\text{-}18)$$

One additional equation for the rate of growth of the mixing layer is required. The empirical expression proposed by Abramovich (ref. 5-12) for mixing with large density gradients was used:

$$\frac{db}{dx} = \frac{k}{2} \frac{(\rho_j u_j^2 - \rho_a u_a^2) \int \rho d\left(\frac{r-r_i}{b}\right)}{\left[\int_0^1 \rho u d\left(\frac{r-r_1}{b}\right)\right]^2} \qquad (5\text{-}19)$$

Using eqs. (5-18) and (5-19), equations (5-16a) and (5-17a) were solved numerically for the unknowns $p(x)$ and $r_i(x)$.

The theory is compared to an experimental wall pressure distribution in fig. 5-5. Also shown in fig. 5-5 are the parameters for the experimental apparatus. The assumption of a one dimensional rocket stream is badly violated for these experimental conditions. As the rocket plume expands from the nozzle, it causes the air stream to choke at a station downstream from the inlet. This effect was treated in an approximate way by calculating the rocket plume shape with the method of characteristics up to the outer stream choke point. The mixing theory was then initiated at this section, with the assumption of equilibrium mixing zone chemistry.

Radial distributions of pitot pressure and gas composition were obtained at the duct exit plane. The experimental and theoretical distributions are compared in fig. 5-6. Considering the extreme difficulty of making reliable measurements in the high temperature environment, the agreement between theory and experiment is reasonably satisfactory.

The rather crude analytical model seems to provide a satisfactory representation of the mixing zone profiles, but

two faults are evident in the overall analysis. First, the assumption of a one dimensional rocket stream is not justified for many practical configurations. Second, strong axial pressure gradients may have an appreciable effect on the rate of growth of the mixing layer. The Abramovich equation for the growth rate was deduced from constant pressure experimental results, and cannot predict the effect of axial pressure gradients.

Analysis of Chow and Addy - Chow and Addy (ref. 5-13) have analyzed the case of a short ejector configuration in which the primary jet is underexpanded.

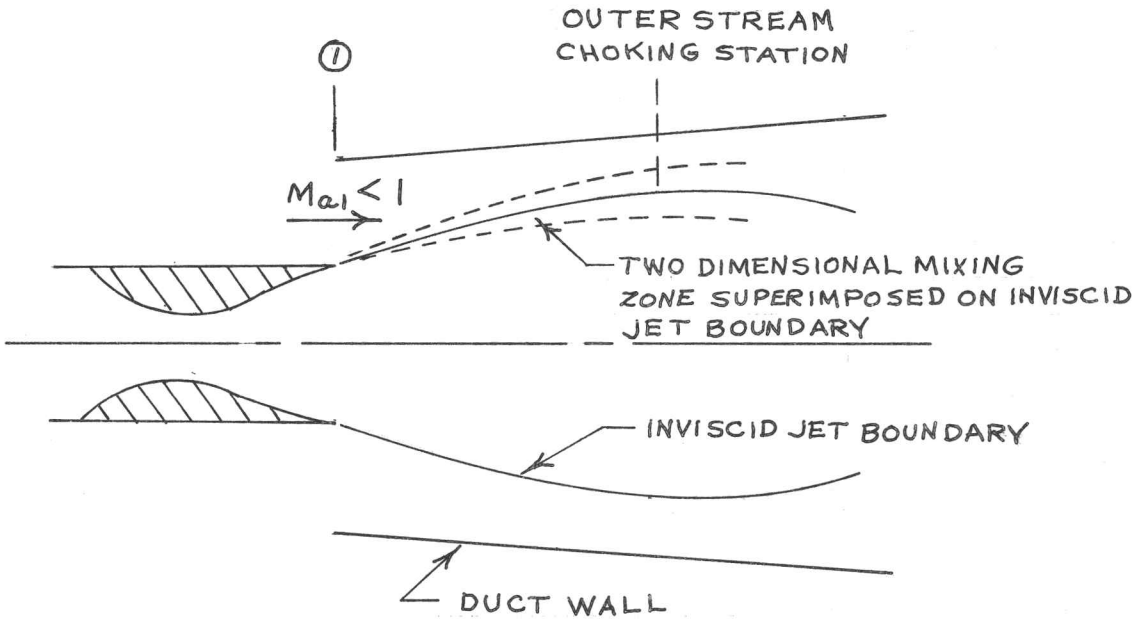

The inviscid flow field is first calculated, using the method of characteristics for the central stream and the assumption of one dimensional flow for the outer stream. The outer stream choking station is established by a trial and error procedure. After the inviscid flow field is established, including the wall pressure distribution, the effect of mixing is calculated

by superimposing a two dimensional mixing zone on the inviscid jet boundary. The change in outer stream mass flow caused by the mixing is calculated by using the concept of a displacement thickness at the choking section. Chow and Addy stated that the accuracy of prediction of the outer stream mass flow and the wall pressure distribution can be improved by an iteration procedure. The theory was found to predict quite accurately the experimental secondary mass flow and wall pressure distribution for the case where both streams are cold air.

The analysis is useful for short ejector or thrust augmentation configurations where the effect of mixing is only a small perturbation on the inviscid flow field. Chemical reactions have not been included in the mixing analysis, nor is the analysis useful for long duct configurations where the mixing effects predominate. It is, however, the only available analysis which considers the non-uniform nature of the central jet.

Other experimental studies - Because of the complex nature of the mixing duct flow, detailed and reliable experimental results are essential for the development of a satisfactory mixing theory. Unfortunately, such data are almost nonexistent for the flow regime of the air augmented rocket.

Several experimental studies have been reported on the problem of thrust augmentation for zero or very low flight velocities, where the air stream total pressure is equal to the ambient pressure, p_∞.

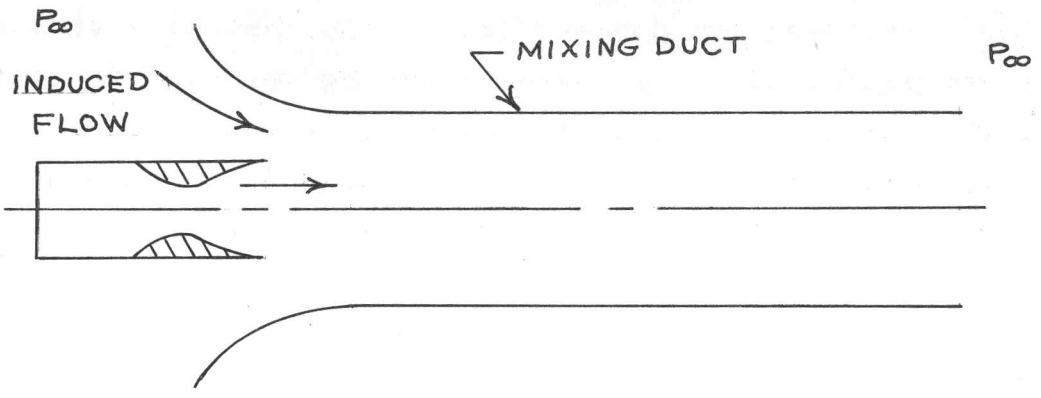

In this type of thrust augmentatinn, the increase in thrust is caused entirely by the decreased pressures on the front surface of the inlet. The main difference between the flow in this type of configuration and the air augmented rocket configuration of fig. 4-3b is that the rocket is normally overexpanded. The mixing process is accompanied by a strong shock system, which hugely complicates the analysis of the flow.

Pool and Charyk (ref. 5-14) made experiments on a static thrust augmentation device consisting of a small oxygen-gasoline rocket engine and a divergent mixing duct. Duct static pressure distributions were measured, but no measurements were made on the flow within the duct.

Scott (ref. 5-15) has recently reported results from another of the early Project Squid investigations. In this

experiment the mixing duct was cylindrical and the central stream was the exhaust from an ethylene oxide monopropellant rocket. Only duct static pressures were measured.

Simonson and Schmeer (ref. 5-16) have investigated static thrust augmentation devices having cylindrical mixing ducts. The central jet came from a hydrogen peroxide decomposition chamber. Measurements were presented on duct thrust, and on radial distributions of temperature and pitot pressure at the duct exit plane.

REFERENCES

5-1 ARMOUR, et al.: A review of nozzle concepts for future solid propellant rocket motors.
Philco Research Lab., RPL-TDR-64-8, March 1964. (AD 436 296)

5-2 SUTTON, et al.: Advanced cooling techniques for rocket engines.
Astronautics and Aeronautics, vol. 4, no 1, January 1966, pp. 60-71.

5-3 GOETHERT: Base flow characteristics of missiles with cluster-rocket exhausts.
Aerospace Eng. vol. 20, no 5, March 1961, pp 108-117.

5-4 MULREADY, et al.: Engine installations for advanced vehicles.
Pratt & Whitney Aircraft, PWA FR 643, (AD 402 761), March 1963.

5-5 GLASSMAN & CHARYK: The ramrocket, in
Jet Propulsion Engines, vol. XII, High Speed Aerodynamics and Jet Propulsion, Princeton University Press, Princeton, N.J., 1959.

5-6 PERINI, et al.: Preliminary study of air augmentation of rocket thrust.
Johns Hopkins University, Applied Physics Lab., TG 545, January 1964.

5-7 LIBBY: A theoretical analysis of the turbulent mixing of reactive gases with application to the supersonic combustion of hydrogen.
ARS Jnl, vol. 32, no 3, March 1962, pp. 388-396.
(also General Applied Science Lab, TR 242, June 1961).

5-8 VASILIU: Determination of temperature, velocity and concentration profiles in the mixing layer between a rocket exhaust jet and the surrounding supersonic air stream.
Convair-Astronautics Report ERR-AN-005, March 1960.

5-9 MAGER: Transformation of the compressible turbulent boundary layer.
Jnl Aero. Sci., voL 25, n° 5, May 1958, pp 305-311.

5-10 TING & LIBBY: Remarks on the eddy viscosity in compressible mixing flows.
Jnl Aero. Sci., vol. 27, n° 10, October 1960, pp 797-798.

5-11 PETERS, et al.: Mixing and burning of bounded coaxial streams.
Arnold Engineering Development Center, AEDC TR 65-4 (AD 458 348), March 1965.

5-12 ABRAMOVICH: Mixing turbulent jets of different density.
Izvestiya Akademii Nauk SSSR, OTN, Mekhanika i Mashinostroyeniye, n° 1, 1962, pp 66-72
(English translation FTD TT-62-1571).

5-13 CHOW & ADDY: Interaction between primary and secondary streams of supersonic ejector systems and their performance characteristics.
AIAA Jnl, vol. 2, n° 4, April 1964, p. 686.

5-14 POOL & CHARYK: Theoretical and experimental investigations of the mixing of a supersonic stream with an induced secondary stream as applied to ducted propulsive devices.
Project Squid Technical Report n° 25, Princeton University, September 1950.

5-15 SCOTT: Mixing and combustion of a supersonic fuel jet and a subsonic coaxial gas stream.
Project Squid, Technical Report UVA-7-P, University of Virginia, August 1965. (AD 469 052).

5-16 SIMONSON & SCHMEER: Static thrust augmentation of a rocket ejector system with a heated supersonic primary jet.
NASA TN D 1261, May 1962.

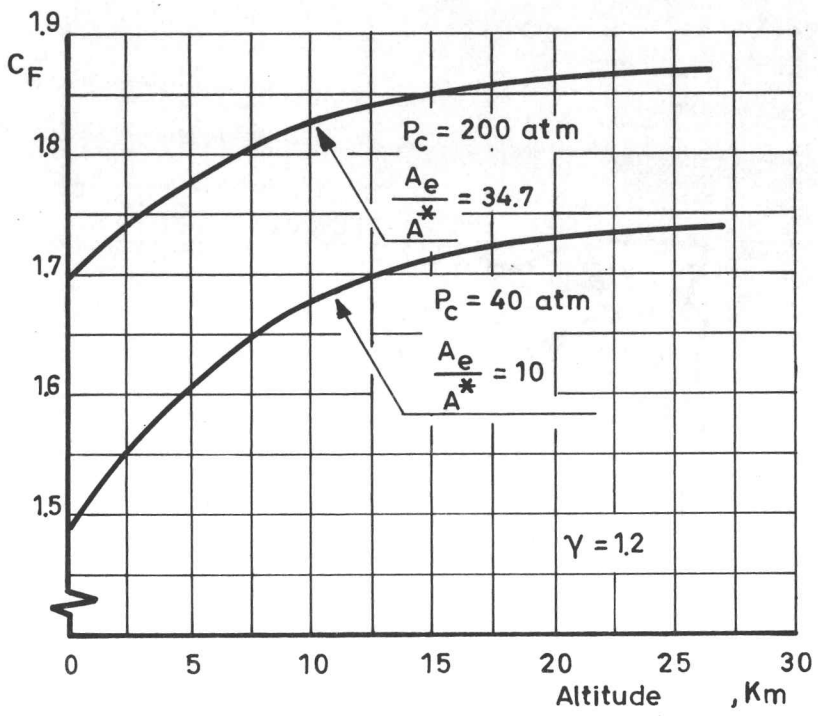

a. Thrust coefficient

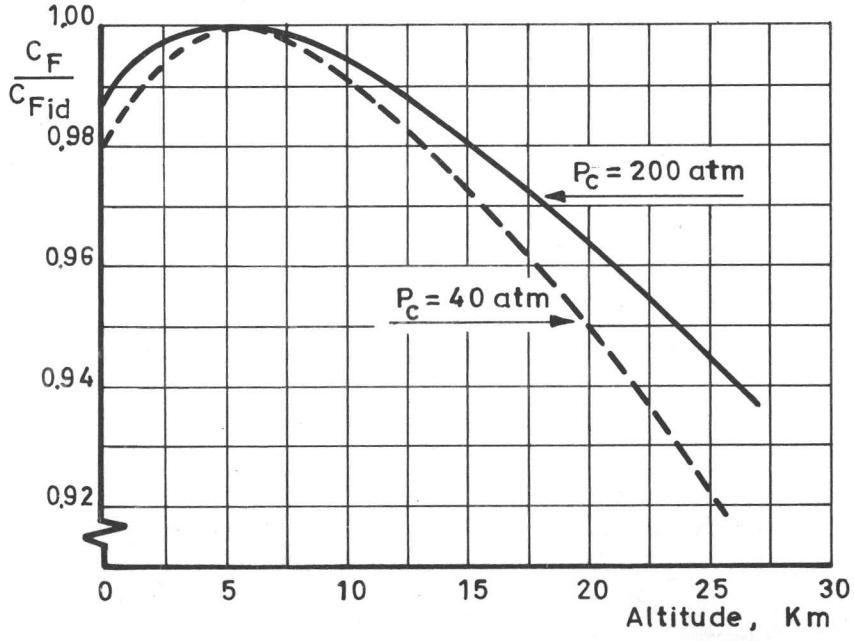

b. Thrust coefficient compared to ideal

Fig. 5-1 EFFECT OF CHAMBER PRESSURE ON IDEALIZED NOZZLE PERFORMANCE

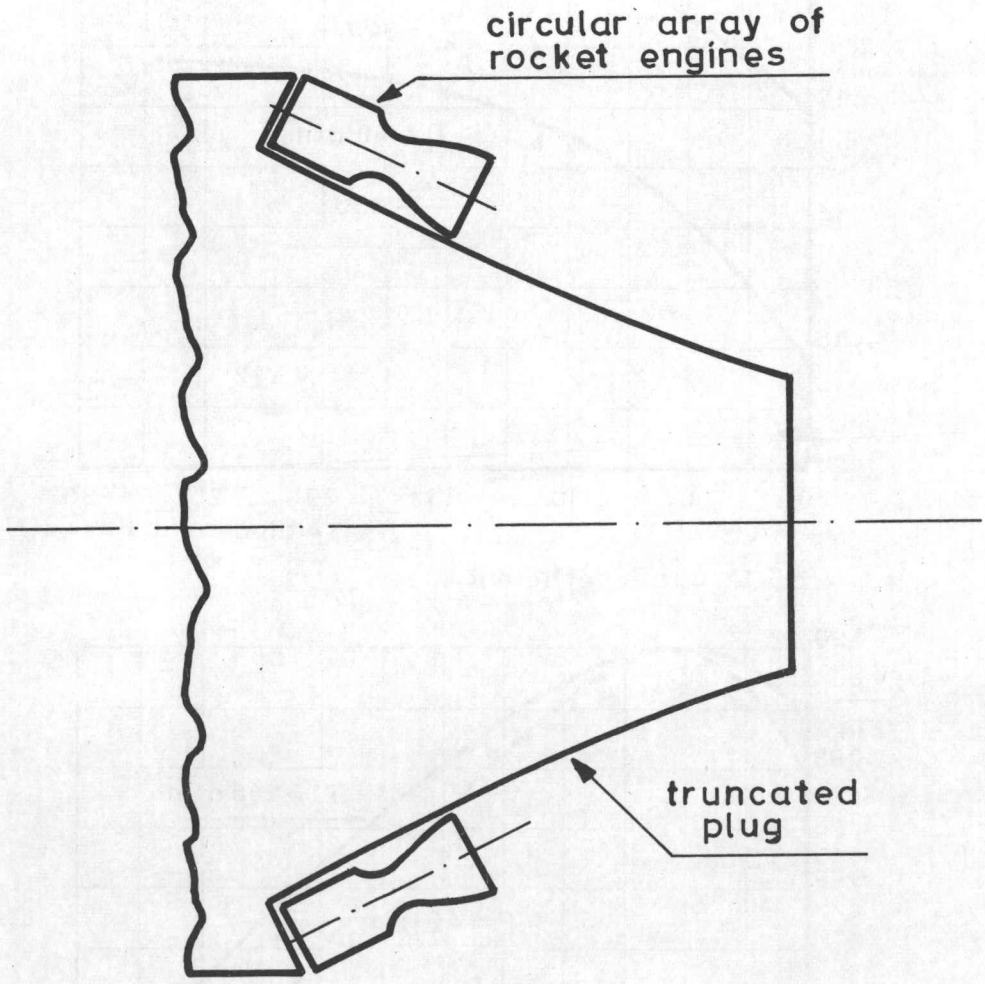

Fig. 5-2 PLUG-CLUSTER EXHAUST NOZZLE (ref. 5-4)

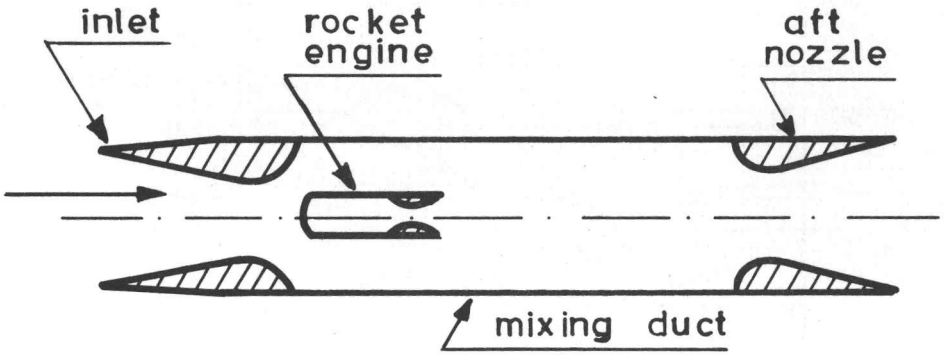

a. Ramrocket

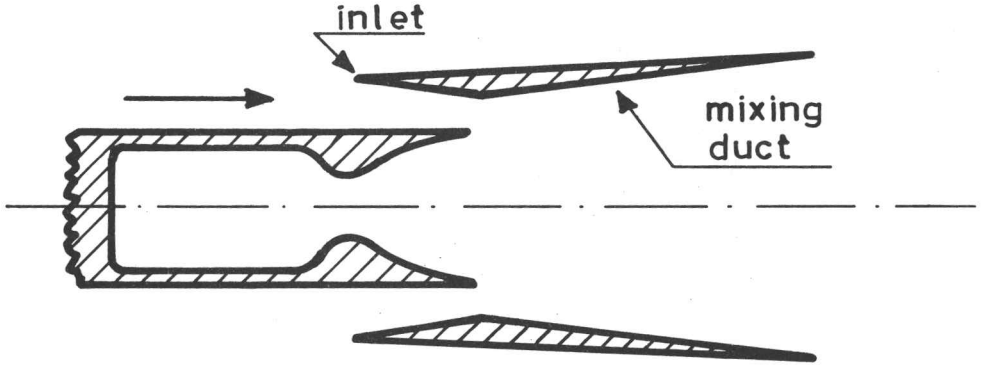

b. Air augmented rocket

Fig. 5-3 COMBINATION ROCKET-AIR BREATHING PROPULSION SYSTEMS

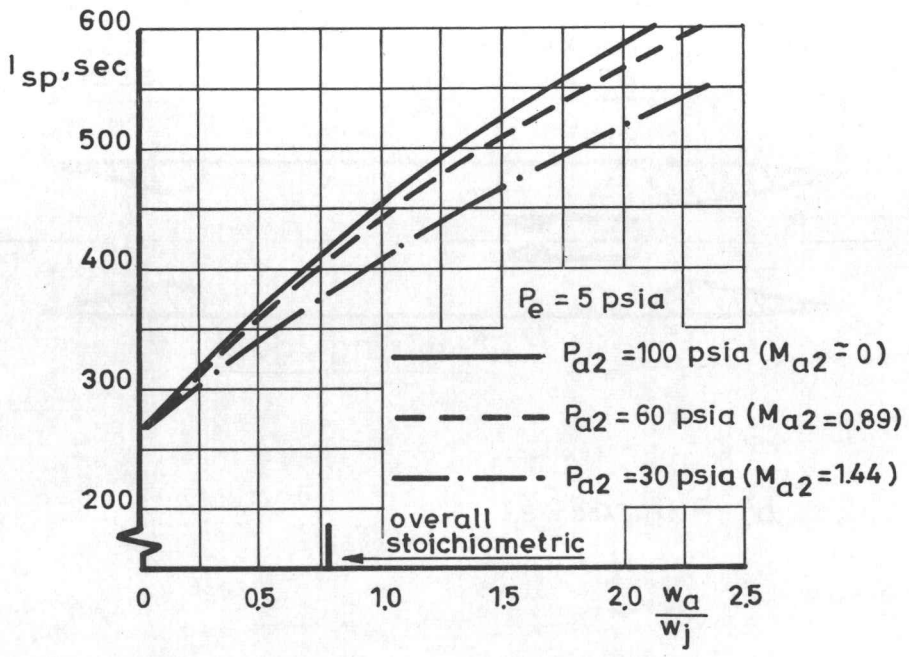

a. Effect of injection pressure , P_{a2}

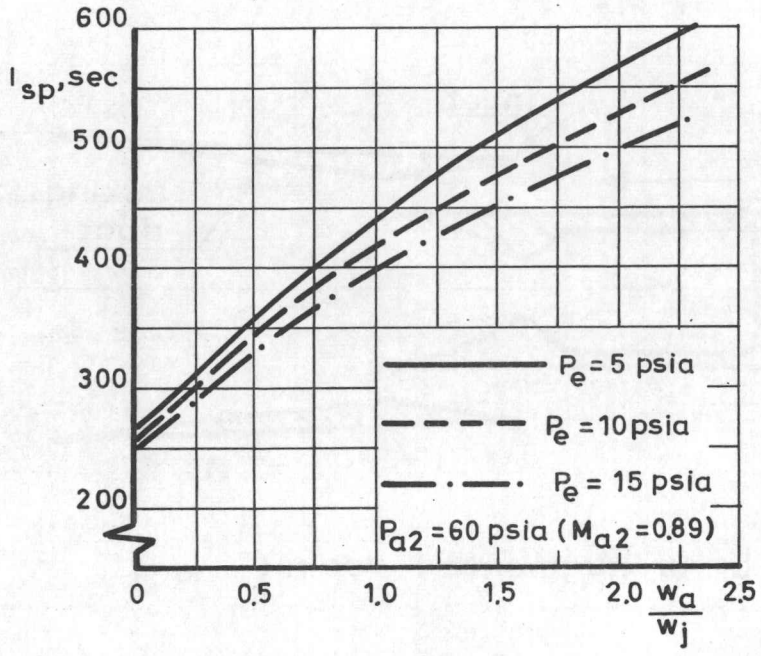

b. Effect of exit pressure , P_e

Fig. 5-4 OVERALL ANALYSIS OF THE AIR AUGMENTED ROCKET (ref. 5-6)

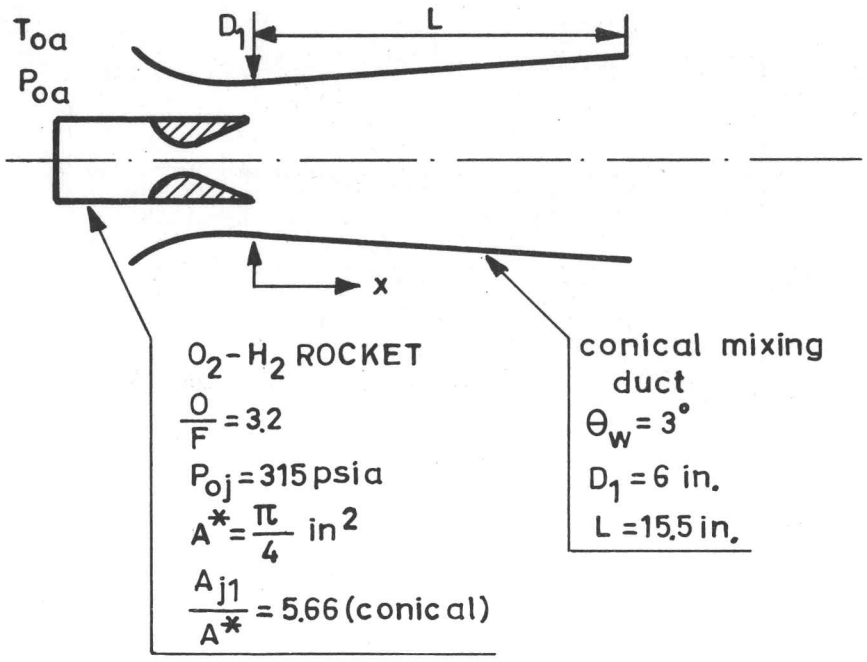

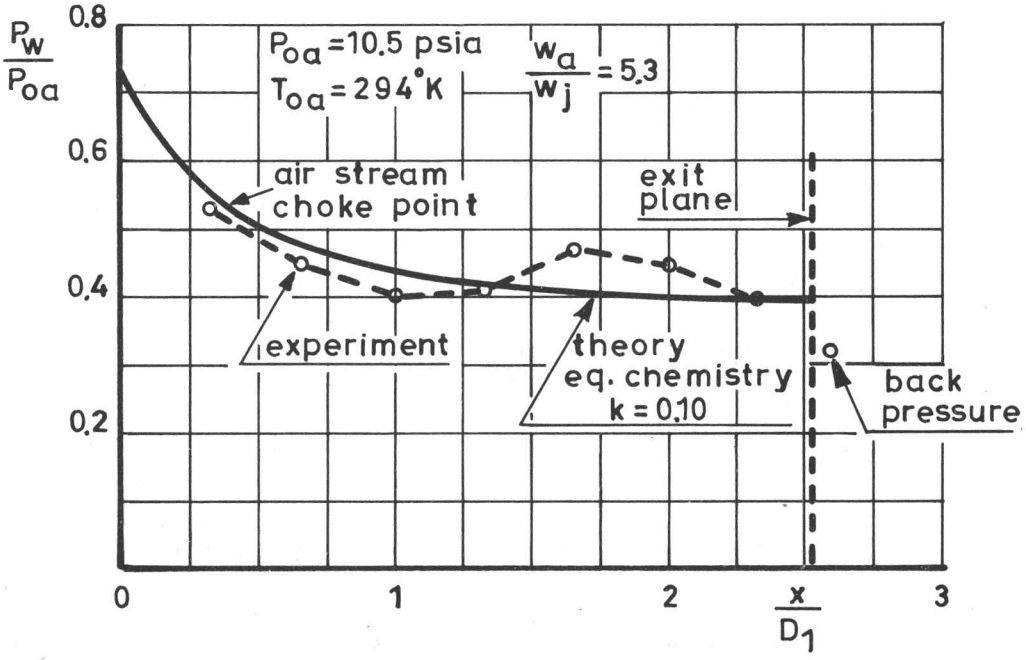

Fig. 5-5 PRESSURE DISTRIBUTION IN MIXING DUCT (ref. 5-11)

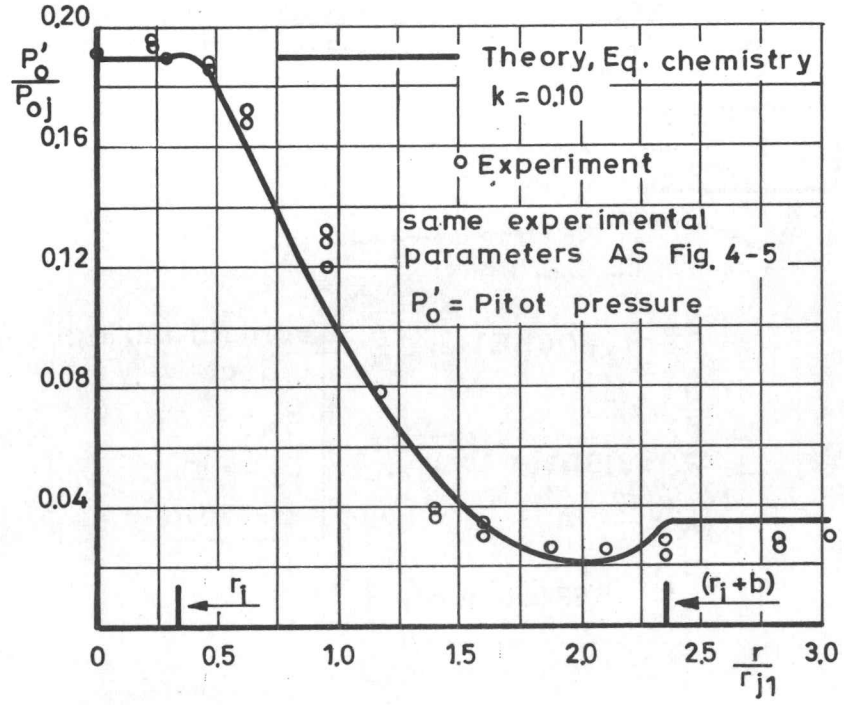

a. Pitot pressure distribution

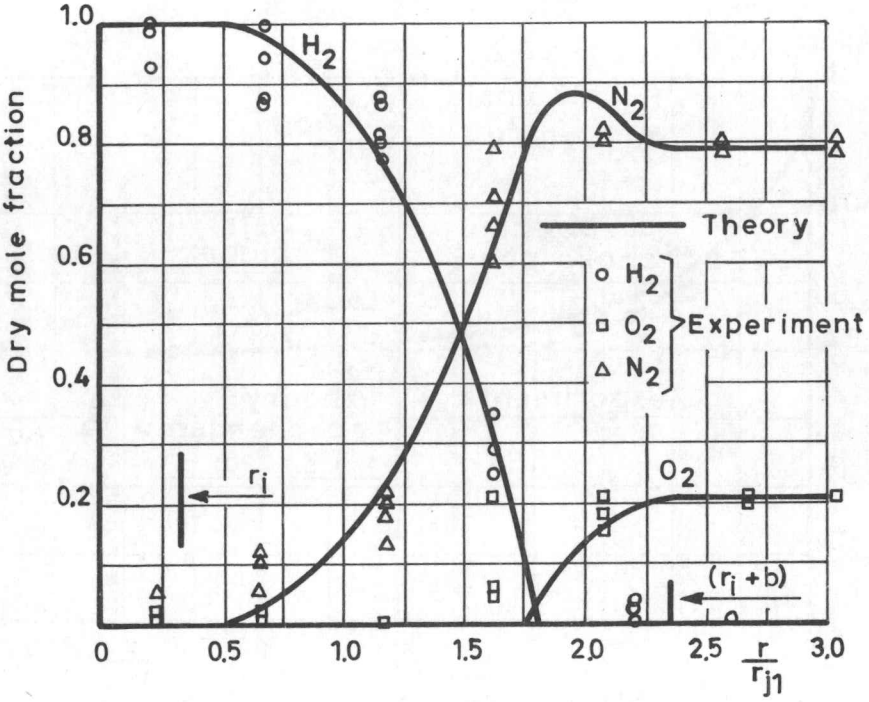

b. Gas composition distribution

Fig. 5-6 RADIAL DISTRIBUTION OF FLOW PROPERTIES AT MIXING DUCT EXIT (ref. 5-11)